UNIVERSITÀ DEGLI STUDI DI MESSINA

PHD IN "PHYSICS"
XXXVI CYCLE

Study of clustering states in neutron-rich nuclei with FARCOS detector

---

SSD FIS/04

Author:
Fabio RISITANO

Tutor:
Prof. Marina TRIMARCHI

Co-Tutor:
Dr. Brunilde GNOFFO

Ph.D Coordinator:
Prof. Vincenza CRUPI

DIPARTIMENTO DI SCIENZE MATEMATICHE E INFORMATICHE,
SCIENZE FISICHE E SCIENZE DELLA TERRA (MIFT)

A.A. 2022–2023

Contents

List of Figures

List of Abbreviations

INFN	**I**stituto **N**azionale di **F**isica **N**ucleare
LNS	**L**aboratori **N**azionali del **S**ud
CLIR	**C**lusters in **L**ight **I**on **R**eactions
CHIMERA	**C**harged **H**eavy-**I**on **M**ass and **E**nergy **R**esolving **A**rray
FARCOS	**F**emtoscope **AR**ray for **CO**rrelations and **S**pectroscopy
FRIBs@LNS	In-**F**light **R**adioactive **I**on **B**eams **at LNS**
DSSSD	**D**ouble **S**ided **S**ilicon **S**trip **D**etector
MCP	**M**icro **C**hannel **P**late
AMD	**A**ntisymmetrized **M**olecular **D**ynamics
FRAISE	**FRA**gment **I**n-flight **SE**parator
RIB	**R**adioactive **I**on **B**eam
QDC	**Charge**-to-**D**igital **C**onverter
TDC	**T**ime-to-**D**igital **C**onverter
PSD	**P**ulse **S**hape **D**iscrimination
ToF	**T**ime-**o**f-**F**light
CFD	**C**onstant **F**raction **D**iscriminator
CS	**S**uperconducting **C**yclotron
GET	**G**eneric **E**lectronic for **TPCs**
TPC	**T**ime **P**rojection **C**hamber
ASIC	**A**pplication **S**pecific **I**ntegrated **C**ircuit
ASAD	**AS**IC plus **AD**C
ADC	**A**nalog-to-**D**igital **C**onverter
μTCA	**Micro T**elecom **C**omputing **A**rchitecture
CoBo	**Co**oncentration **Bo**ard
FPN	**F**ixed-**P**attern **N**oise
MuTanT	**Mu**ltiplicity **T**rigger **an**d **T**ime
RNQM	**R**ecombination and **N**uclear **Q**uenching **M**odel

Introduction

In nature, there are many phenomena in which it seems that independent objects can naturally aggregate into more complex structures, giving rise to a collection of smaller sub-units. This phenomenon is generally referred to as *clustering*, and, although this concept will be explored, in the context of this work, only in Physics, similar effects also exist in biological, social, human and animal contexts. Its attraction in the eyes of the research scholar lies especially in the fact that phenomena of this type occur at all physical scales, from the microscopic to the macroscopic, from nuclear scales and sub-nuclear particles to planetary, stellar and galactic structures. The dynamical evolution of such many-body systems arises mainly from the attempt to obtain a higher internal stability, gained from the reduction of the potential energy of the system. In astrophysics for example, from *galaxy filaments* to *galaxy superclusters*, these structures arise from the natural aggregation of galaxies subjected to the gravitational field. Even the formation of stellar systems like our own or planets within them are further immediate proofs of these phenomena. On a microscopic scale, even the cells of the human body, i.e. eukaryotic cells, may have formed at the eve of life by *endosymbiosis*, a type of evolution in which prokaryotic cells incorporated other cells creating substructures, and established reciprocal cooperative relationships. In this way each cell can be seen as an ensemble of many sub-structures, each of which covers a very specific task. Finally to molecular to subatomic scales, atoms form molecules, both in liquid and gas phase, while they form crystals in the solid state with well-established internal symmetries, some even of extreme complexity. Although some present structures with extreme complexity, their formation is regulated by the same principles and laws, aggregating into structures regulated by the reduction of a chemical potential. On subatomic scales, quarks are confined, since the early stages of life of the universe, to form hadrons, like mesons or baryons, made of 2-3 constituents.
Furthermore, in the case of atomic nuclei there are characteristics common to

this phenomenon. Unlike the early *liquid drop* model, in which protons and neutrons were considered to be in a spherical symmetry inside the nucleus, behaving like molecules in a drop of liquid, we now know that the nucleus is a dynamic agglomeration of its constituents governed by quantum effects, which exert fields around them from which correlation forces arise. Unlike bosons, fermions are subjected to the Pauli Exclusion Principle, for which orbitals can be occupied at most by a pair of the same nucleon, with opposite spins. In this context, the nucleus of ^{4}He, or α particle, being formed by a pair of neutrons and one of protons, is an important nucleus with a very high binding energy per nucleon among the light nuclei, of about 7 MeV/A. Its great internal stability, in conjunction with the initial studies of the α decay, led to think that this structure could coexist relatively unperturbed within the nucleus for a significant amount of time. As in the cases of clustering mentioned above, it was supposed that the nucleus could therefore be constituted, under certain conditions, by such α sub-units, free to form inside the nucleus, offering a greater advantage in terms of binding energy of the system. This clustering phenomenon of α-particles is nowadays one of the most advanced research topics of modern heavy ion nuclear physics. Many lines of research around the world aim to investigate this phenomenon both from a theoretical stand, through the study of models to characterize the nucleus and predict its energy levels of cluster states, and from the experimental point of view, with the use of detectors and of increasingly advancing techniques for the characterization of reactions of interest. Moreover, the topic of α-clustering has also remarkable involvements in several other fields, such as in astrophysics, where this model can be used to explain phenomena concerning the nucleosynthesis of heavier elements. This is the case of the famous Hoyle state of ^{12}C, which clarified the process of carbon formation in stars.

In this thesis, the topic of clustering will be addressed in particular in the context of the research carried out at the Laboratori Nazionali del Sud (LNS) of the Italian Instituto Nazionale di Fisica Nucleare (INFN), and in particular inside the scientific program of the CHIRONE group. Numerous results on cluster physics of international relevance have been obtained here, over the last 20 years. Furthermore, the primary object of the thesis will also regard the discussion of the results obtained from the data analysis of the CLIR (Clustering in Light ion Reactions) experiment, conducted at the LNS with the CHIMERA and FARCOS detectors. In particular, in Chapter 1 the

phenomenon of clustering in light ions will be explored, from the dawn of this line of studies to the most recent results, giving a general vision of the phenomenon and the importance of its study. Furthermore, the main purpose of the CLIR experiment will be detailed more carefully, starting from some promising results obtained during previous works, which constituted the main motivation for the experiment. This in particular concerned the study of such cluster states in neutron-rich radioactive nuclei. In fact, it has already been known for some time in the literature that such nuclei can exhibit exotic configurations in which the substructures of α particles are bound together by so-called *valence neutrons*, much like chemical molecular bonds, so that they are defined as *molecular states*.
Subsequently, in Chapter 2, the experimental apparatus employed will be discussed, in particular starting from the FRIBs facility used to produce a radioactive beam containing various isotopes of interest. After explaining the production method of the cocktail beam used, the tagging system used in the identification of the ions in the beam will be explored in greater detail. Then, the experimental apparatus used to study projectile break-up reactions will be described, namely the 4π CHIMERA multidetector and the FARCOS array, detailing their main identification techniques and features.
Finally, in Chapter 3 the results obtained for the analysis carried out will be discussed, starting from the calibration method used depending on the detector, and the results obtained for the study of the ^{10}Be cluster break-up for the $^{4}\mathrm{He} + {}^{6}\mathrm{He}$ decay channel. In particular, the analysis carried out on FARCOS was of fundamental importance in this case. FARCOS is a detector consisting of 3 different stages, two Double Sided Silicon Strip Detectors (DSSSD) followed by four CsI(Tl) scintillators, providing great angular and energetic resolution. After having calibrated the 3 stages of FARCOS and identified the fragments of the various reactions through the ΔE-E method, the ^{10}Be excitation spectrum of the $^{4}\mathrm{He} + {}^{6}\mathrm{He}$ decay channel was reconstructed, showing the presence of different peaks of interest, associated with cluster states and molecular configurations. Finally, the conclusions will be shown, in particular indicating the future prospects of the CLIR experiment, the analysis of which will continue by increasing the statistics, refining the resolution of the experimental data, and evaluating the background.

Chapter 1

Cluster in light nuclei

1.1 Nuclear clustering in $N = Z$ conjugated nuclei

The study of clustering phenomena in nuclei is one of the most fascinating research topics in modern nuclear physics, since it connects properties of the nuclear force with the structure of light nuclei, allowing to congregate in internal sub-structures. This study has its roots back to the beginning of the last century, even prior to the discovery of the neutron. Since the discovery of the proton, of the α decay and of the nucleus, various models were created to characterize the atomic nucleus and its properties. One of the most traditional models that describes the nucleus and its components is the *liquid drop model*. This essentially describes the atomic nucleus as a drop of liquid, in which protons and neutrons behave like molecules, treating the whole structure as an incompressible fluid of high density. Therefore, according to this model the nucleus is held together by the strong nuclear force, conceivable as a volumetric force, mediated by various other contributions such as the Coulomb repulsive force of the protons, the surface tension of the "drop of liquid", the fermionic behavior of the nucleons and spin coupling. This model is able to predict the atomic mass and binding energy of nuclei, as well as to explain radioactivity phenomena and nuclear fission. However, the model fails to explain the structure of light ions, where *clustering* effects can occur.

Although the concept of clustering in nuclear physics is relatively modern, the first idea of a similar phenomenon dates back much further than one might actually think. In fact, although the concept of clustering has been explored just recently in the nuclear field in the last 50 years, a model based on α particles was already hypothesized since the 1920s, with the study of α

decay. In fact, it was thanks to Bethe and Becher that a nuclear model with α particles began to be concretely hypothesized. This was mainly due to some major premises, first of all the high binding energy per nucleon of ^{4}He (about 7 MeV) and the presence of a first excited state at about 20.21 MeV. Moreover, it was also thought that α particles could coexist within the nucleus itself for a fairly long time. This was mainly thanks to Gamow and his pioneering work in 1928, which, applying the quantum theory for the first time to nuclei, demonstrated the emission of the α particle by the tunneling effect. Finally it was seen how some light nuclei, such as ^{8}Be, ^{12}C and ^{16}O had energies of bonding much higher than neighboring nuclei, and that such species could be imagined as an agglomeration of multiple α sub-structure, bonded together. It was this initial work that led Hafstad and Teller to develop a description of such nuclei with $A = 4n$ with $n = 2, 3, 4, \ldots$ and equal number of protons and neutron, which binding energy can be described as a function of the number of possible $\alpha - \alpha$ bonds within the nucleus. They therefore developed a "van der Waals" potential between two α particles, according to the previous work of Bethe and Becher, i.e. repulsive at short and long distances but attractive at medium distances. In this way they found that these α particles inside the nucleus could arrange themselves into ordered, symmetrical and almost "crystalline" structures, depending on the number of possible bonds, minimizing the configuration space between the α particles. Furthermore, they observed that the binding energy of such light self-conjugated ions showed a linear trend with the number of possible $\alpha - \alpha$ bonds within the nucleus (Fig. 1.1). As a direct consequence, it was possible to obtain ordered and symmetric structures made up of α particles, for example triangular geometries for ^{12}C and tetragonal for ^{16}O.

This model however fails to distinguish clustering phenomena at ground or excited states, underlining that α-clustering was therefore possible even at the ground state. However, as it was later discovered, such α cluster states can generally be found only when the ground state is very close to the cluster decay threshold (or Q-value), which is generally much higher than the ground state. Moreover, this model was in complete contrast with the liquid-drop model, which does not contemplate the existence of possible agglomerates of nuclides inside the nuclear structure. A big step forward occurred in the 1950s, following the study of the existence of possible other cluster states. One of these, for example, was the possible 3α state of ^{12}C, hypothesized by

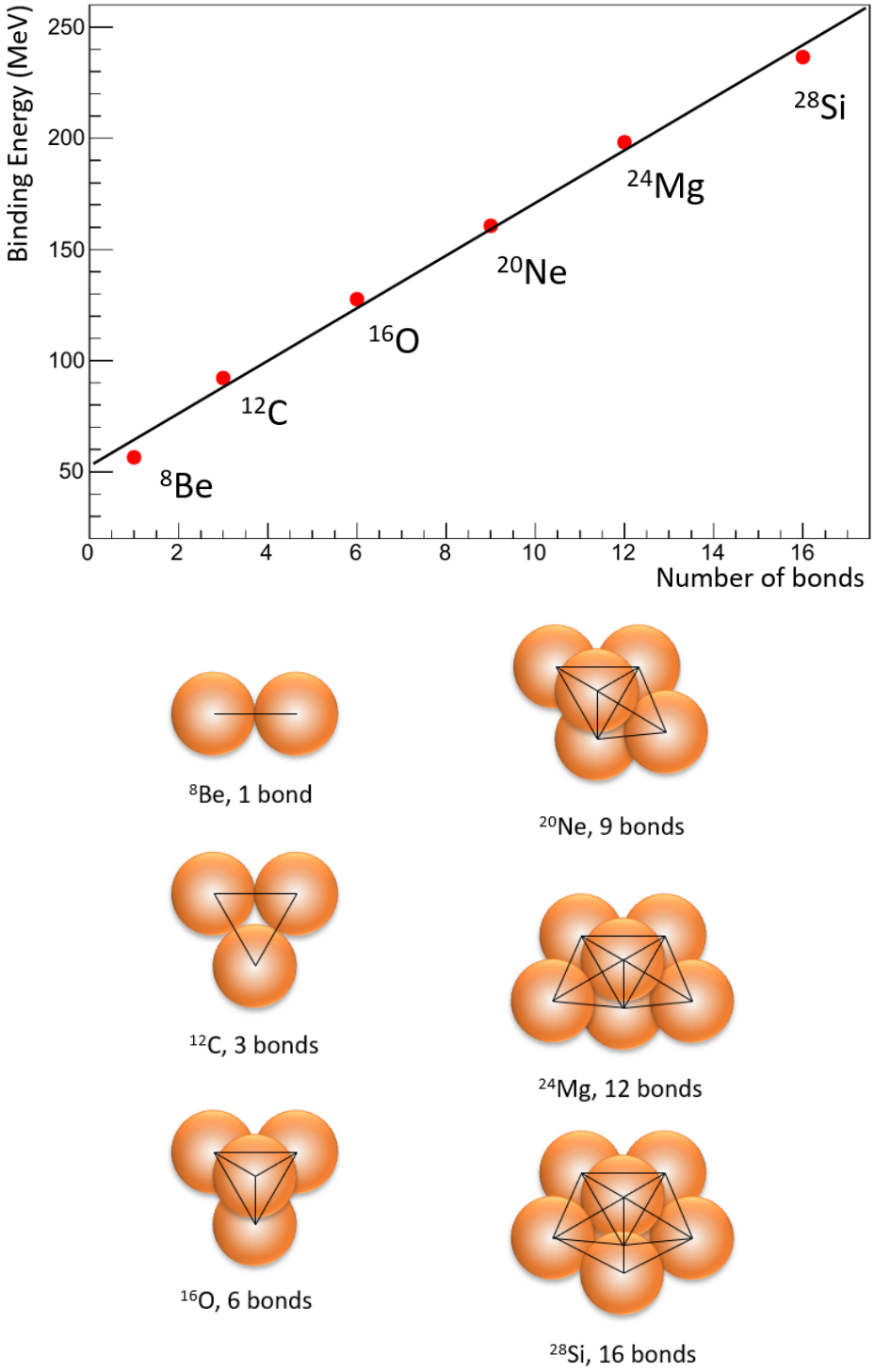

FIGURE 1.1: Binding energy for $A = 4n$ with $n = 2, 3, 4, \ldots$ versus the number of possible $\alpha - \alpha$ bonds. A clear law of proportionality can be observed, as studied by Hafstad and Teller. Figure adapted from [1, 2].

Hoyle in 1954 [3]. The Hoyle state was initially hypothesized for astrophysical reasons related the nucleosynthesis of carbon in stars, but it was found that this state can exhibit features consistent with a cluster state of three α particles. In particular, this state will be discussed in more detail in Sect. 1.3. Furthermore, in 1956 Morinaga suggested the possible presence of exotic spatial configurations for such cluster states, with previously discussed nuclei that could assume *linear chain* configurations. This interpretation, which would give rise to structures with angular momentum values very different from the ground state configurations, will in fact be fundamental. Although such linear structures logically should seem energetically disfavored, Morinaga hypothesized that, with the right excitation energy, such configurations would be possible. Finally, the idea that these α particle cluster states could not appear at the ground state was consolidated: a cluster state could then manifest only at certain precise energy levels, such that the interaction between nucleons and nuclear potential energy can allow the rearrangement of the nucleons. Thanks therefore to the research by Ikeda et al. [4], who transferred this concept into a diagram shown in Fig. 1.2, the formation of various other structures was also predicted for a large variety of light ions. For each structure the energy required to liberate the cluster constituents was also calculated, emphasizing its connection with the excitation energy of the system. Many of these predictions have also been confirmed experimentally, whereby cluster states have been found with energy levels close to the cluster decay thresholds.

1.2 Cluster states in neutron-rich nuclei

Subsequent to their work on light self-conjugated nuclei, Hafstad and Teller continued to apply the method they developed also on other nuclei, in particular such that $A = 4n + 1$, in a similar way to what was previously explained, by studying neutron-rich isotopes of beryllium, carbon, oxygen,.... They discovered that the binding energy of such systems did not depend only on $\alpha - \alpha$ interactions, but also on the presence of the added neutron. In this way, $\alpha + n$ bonds could then be established, showing the presence of clustering effects. Over the years, this discovery proved to be decisive as the interest of the international community began to shift also to neutron-rich

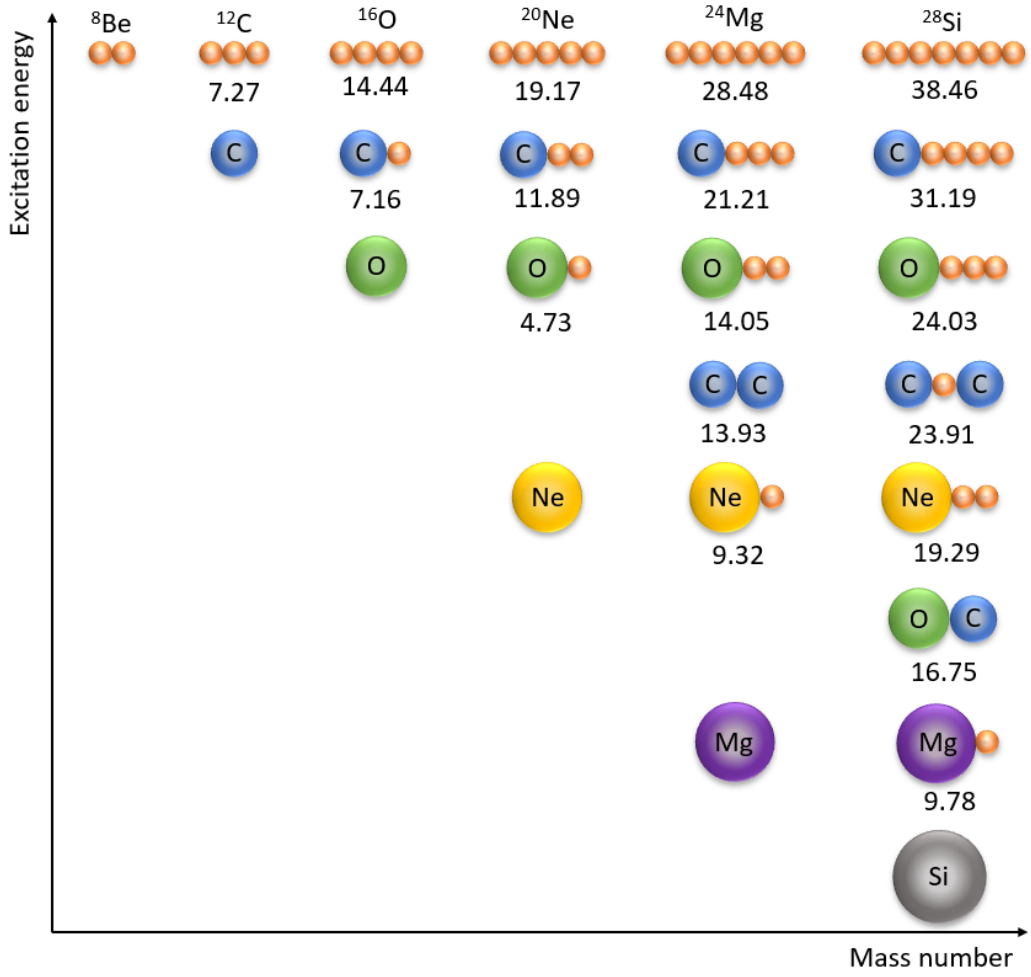

FIGURE 1.2: Ikeda diagram showing threshold energies predicted for cluster decay in MeV. The identified cluster structures can undergo cluster decay at energy levels close to the derived energies. Figures adapted from [5].

and exotic weakly-bounded nuclei, which could exhibit clustering phenomena enhanced by the presence of extra neutrons. The main concept behind these clustering effects is that the added neutron(s) is exchanged between the α cores, increasing the stability of the cluster structure. This phenomenon was therefore described in analogy to the basic concepts of molecular bonds in chemistry between atoms and molecules, in which electrons are covalently exchanged between the molecule ions. In this case the neutrons, also called *valence neutrons*, exchanged between the cluster particles, allow covalent bonds in order to stabilize these unstable multi-cluster states.

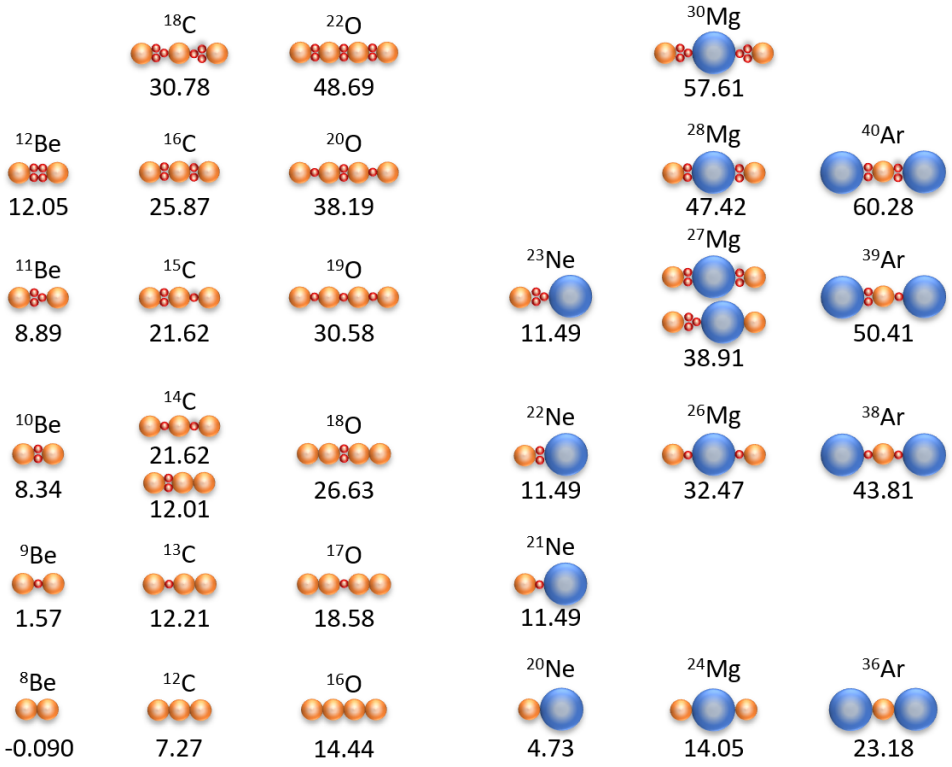

FIGURE 1.3: Ikeda diagram extended for neutron-rich isotopes. Molecular structures are shown, including the energy contribution (in MeV) considering also the additional valence neutrons. Figure adapted from [5].

The addition to clustering effects of the contribution of neutrons allows to obtain a multitude of interesting case studies. Some of these can be observed, in a similar fashion to what was previously shown, from the modified Ikeda diagram represented in Fig. 1.3. Similar to the original Ikeda diagram in Fig. 1.2, this one shows the possible cluster structures for a series of neutron-rich nuclei, reporting the cluster decay threshold considering the neutron contribution. In particular, some remarkable examples concern those obtainable from beryllium and carbon isotopes. In fact, these, being made up of two or three α particles plus valence neutrons, can exhibit exotic configurations, with high angular momentum. Moreover, the presence of multiple neutrons allows also configurations in which the valence neutrons can couple and increase the complexity of the excitation energy levels of the states.
A key example in this context is the case of ^{9}Be which, unlike ^{8}Be, is stable at

the ground state, thanks to the presence of an additional neutron. Its structure can therefore be thought of as a nuclear dimer of α particles, which can reach even very high degrees of deformation, depending on the excitation energy of the system. A very similar situation also occurs for the case of ^{10}Be structure, which instead can be represented as a dimer held together by a pair of valence neutrons. It is in fact the presence of this valence neutron couple that makes this a very interesting nucleus, with a great variety of molecular states of interest. The ^{10}Be case will be addressed in more detail in Sect. 1.5.1. Valence neutrons, in a coherently similar way to the case of molecular bonds, in the nuclear case can produce different molecular orbitals depending on the separation plane between the two bonded α particles: in the case of beryllium isotopes for example, but also in that of carbon and oxygen, covalent bonds can be arranged in different orientations depending on the excitation energy of the cluster state, for example perpendicularly, forming π-type orbitals, and in parallel (σ-type orbitals), to the separation axis. In the case of ^{9}Be, a π bond was predicted for the ground state, typical of a more compact dumbbell-like structure, while also a σ-type orbital configuration is possible for higher energies, leading to a greater spatial separation between the two cores [6, 1]. Moreover, as one can see from the extended Ikeda diagram, cluster states can even be formed by asymmetric cores, leading to the formation of more complicated structures for which further studies are currently necessary. More example cases are that of neon, magnesium and argon isotopes, which can present dimer cluster structures formed by α cores and a ^{16}O core, held together by possible valence neutrons depending on the atomic number, generally enabled by the stability of the ^{16}O nucleus. Another interesting possibility in this case is the asymmetric cluster structure of ^{13}B, theorized to present a $^{9}\mathrm{Li} + \alpha$ exotic cluster state. More details about this specific case will be addressed in Sect. 1.6.2.

Generally, this type of cluster structure can be studied through different theoretical approaches, which can possibly predict, to a degree, both the cluster structure and the excitation energy necessary for its formation. One of the models that has allowed to produce a multitude of successful results is the Antisymmetrized Molecular Dynamics (AMD) model [7, 1]. The AMD approach, by simply constructing the wave function of the system, including all the different degrees of freedom of the nucleons, is able to prove the presence of core clusters without imposing them in the calculation. This method

is therefore able to give a description of the cluster structure of a system, simply making it emerge naturally from the nucleon-nucleon interaction, obviously accounting also for the Pauli exclusion principle. The AMD approach has been applied on many case studies, including in particular those of the lithium, beryllium, boron and carbon isotopes, allowing to reproduce the bond energies, transition rates, radii and momenta in accordance to a certain degree with those obtainable experimentally.

1.3 Importance of clustering phenomena in astrophysics

The cluster structure of light nuclei can also have important implications in the field of nuclear astrophysics. An important factor that can influence the nucleosynthesis of elements in stars is in fact the nuclear structure, which, depending on the ion, can be decisive. The main aspect that influences these nucleosynthesis processes is the great stability of ^{4}He, which, thanks to its ≈ 7 MeV/u binding energy, is also stable enough to form, through fusion, heavier elements, such as ^{6,7}Li, through the channels $^4\mathrm{He} + d$ or $^4\mathrm{He} + t$.
Another key example in this context is the aforementioned Hoyle state for ^{12}C, hypothesized by the British physicist in 1954 [3], linked to the carbon formation in stars. The abundance of carbon within stellar processes is important and non-trivial, due to a series of factors, from the nucleosynthesis of heavier elements in Red Supergiant stars, to the abundance of carbon in star systems, and therefore looking at our star, also for life on earth. At the time, the main reaction mechanism that was known to allow the production of carbon was when a star, in the final phase of its life, started to burn helium, producing heavier elements. Normally the carbon production process occurs in two different steps, i.e. the aggregation of two α particles in ^{8}Be, with the subsequent integration of a third α nucleus. However, one of the most striking questions related to this process was about the subsequent abundance of carbon, which cannot be explained simply by this process. The ^{8}Be nucleus in fact possesses, as can be seen from the Ikeda diagram reported previously in Fig. 1.2, a cluster state exactly at the ground state: the two ^{4}He particles remain technically unbound at the ground state and the ^{8}Be nucleus

subsequently decays after very short times of the order of 10^{-16} s into its constituents. This can be seen also by a calculation of the structure of the ions, revealing at the ground state a classic dumbbell-like shape of two α particles having a rotational band consistent with a 2:1 symmetric deformation. Hoyle realized that this process alone could not have accounted for the whole abundance of carbon and heavier elements in stars: the ^{8}Be production represents a sort of *bottleneck* for the production of ^{12}C, which, according to calculations, allowed reaction rates approximately 8 orders of magnitude smaller if the whole process undergoes only through direct capture.
For this reason, Hoyle hypothesized a different process of formation of ^{12}C, in which he proposed the capture of the third α particle through an s-wave ($l = 0$) resonance. This state would have a momentum $J^\pi = 0^+$, in order to favor the formation of carbon as a cluster state, presenting a structure of 3 resonant α nuclei, or equivalently a $^8\text{Be} + \alpha$ system. The excited state also required an energy higher than the cluster decay threshold at 7.27 MeV (from Ikeda diagram), later found at 7.65 MeV. The ^{12}C ions thus produced in this state have a large probability, about 99.96% of decaying back to the $^8\text{Be} + \alpha$ system, allowing to reach a sort of equilibrium between formation of ^{12}C and the decay into three α particles. However, only for approximately one event over 2500, the ^{12}C produced at the Hoyle state is allowed to decay at the ground state, first by reaching the first excited state at 4.44 (2^+) MeV, emitting a first 3.21 MeV γ ray, and subsequently decaying again at the ground state (with $J^\pi = 0^+$) emitting a second γ ray. In this way, ^{12}C ions, now stable after the emission of two γ rays, are actually produced, which can then be subsequently used for the production of heavier elements. The whole process is also depicted on Fig. 1.4. Other than this double-γ decay channel, since the spin of both Hoyle and g.s. are 0^+, there are two other possible ways for ^{12}C to decay: undergoing $E2$ transition to the 4.44 (2^+) intermediate state, or electric monopole transition $E0$, by emitting a electron-positron pair. This last $E0$ process, important for the complete calculation of the radiative width of the Hoyle state, however has a very low branching ratio of the order of $\approx 6.7 \times 10^{-6}$ [8], therefore very difficult to identify.
In the context of the Hoyle state, given the total reversibility of the ^{12}C production reaction, it is also interesting to study the exact dynamics of ion production, starting from α particles: in fact, recent works have shown how the reaction of three α particles is more commonly a sequential process, therefore forming in two different steps: first the ^{8}Be ion at the ground state, with

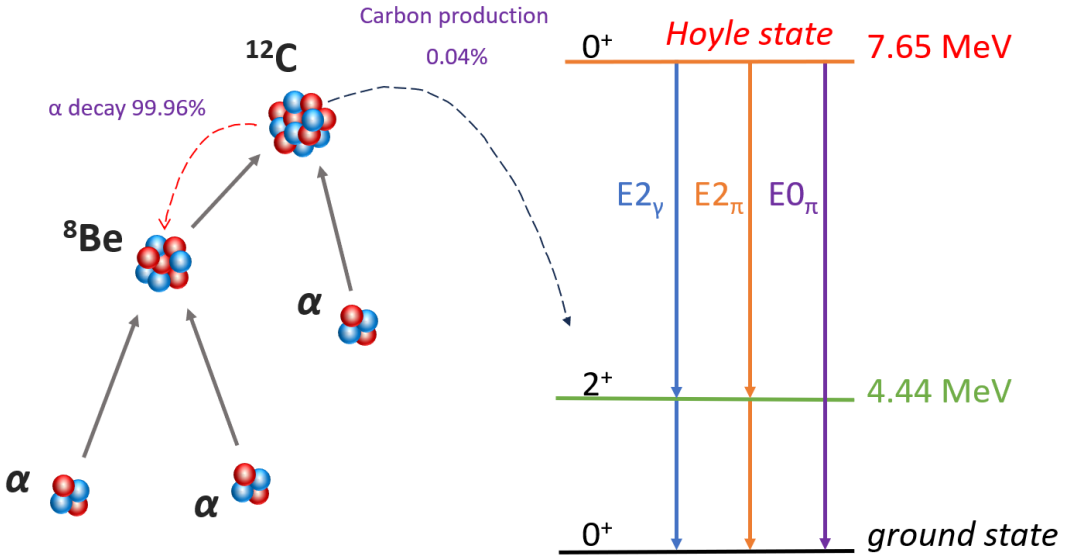

FIGURE 1.4: Schematical graph of the triple α process for the production of ^{12}C. From the plot it is possible to note the various states and processes involved in the de-excitation from the Hoyle state. Figure adapted from [9].

a subsequent interaction of a third ^{4}He particle. This process differs from a much more unlikely direct process, in which three α particles bypass the production of ^{8}Be at the ground state to directly produce ^{12}C.
Some investigations also have been performed on the existence of a possible Efimof-like state for ^{12}C [10, 11, 12]. An Efimov state is a bound state born from quantum mechanical effects of three identical bosons when the attraction of the two particles however is too weak to allow two bosons to pair. In this case, all the 3 couples of α particles have the same center of mass energy of the ^{8}Be ground state, thus allowing to predict it at an excitation energy for ^{12}C of 7.458 MeV, slightly different from the energy of the Hoyle state and from its behaviour.
Another important case, relevant for astrophysics, is the formation of ^{16}O involved in the burning phase of helium of Red Giant stars, from the $^{12}\mathrm{C} + \alpha$ reaction channel. The abundance of ^{16}O is crucial especially for the determination of the final stages of the life of a star, as the relative ratio between the quantities of carbon and oxygen determine, as well as the time scale of the last phase of the star, the chemical composition of the material emitted by type Ia Supernovae [13].

1.4 CLIR: Clusters in Light Ion Reactions

A long experimental campaign has been carried out over the last 20 years at the Laboratori Nazionali del Sud (LNS) of the Istituto Nazionale di Fisica Nucleare (INFN), aimed to study the physics behind the phenomena of clusters in light ions. Thanks to the availability of beams and energies at LNS, since the early 2000s, it was possible to carry out studies in the context of clustering on both stable and radioactive nuclei, especially aimed to point out the fundamental role played by α-correlations in light nuclei. Special attention has been devoted by the CHIRONE group [14] during the years to the physics of the Hoyle state [12, 15], already discussed before in Sect. 1.3, through reactions $^{4}\mathrm{He} + {}^{12}\mathrm{C}$ (64 MeV) and $p + {}^{12}\mathrm{C}$ (24 MeV), by simultaneously detecting the scattered projectile, carbon target and the two γ rays from the decay of excited carbon ions. Furthermore, some experiments were dedicated to the investigation of clustering in ^{13}B or ^{14}C through the Resonance Elastic Scattering method, showing the presence of some interesting states possibly associated with exotic clusters [16]. Moreover, thanks to the FRIBs@LNS (In-Flight Radioactive Ion Beams at LNS) facility, which will be discussed in Chapter 2, the opportunity of studying such phenomena even expanded to non-conjugated and radioactive nuclei.
In this context, the CLIR (Clustering in Light Ion Reactions) campaign was started in 2015, with experimental and theoretical investigations conducted with the aim of studying clustering and molecular states in light radioactive ions. The experiment was primarily intended to study the decay channels associated to cluster decomposition break-up channels of radioactive isotopes of beryllium, boron and carbon, through the FARCOS hodoscope, which was used for the first time, and with the aid of the CHIMERA 4π multidetector. More details about the features of the detectors employed and on the facility FRIBs will be later given in Chapter 3.
As discussed previously in Chapter 1, neutron-rich light isotopes can present clustering effects leading to the formation of "molecular" structures inside the nucleus, due to the rearranging of nucleons into clusters of α particles, held together by so called "valence" neutrons. Moreover, for a given element, as the number of neutron number increases, approaching the neutron drip-line, other exotic clustering effects start to appear, leading to the formation of pair effects in valence neutrons, in which the nuclear molecule is held together by "covalent" bonds. One typical example is the discussed configuration

α-2n-α-2n-α of ^{16}C, theorized by von Oertzen [17, 18], which can assume different shapes, such as the extremely deformed linear chain with a 3:1 configuration.
A relatively simple way to investigate clustering effects in light ions concerns the study of ejectiles compatible with cluster decomposition in break-up decay channels in reactions at intermediate energy on light targets. In fact, by detecting the reaction products, one could calculate the excitation energy E^* of the incident nucleus from the relative energy of the reaction products E_{rel} and Q-value or threshold of the selected break-up channel Q_{gg} by the formula:

$$E^* = E_{rel} - Q_{gg} \tag{1.1}$$

In the case of a binary emission channel, given m, E, θ and ϕ, indicating respectively the masses, energy and emission angles of the break-up products given with respect to the vertical plane and the beam axis, one can calculate:

$$q_1 = (p_{1x}, p_{1y}, p_{1z}, E_1 + m_1); \tag{1.2}$$

$$q_2 = (p_{2x}, p_{2y}, p_{2z}, E_2 + m_2); \tag{1.3}$$

the four-momenta of the two break-up products. Then, the relative energy E_{rel}, can be calculated from the formula:

$$\begin{aligned} E_{rel} &= m_{12} - m_1 - m_2; \\ &= \sqrt{(q_1 + q_2)^2} - m_1 - m_2; \end{aligned} \tag{1.4}$$

where m_{12} is the invariant mass of the two break-up products. Therefore, through a statistical evaluation of the excitation energy E^*, obtainable through the Q-value of the break-up reaction, it is possible to obtain an energy spectrum from which to obtain energies and energy levels for the chosen reaction channel. Moreover, if the state is characterized by a deformed shape, as in the case of linear, chain-like molecules, predicted for some state of ^{10}Be or ^{16}C, rotational bands with large moment of inertia can be observed.
The CLIR experiment was then proposed to study the break-up decay channels of neutron-rich isotopes of beryllium, boron and carbon, thanks to the availability of the FRIBs facility, which could have been obtained only by a single primary beam fragmentation. This had the great advantage of producing a variety of RIBs at the same time, by fragmenting a primary beam

of $^{18}O^{7+}$ on a ^{9}Be target. For this purpose, the identification of the isotopes arriving in the experimental hall was also crucial, both online and off-line, to better discriminate the reaction product for the correct decay channel, so a *tagging* system was needed, coupled with the experimental hall acquisition. Details about the FRIBs facility and the production and tagging of the cocktail beam will be given in Chapter 2. To trigger break-up fragmentation of the projectiles and excite levels associated to cluster states, a light reaction target is required. In this case the main plan was to use two thin targets, of CH_2 and ^{12}C. The analysis mainly involves the study of the reactions of interest on the polyethylene target, and in particular on the hydrogen ions, as will be subsequently described in Chapter 3.
Moreover, the experiment was also used to prove the capabilities of the FARCOS detector, which was used in this kind of experiment with heavy ions for the first time. In this experiment, the FARCOS array aims to further improve the angular resolution of the data gathered in the forward part and reconstruct the emission angles θ and ϕ with a better resolution than the one achievable with the CHIMERA 4π multidetector. Correlations between emission angles in fact show periodic structures that, if interpreted by using Legendre polynomials, can give insight to the angular momentum of the excited level, allowing to extract the moment of inertia of deformed clustering structures. Moreover, the use of the 4π CHIMERA array could be used to refine the data, not achievable with the only FARCOS telescopes. This can be done for example by gathering the recoil target nucleus, which is usually excited by the collision with the projectile, or its de-excitation products in the case of ^{12}C targets. The last ones in particular can be usually recognized by analyzing their parallel velocity, not compatible with the projectile decay. This technique generally allows to select with a good accuracy the true break-up decay channels from a spurious background, including compound-nucleus formation or quasi-elastic transfer phenomena.

1.5 Previous cluster investigations at LNS: the UNSTABLE experiment

As already indicated in Sect. 1.4, cluster physics has been studied at Laboratori Nazionali del Sud for a long time: many experiments and theoretical investigations have been conducted on the study of clusters, both in stable

nuclei, such as ^{12}C [[12, 15, 19, 20] and ref. therein], and in neutron-rich isotopes, with the study of molecular cluster structures [[16, 21, 22] and ref. therein]. The LNS are an ideal place for the study of such phenomena, thanks to the presence of various experimental apparatus, such as the already mentioned CHIMERA 4π multidetector and FARCOS array, and to the possibility to produce radioactive beams at the Fermi energies (10 MeV/u $\leq E/A \leq$ 100 MeV/u). Furthermore, thanks to the the new FRAISE facility, currently under construction (App. A), it will be possible to further expand the variety of available beams, and also to push towards the production of isotopes next to the *neutron drip-line*.

One of the most promising results was obtained by the UNSTABLE experiment, carried out by the EXOCHIM group with the CHIMERA 4π multidetector. In fact, results obtained on the spectroscopy of ^{10}Be and ^{16}C above the clustering emission threshold, allowed to set the basis for the planning of the CLIR experiment, here discussed, and aimed to further improve the quality of the gathered data, by increasing the resolution and to expand the analysis even to other nuclei. In this case, the CHIMERA multidetector was used to gather data, while break-up reactions were induced by both a polyethylene CH^2 (50 μm) and deuterated polyethylene CD^2 (28 μm) targets. More details about the CHIMERA multidetector will be given in 2.4. The experiment, performed in 2011, used a radioactive ion beam produced by the FRIBs facility, fragmenting a ^{18}O primary beam, accelerated by the CS at 55 MeV/u, on a thin ^{9}Be target, 1.5 mm thick. Fragments were then selected with the In-Flight technique, with a rigidity $B\rho \approx 2.8$ Tm and momentum acceptance $\Delta p/p \approx 0.01$. The cocktail beam produced was then identified in its components by a *tagging* system, made by a Micro-Channel Plate (MCP) and a double-sided Silicon Strip Detector DSSSD (140 μm), ≈ 12.9 m apart, through the ΔE-ToF technique. The state of the cocktail beam was verified and currents calculated, finding a high intensity for ^{16}C at 49.5 MeV/u ($\approx 10^5$ pps), ^{13}B ($\approx 5 \times 10^4$ pps) and ^{10}Be at 56 MeV/u ($\approx 4 \times 10^4$ pps). Since the projectile break-up cross-section is generally forward-focused, a large variety of fragments coming from break-up decay channels was expected in the most forward part, around the beam axis, so particular importance for the analysis was covered by the first three rings of CHIMERA. Fig. 1.5 shows a typical identification plot for the cocktail beam produced, identified through the ΔE-ToF technique, while Fig. 1.6 shows a ΔE-E spectrum obtained for forward telescopes, through which identification in charge and mass was performed.

1.5.1 Study on ^{10}Be clustering: from UNSTABLE to CLIR

The excitation energy of the nuclear states cluster was obtained by analyzing the couple correlations between decay products coming from ^{10}Be. The excitation energy E_x was obtained with the Invariant Mass technique, explained in Sect. 1.4, adding the energy threshold for the ^{4}He + ^{6}He decay channel ($-Q_{gg} = 7.409$ MeV) to the relative energy of the two components. Details on the same technique can be found in Sect. 1.4. Fig. 1.7 shows the spectrum of the reconstructed excitation energy, with vertical arrows indicating the positions of known peaks in literature. Background was estimated through *event-mixing* procedures (green dashed line), showing no substantial shapes or structures. On the other hand, the red and yellow dashed lines correspond to the simulated detection efficiencies, obtained by performing Monte-Carlo simulations for the CHIMERA apparatus, assuming respectively hydrogen or carbon recoil atoms for the CH_2 target. Simulations of the reaction kinematics between ^{10}Be and target nuclei in fact show that in the range of the excitation energy of interest, the limit angle for scattering on hydrogen is about 5.77°, while there is no limit angle for scattering on carbon. In this way, because of the more forward-focused kinematics, by using a polyethylene target, the forward detectors around the beam axis become more important, leading to higher detection efficiency.
Many internal structures can be identified in the excitation energy spectrum,

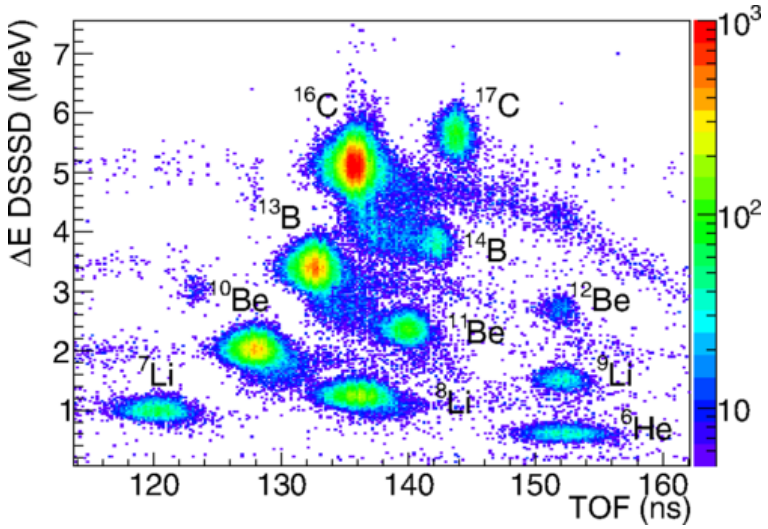

FIGURE 1.5: ΔE-ToF plot obtained for the cocktail beam produced during the UNSTABLE experiment. Several isotopic species can be observed. Figure taken from [21].

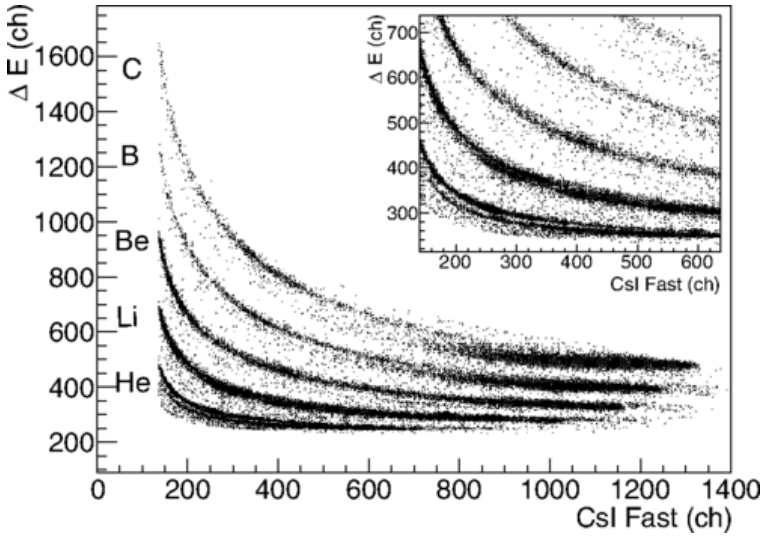

FIGURE 1.6: ΔE-E spectrum obtained for the ring covering $\theta = 3.1^\circ$ for Si-Csi(Tl) telescopes, showing the energy loss on the Si detector (ΔE) and residual energy on the corresponding CsI(Tl). Figure taken from [21].

with at least 4 peaks reported in literature, and still objects of studies. Between these, two peaks stand out for their interest: the 10.2 MeV (2^+) and 13.5 MeV (6^+), belonging to the ^{10}Be molecular rotational band [21, 23]. As reported in [23], the ^{10}Be molecular rotational band is made of a 6.179 MeV (0^+) state, under the threshold emission, and a 7.542 MeV (2^+) state just above it, with a $\approx$ 10.2 MeV state for a possible 4^+ state of the same band. Moreover the 13.5 MeV, particularly interesting because not reported at that time, was identified with reasonable accuracy as also a possible candidate for the missing 6^+ state of the same molecular rotational band. Spin and parity was estimated by angular correlation analysis in terms of Legendre polynomials (Fig. 1.8), for both the 11.8 MeV and 13.5 MeV peaks. For the first one, it was found a value of $J^\pi = 4^+$, in agreement with past works and theoretical calculations, while for the 13.5 MeV peak, several values have been fitted, showing the best match with χ^2 analysis with experimental data for $J^\pi = 6^+$ with reasonably good agreement.

The CLIR experiment starts from this standpoint in order to improve the analysis conducted, not only through a new, more intense radioactive beam, but above all also using the FARCOS array. In fact, one of the main problems detected during the previous experiment was the relatively poor angular resolution, which in turn translated into a not entirely excellent energy

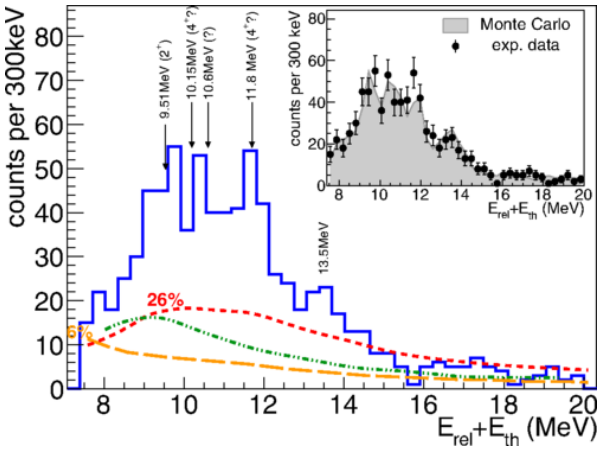

FIGURE 1.7: ^{10}Be excitation spectrum obtained for the ^{4}He + ^{6}He decay channel obtained during the UNSTABLE experiment. The vertical markers indicate the position of known states for the nucleus. The dashed lines represent the detection efficiency obtained assuming hydrogen recoil (red) and carbon recoil (orange). Background obtained through event mixing procedures is shown (green line). Figure taken from [21].

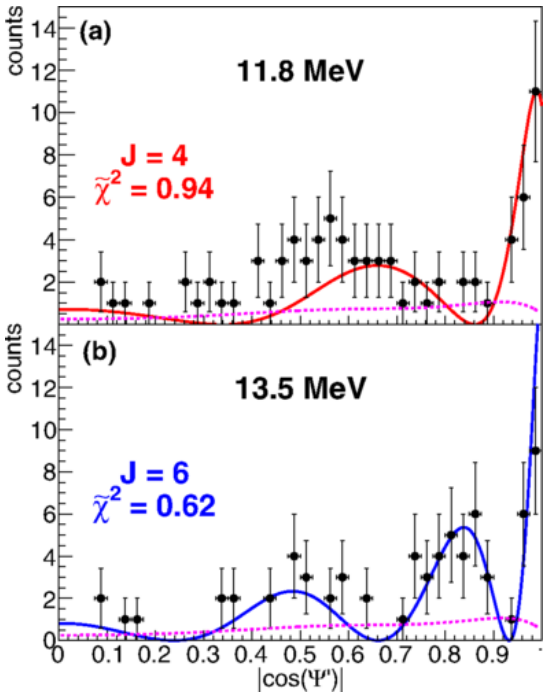

FIGURE 1.8: Angular correlation distribution obtained for ^{10}Be for the ^{4}He + ^{6}He decay channel obtained during the UNSTABLE experiment for the two states at 11.8 MeV and 13.5 MeV excitation energy. Figure taken from [21].

resolution. For this reason CLIR, with the aid of FARCOS telescopes positioned at small angles, where most of the break-up fragments are emitted, with its three different detection stages, promises to be an excellent tool to obtain even better results.

1.6 Case studies on clustering in CLIR

The promising results obtained, especially in the context of the UNSTABLE experiment, led to the proposal of the new CLIR experiment, with the aim of prosecuting the studies still in progress, while addressing the problems encountered in the past. The first among these is the need to improve the statistics, which is possible both through reproducing the experiment and by improving the experimental apparatus. For this purpose, it was therefore decided to use, for the first time in a real experiment, the FARCOS detectors, still under development at the LNS. FARCOS, thanks to its high granularity and energetic resolution, as it will be described in Sect. 2.5, represents a powerful tool for this kind of study. Moreover, given the small spatial aperture of the kinematic emission cone of the break-up fragments, the detectors would allow us to obtain more accurate information on the reaction spectroscopy, while placed at small angles around the beam axis. For this reason, it would also be very powerful even for other case studies, further from the stability valley, and much harder to investigate. Other than the ^{10}Be case described above in Sect. 1.5.1, for which analysis is ongoing and will be presented in Chapter 3, here in this section some interesting case studies will be indicated.

1.6.1 The ^{16}C case

Clustering in carbon isotopes has always been an interesting topic in the context of molecular states, thanks to its nature as a $3-\alpha$ cluster. The Hoyle state for ^{12}C represents perhaps one of the most studied examples, as previously described in Sect. 1.3. As what regards studies about radioactive isotopes of carbon at LNS, such as for the ^{16}C, its cluster states have already been investigated with the UNSTABLE experiment, with results however still preliminary and in need of further experimental confirmation, due to the insufficient statistics.

On the international scene, both theoretical and experimental work has been

carried out on the nature of neutron-rich isotope clustering, as well as research on possible neutron skin effects. For example, recent theoretical calculations show spectroscopic factors and neutron-skin thickness of even-isotopes (^{12,14,16,18}C) [24], while several experiments performed at GSI investigate the matter radii for neutron-rich isotopes, while other pointed out the presence of neutron skin halos for ^{15}C and neutron skins for ^{16,17}C [25, 26].
One of the possible cases to be investigated through the CLIR experiment revolves around the case of ^{16}C, produced together with other species from the same cocktail beam. In this case, many studies have mainly focused on the possible existence of a linear cluster structure of α particles. From a theoretical point of view, AMD calculations [27] show the presence of possible molecular states with high moment of inertia around 16.81 MeV (0^+), with molecular orbitals possibly coherent with the decay channel $^4\text{He} + ^{12}\text{Be}(2^+)$. Moreover, in a subsequent work, the possible presence of a linear chain state with excitation energy at around 30 MeV was investigated, which neutrons could occupy orbitals $(1/2^-_\sigma)^2(1/2^+_\sigma)^2$ with a high moment of inertia. From the experimental point of view, sequential decay of ^{16}C for the ($^4\text{He} + ^{12}\text{Be}$) and ($^6\text{He} + ^{10}\text{Be}$) decay channels was investigated [28, 29], showing the presence of a 16.5 MeV (0^+) state, in agreement with AMD calculations. Moreover, observation of excited states at 27.2 MeV could be in agreement with the AMD calculations stated above, of linear chain with valence neutron occupying the $(1/2^-_\sigma)^2(1/2^+_\sigma)^2$ orbitals.

1.6.2 The ^{13}B case

The case studies of α clusters bound together by valence neutrons, like in isotopes of beryllium or carbon mentioned earlier, are not the only ones possible to be studied in the context of the CLIR experiment. In fact, there are many other exotic cluster states with unstable configurations, theoretically predicted but surely more difficult to produce. This is the case for example of the exotic clusters of the ^{13}B nucleus, which case study is quite peculiar, having a magic number ($N = 8$) of neutrons. While for ^{12}Be, the neighboring nucleus with just one proton of difference to ^{13}B, many clustering states have been predicted, both in ground states and excited states, the situation is not yet well understood with the isotonic counterpart of boron. Unlike other boron isotopes (^{15,17}B), for which cluster states were predicted in the ground

state using AMD models, ^{13}B presents a $3/2^-$ ground state with a closed neutron p-shell configuration, especially due to the magic number of neutrons. On the other side however, AMD calculations made by Kanada-En'yo et al. [30], show largely deformed states with highly excited configurations or cluster states, appearing in energy regions compatible with the normal excited states. Some well-developed exotic cluster structures like $^9\text{Li} + \alpha$ are suggested, for states $J^\pi = 1/2^-$ and $J^\pi = 1/2^+$, with energy threshold emission at about 11 MeV, researchable with ^{13}B radioactive beams. Moreover, cluster states with $^{12}\text{Be} + p$, $^{10}\text{Be} + t$ and $^7\text{Li} + ^6\text{He}$ decay channels have been predicted, but further investigations are needed. Among light nuclei, perhaps the case of clustering structures in boron is possibly the less known one: while some theoretical studies have been produced during the years with different models, mainly AMD, there is still much need for experimental proof to validate models, as the interpretation of their results is still approximate and should be detailed. The presence of ^{13}B in the cocktail beam species for the CLIR experiment could be of considerable importance in the international scenery of cluster physics. Moreover, the new CLUB experiment, specifically dedicated to the investigation of these ^{13}B cluster states has already been approved within the CHIMERA 4π multidetector activity research. The CLUB experiment, postponed in the next years due to the pandemic, will make use the CHIMERA multidetector coupled with the FARCOS array, positioned at small angle, and the new facility of radioactive ion beams FRAISE, currently under construction and discussed in Appendix A.

Chapter 2

Experimental apparatus of the CLIR experiment

In this Chapter, the experimental setup of the CLIR experiment will be described. As already mentioned in Chapter 1, the CLIR experiment was performed at INFN-LNS in Catania in 2015 [31], at the FRIBs@LNS (in-**F**light **R**adioactive **I**on **B**eam**s at LNS**) facility. In this chapter details on the experimental setup of the fragment separator will be given, explaining the method of production of RIBs, employing the In-Flight technique. Moreover, the tagging system employed for the identification of the radioactive isotopes produced will be described, while also explaining the technique used for the selection of the beams. Finally, the detectors employed for the study, the CHIMERA 4π multidetector and the FARCOS arrays, will be described, explaining their detection features and techniques of identification, as well as the electronics.

2.1 General setup of the experiment

A Radioactive Ion Beam (RIB) was produced by the FRIBs@LNS (in-**F**light **R**adioactive **I**on **B**eam**s at LNS**) facility through the In Flight technique [32, 33]. A primary beam of $^{18}O^{7+}$ was accelerated at 55 MeV/u by the Superconducting Cyclotron (CS), and fragmented on a ^{9}Be target, 1.5 mm thick. Isotopes resulting from the fragmentation were then inserted into the *fragment separator* FRIBs, selecting ions with a rigidity of $\approx$ 2.8 Tm. For the purpose of the CLIR experiment, the same primary beam was used as a pilot beam to set up the magnetic fields of the dipoles of the spectrometer, for the optimization of the transport of the isotopes of interest (^{10}Be and ^{16}C). The *cocktail* beam

produced was then sent to the CHIMERA experimental hall. More details about the FRIBs facility and about the behavior and usage of fragment separators will be given in Sect. 2.2.
Before arriving at the hall, the beam passes through a *tagging* system, crucial for this setup, allowing the identification, event-by-event, of the isotopic components of the RIB. The tagging system used was the standard one developed for the CHIMERA beam line, consisting of a Micro-Channel Plate detector and a Double Sided Silicon Strip Detector (DSSSD) [34]. The identification method for the ions of the cocktail beam is based on the ΔE-ToF technique: in this case the start of the time-of-flight is given by the MCP detector, while the stop of the ToF is measured by the DSSSD, placed $\approx$ 12.9 meters apart. The DSSSD is also used for the measurement of the energy loss and spacial distribution for each isotope of the cocktail beam. More details on the specifics of the tagging system will be given in section 2.3.
Inside the experimental hall, the CHIMERA (**C**harged **H**eavy-**I**on **M**ass and **E**nergy **R**esolving **A**rray) multidetector was housed [35]. CHIMERA is a multidetector of 1192 ΔE-E telescopic units, divided into a forward part (688 detection units) and a sphere (504 units), covering the backward angles. For this experiment, two different reaction targets were used: a polyethylene CH_2 and a ^{12}C target. The target was placed at about 2 m after the DSSSD tagging detector, in the centre of the sphere of CHIMERA. Moreover, CHIMERA was coupled with four FARCOS (**F**emtoscope **AR**ray for **CO**rrelations and **S**pectroscopy) telescopes [36, 37] placed at small polar angles between the forward part and the sphere. FARCOS is an array of detectors expanding the basic concept of a ΔE-E telescope, made of three different stages. In this case, due to the high angular and energetic resolution, the FARCOS array proved to be crucial for this analysis. More details on the detectors employed with this measure will be given in section 2.4 and 2.5.

2.2 The FRIBs facility at LNS

At Laboratori Nazionali del Sud of INFN (INFN-LNS) in Catania, since almost 25 years it has been possible to produce Radioactive Ion Beams (RIBs) for research purposes and exotic nuclear physics experiments. Initially, the

production of RIBs began with the EXCYT (**EX**otics with **CY**clotron and **T**andem) project [38], exploiting the ISOL method[1] [39, 40]. This was done by using the Superconducting Cyclotron (CS) *K800* of the LNS to accelerate primary beams, and a TANDEM linear accelerator to post-accelerate the radioactive ions produced on a thick fragmentation target. Since the early 2000s, the In-Flight technique was also developed at the LNS: the FRIBs@LNS (In Flight Radioactive Ion Beams at LNS) project was set in motion, thanks to the pioneering work of G. Raciti and collaborators [41], following the reconfiguration of the extraction line of the Superconducting Cyclotron as a *fragment separator*. The project aimed in particular to the production of RIBs at intermediate energies ($10\,\text{MeV/u} \leq E \leq 100\,\text{MeV/u}$), through the In-Flight fragmentation technique, by employing primary beams produced by the CS and impinging on a target placed on the beam line. More details on the production of radioactive beams through the In-Flight technique will be given in 2.2.1.

During its time of activity, FRIBs has been capable of producing many radioactive ion beams [19, 21, 42] by using stable primary beams as ^{12}C, ^{18}O, ^{20}Ne, ^{40}Ar, ^{58}Ni and ^{70}Zn with intensity up to 500 nA and power to 100 W. Nowadays the LNS are undergoing intense upgrade work, involving in particular the CS, the locale infrastructures, but above all the construction of the new FRAISE fragment separator [32, 33, 43] whose details will be explored in more detail in Appendix. A.

The fragment separator of the FRIBs@LNS facility is featured in the scheme of Fig. 2.1. It is made of two 45° dipoles, in the extraction line of the CS, as shown in the map of Fig. 2.2, downstream of the fragmentation target. On the beamline, three series of three quadrupoles are also present: between the production target and the first dipole ($Q_1 - Q_3$), after the first dipole ($Q_4 - Q_6$), and before the second dipole ($Q_7 - Q_9$).

After being produced, the ions of the cocktail beam are horizontally separated and selected depending on their rigidity $B\rho$. The momentum acceptance $\Delta p/p$ in the case of FRIBs, determined by the opening of the dipoles,

[1] The ISOL (**I**sotope **S**eparation **O**n-**L**ine) technique [39, 40] consists in the production of radioactive ions through the collision between a stable beam, generally protons or light ions, accelerated by a primary accelerator, on a thick target, with the subsequent production of a multitude of isotopes which remain blocked inside the target itself. Isotopes are then extracted from the target through a chemical-physical processes and subsequently accelerated by a secondary accelerator, to be sent to the experimental halls to obtain RIBs also with energy in the order of MeV/u.

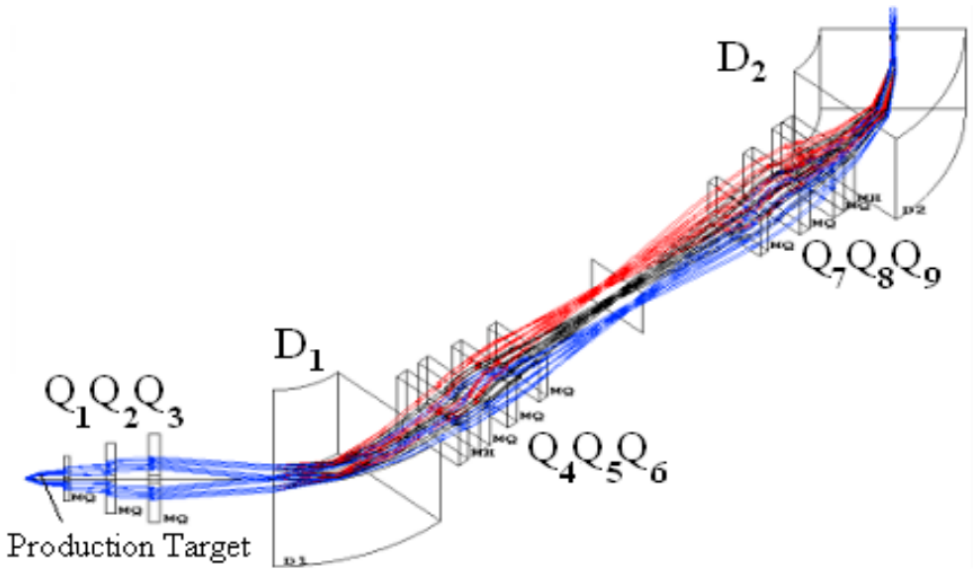

FIGURE 2.1: Scheme of the standard layout for the FRIBs fragment separator at LNS. The two 45° dipoles (D_1, D_2) are shown, with triplets of quadrupoles (Q_{1-3}, Q_{4-6}, Q_{7-9}) placed on the beamline to focus the beam [44].

is of $\approx$ 1%. This implies that when producing a cocktail beam, many beam components with approximately the same m/q ratio can be transmitted. On one hand, while this can be a disadvantage due to the presence of impurities other than the desired component, on the other hand, it can prove to be an advantage since it would be possible to work simultaneously with different radioactive beams, and so conducting more than one analysis with the same cocktail beam.

2.2.1 Radioactive beams production with In-Flight technique

As said previously, the production of RIBs at the FRIBs@LNS facility is based on the In-Flight fragmentation technique. According to this method, Radioactive Ion Beams are produced through the fragmentation of an accelerated heavy ion beam, after reacting with a thin target. The produced beam (so called *cocktail beam*) is therefore composed of different species travelling at approximately the same velocities as the ions of the primary beam, thus no re-acceleration is necessary. In order to trigger fragmentation reactions, the In-Flight technique involves the use of a primary beam with at least $E > 30$ MeV/u, impinging on a light target, generally made of beryllium or carbon.

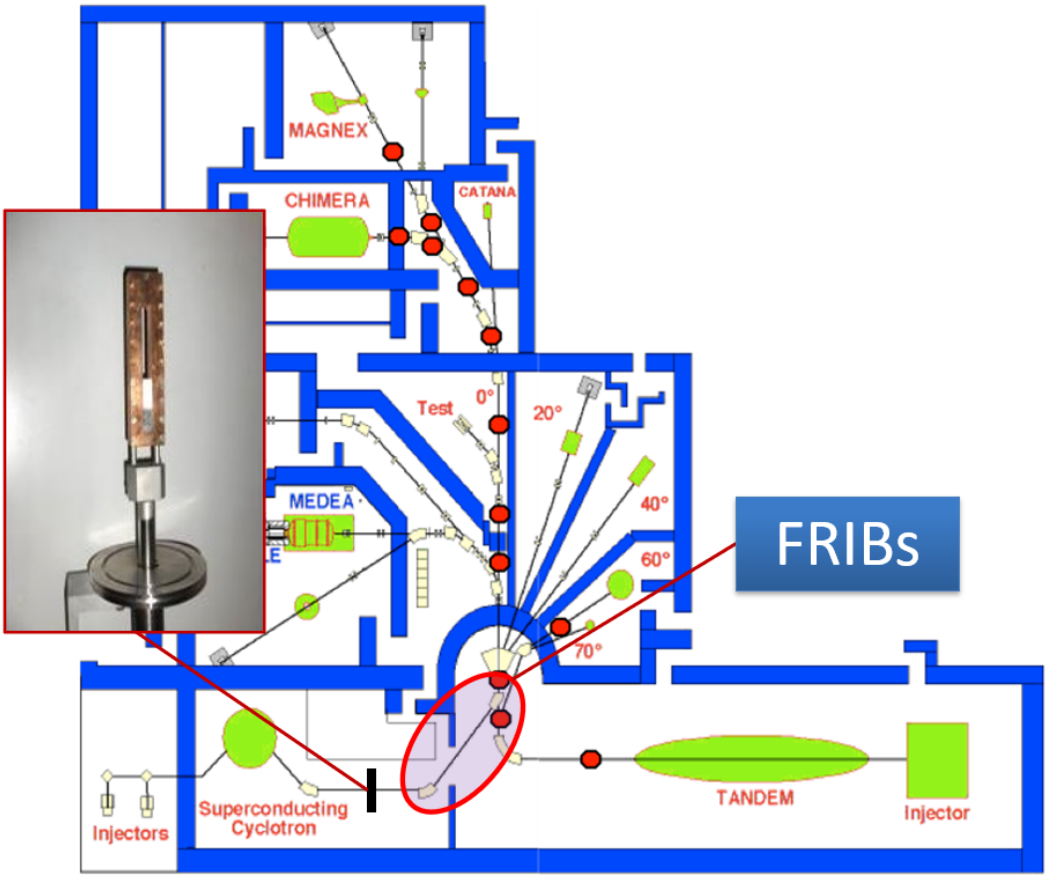

FIGURE 2.2: Map of the INFN-LNS. The positions of the fragment separator FRIBs (with its two 45° dipoles shown in red cycle) and the fragmentation target are shown.

At LNS, this is done by using the Superconducting Cyclotron *K800*, capable of accelerating ions between 20 MeV/u for heavier isotopes like $^{238}U^{38+}$ and to 80 MeV/u for lighter ones, like protons or ^{4}He. The highest magnetic field that can be produced inside the accelerator is around 4.8 T, by two series of superconductive bobbins Nb-Ti, kept at 4.2 K while immersed in a liquid helium bath. Ions are generally produced by two ECR (Electron Cyclotron Resonance) plasma sources SERSE and CAESAR, which produce positively charged ions that are then injected inside the CS where they travel along a spiral trajectory with ever-growing radius, till they are finally emitted [32].
A fundamental component for the production cocktail beam is the fragmentation target, which is generally made of light ions, such as beryllium or carbon. The choice of such a light material is due to the fact that the fragmentation products, produced in inverse kinematics, are forward-focused in

a narrow cone, in order to reduce the amount of ions that are transmitted on the inside walls of the beam line. Not only the choice of the material, but also the thickness of the target influence the production of the cocktail beam. In particular, for intermediate energies, the thickness can vary from even just 100 μm up to a few mm, depending on the wanted production. The target in fact has to be thick enough to be able to produce a higher yield of the isotopes of interest, but thin enough to not stop the fragments produced or to not slow them considerably. In the case of FRIBs, the fragmentation target is a thin foil of beryllium, for which different thicknesses are available (250, 500, 1000, 1500 μm), mechanically inserted inside the beamline whenever a radioactive beam has to be produced. Moreover, due to high beam currents, the fragmentation target is also cooled, to avoid its damage due to heat.
Impinging ions are then fragmented and inserted inside the *fragment separator*, in which magnetic fields and mechanical devices are used to separate unwanted components from the cocktail beam of interest or to focus the beam produced [45, 46]. Magnetic dipoles are essential for the transport of the beam, being able to select and transmit only ions with p/q within a momentum acceptance $\Delta p/p$, given by the width of the aperture of the magnetic dipoles. In general, a charged particle in motion with velocity $\vec{v}$ and charge q in an electromagnetic field, experiences a Lorentz Force given by the equation:

$$\vec{F}_L = \frac{d\vec{p}}{dt} = q\left(\vec{E} + \vec{v} \times \vec{B}\right); \tag{2.1}$$

from which it is possible to obtain the trajectory of the ion. If the electric field $E = 0$ and a homogeneous magnetic field is applied with $\vec{B} \perp \vec{v}$, the ion follows a circular path with radius ρ given by the equation:

$$B\rho = \frac{p}{q}; \tag{2.2}$$

with $B\rho$ defined as the magnetic rigidity. By setting the correct value of the magnetic field for the dipoles, or, in terms of beam transmission, the correct $B\rho$ value, it is possible to select only the charged particles that equal this value within the acceptance $\Delta p/p$ of the dipole. To obtain the best conditions for the separation of ions, a required feature for the fragment separator is the *achromaticity*. This is obtained when the spectrometer is made of two

different branches, symmetrical to each other with respect to a central axis. While the ions of the cocktail beam are separated, due to their different p/q ratio, in the first half of the spectrometer, they are recomposed in the second half, obtaining the most horizontal dispersion at the symmetry plane and mirror image of the incoming beam. In this case, then, selecting a specific rigidity of the dipoles $B\rho_0$, only the ionic species with rigidity inside the interval of acceptance $\Delta p/p$ will pass through the fragment separator, resulting in an automatic filtering of unwanted ions. Other magnetic elements used in a fragment separator are magnetic quadrupoles or poles of higher order, necessary to focus the beam, also symmetrically arranged as the magnetic dipoles between the branches of the fragment separator. However, this method, depending on the radioactive beam to be produced, may sometimes not be entirely sufficient, for which the use of *degraders* is also sometimes employed. Since different ions lose energy inside the same material differently by their charge and mass, a material can be used to slow down the ions of the cocktail beam and change their p/q ratio. Then, setting the rigidity of the dipoles after the degrader accordingly, a better separation of the ion can be obtained, improving the selection of desired species. This comes however at the cost of a worse energy resolution of the desired beam, since at this point straggling effects occur on the material of the degrader, which can be more or less thick.

2.3 The tagging system

In the context of a fragment separator, the tagging system is a device necessary to identify the ions of a cocktail beam produced by fragmentation technique. It has a double importance, whereas during the experimental phase it is used as a diagnostic tool to identify the products *in-flight* and verify the quality of the radioactive beam, while during the analysis it can be employed to identify, event-by-event, the ion reacting with the target in the experimental hall, and so allowing the selection of a particular beam of the cocktail produced. One of the methods employed in the context of the FRIBs facility is the ΔE-ToF technique. This technique exploits the fact that different ionic species, therefore ions with different mass A and charge Z, have different Time of Flight (ToF) through the same beam line and energy losses through the same material.

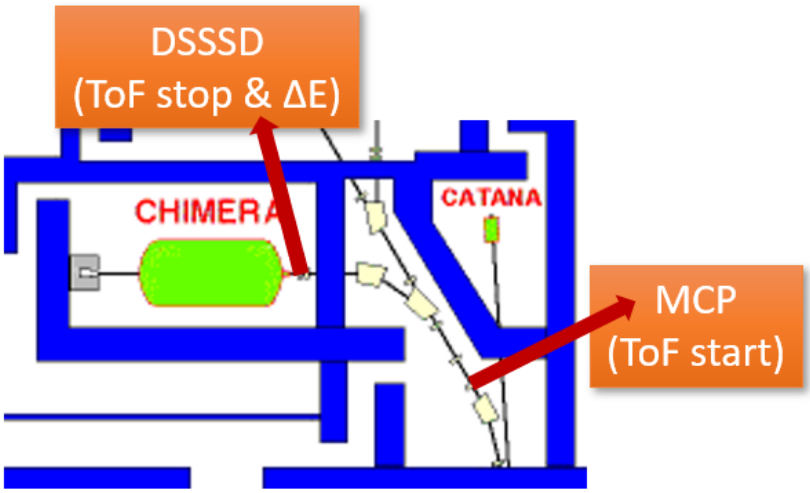

FIGURE 2.3: Map of the CHIMERA beam line. The position of the tagging system is shown: the MCP detector, gathering the start of the ToF, and the DSSSD, 12.9 m apart, gathering both the stop of the ToF and energy loss ΔE.

The tagging system of FRIBs, used for the CHIMERA beam line, is made of a Micro Channel Plate (MCP) detector and a Double Sided Silicon Strips Detector (DSSSD), allowing the identification of the cocktail beam ions through the ΔE-ToF technique. Fig. 2.3 shows the positions on the beam line of the tagging system detectors.

The MCP detector (Fig. 2.4) produces the signal of the start of the time-of-flight (ToF). It consists of a 700 μm thick micro-channel glass of $43 \times 63\ mm^2$, mounted on a chevron configuration. A 2 μm aluminized mylar sheet coated with a LiF film serves the function of electron source. The electrons, emitted when the beam passes through the material, are driven by an electric field to the upper part of the MCP glass. The electron drift region consists of a metal box, which supports a grid biased at the same voltage of the upper surface of the MCP, having a lateral opening to allow the passage of the beam. The bias voltages are provided by a resistive divider, in particular to the emitting foil ($V_f \approx -4200V$), the grid ($V_g \approx -2300V$) and rear side ($V_r \approx -300V$). Fig. 2.4 shows the MCP detector, mounted on its custom support on an ISO-DN flange, equipped with a mobile piston to extract it from the beam line if necessary. Moreover, the MCP detector is also able to sustain a rate of up to 10^6 pps, without degrading its efficiency or resolution.

The Double Sided Silicon Strip Detector (DSSSD) is a silicon detector mounted

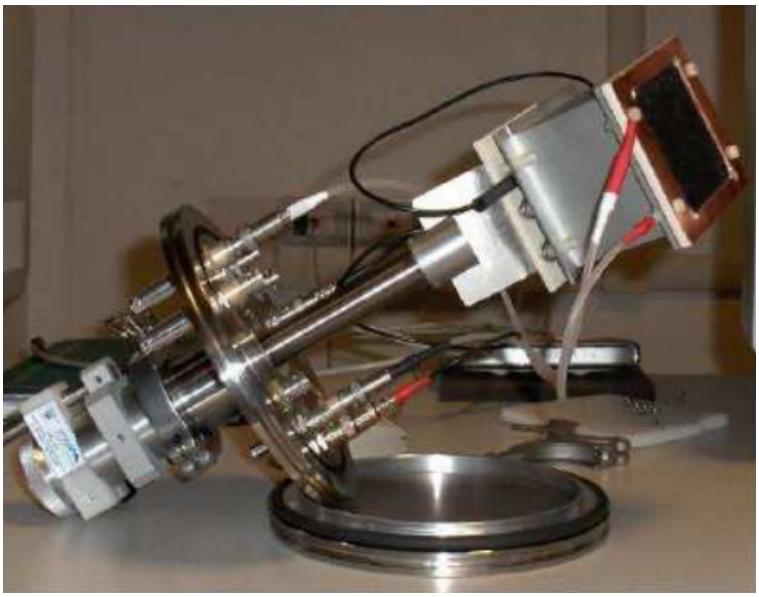

FIGURE 2.4: Picture of the Micro Channel Plate detector mounted on its dedicated ISO-flange. It is also equipped with a piston system to extract the detector from the beamline. Photograph from [34].

just 2 m before the reaction target in the CHIMERA hall, and approximately 12.9 m after the MCP detector. It provides both the stop of the ToF and the energy loss ΔE of the ions of the cocktail beam. It is made of a monocrystal of silicon, with two layers of electrodes, forming a grid of 32×32 strips on the front and back sides, 2 mm wide, with a thickness of 156 μm. For the measurement of the time-of-flight, signals are gathered by TDCs working with a common stop mode for both the start of the MCP and stop of the DSSSD, therefore working with an inverted logic by using the MCP signal to stop the TDCs. The whole system shows a good ToF resolution of about 500 ps FWHM.

For the identification of the ions of the cocktail beam a simulation of the whole FRIBs facility from the fragmentation target to the experimental hall and the tagging system has been developed by means of the LISE++ software[2] [47]. Fig. 2.5 shows a ΔE-ToF plot produced from a simulation of the production of a cocktail beam by reproducing the experimental setup and

[2]LISE++ is a software designed for the simulation of the production of radioactive beams produced and collected in fragment separators. Thanks to its many features, from calculations of cross sections, reaction kinematics, effects of energy loss and trajectories through electromagnetic fields, it allows to simulate the full production of RIBs and can be used both for the planning of an experiment and for the tuning or the calibrations of real devices.

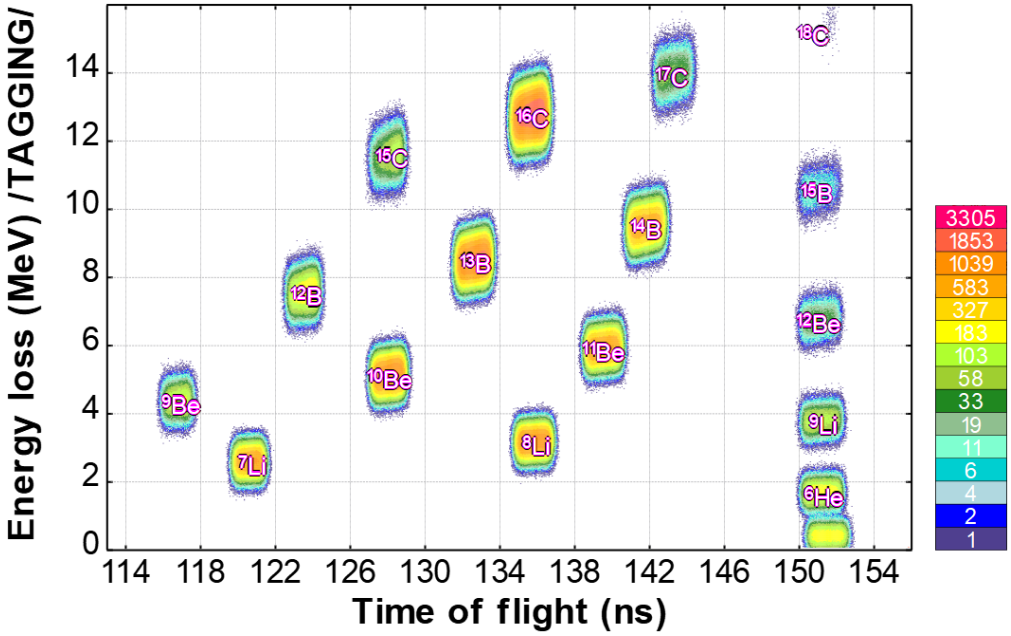

FIGURE 2.5: $\Delta E - ToF$ plot obtained by simulation on LISE++ software, reproducing the experimental settings of the FRIBs facility. Several isotopes can be recognized.

the beam condition for the CLIR experiment. The simulation was then used to calibrate the tagging system: this was done by performing linear calibrations for both the ΔE and ToF, by plotting the corresponding values for the centroids in energy loss and time-of-flight obtained from the simulations (in MeV) as function of the experimental values (in channel). Fig. 2.6 shows an example of a linear calibration obtained for the strip 15 of the DSSSD for both ΔE (Left) and ToF (right). Moreover, in Fig. 2.6 (bottom) the relative errors of each point from the intercept line are plotted. By performing a linear regression for each strip, in both energy loss and ToF, a calibration set of parameters was obtained for each strip, allowing to obtain a general ΔE-ToF plot, shown in Fig. 2.7. Several species can be identified, i.e. ^{6}He, $^{7,8,9}Li$, $^{9,10,11,12}Be$, $^{12,13,14,15}B$ and $^{16,17}C$.

The DSSSD can be also used to produce distribution plots for each ion of the cocktail beam. This is done by developing cuts for each vertical front strip of the detector and for each ion of the beam, allowing to produce distributions of the ions per strip as the one shown in Fig. 2.8.

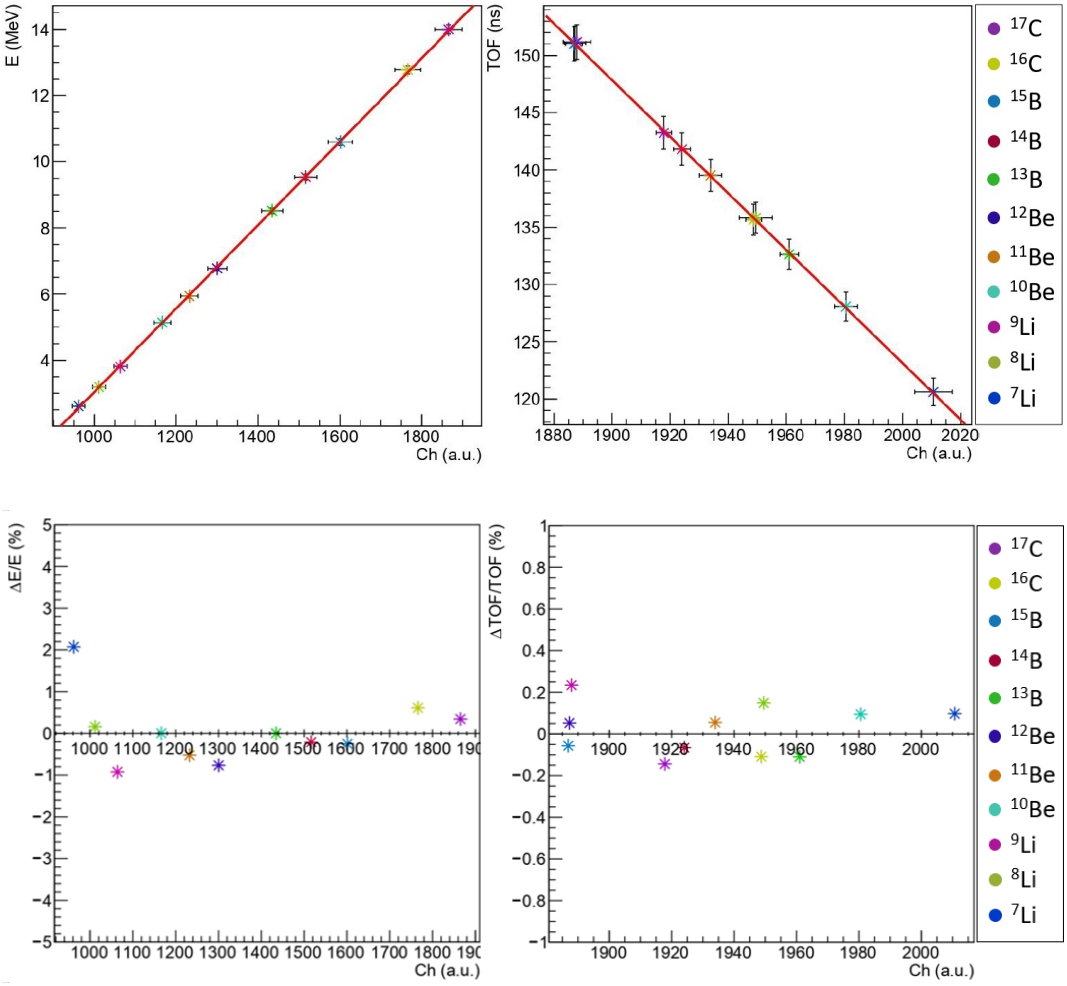

FIGURE 2.6: Top: Linear calibration plot for ΔE (left) and ToF (right) for the strip 15 of the DSSSD. Each point in the plot corresponds to the position in channel and in energy loss or time-of-flight, obtained by simulation, for many ions of the cocktail beam. Bottom: Relative error for each point of the plots shown on top side, respectively for the energy loss (left) and time-of-flight (right) of the strip 15 of the DSSSD.

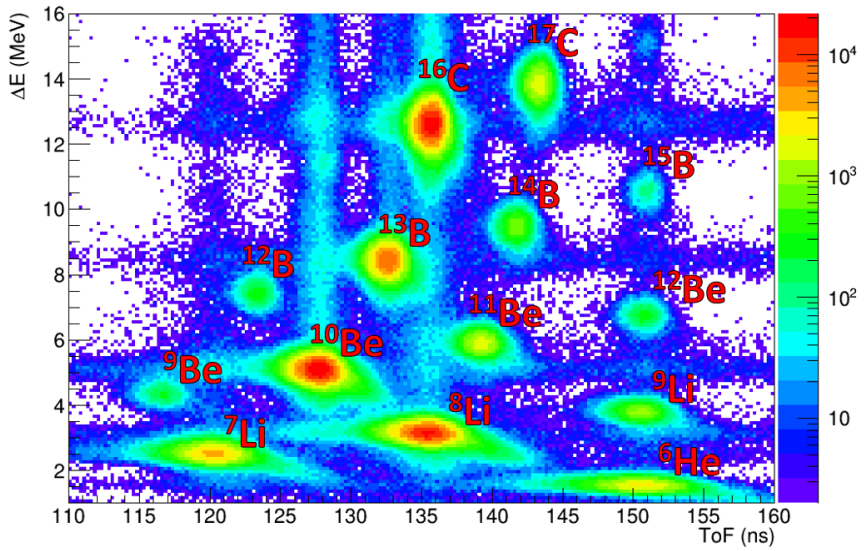

FIGURE 2.7: ΔE-ToF calibrated plot obtained for each strip of the DSSSD.

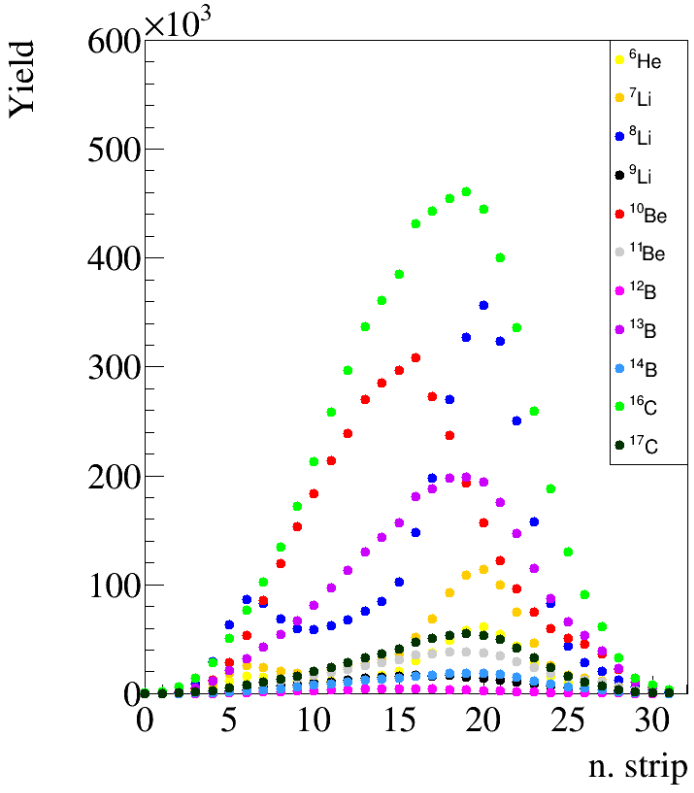

FIGURE 2.8: Distribution of the ions of the cocktail beam, obtained by using graphical cuts on the calibrated ΔE-ToF plot for each strip of the DSSSD tagging detector.

2.4 The CHIMERA multidetector

The CHIMERA (**C**harged **H**eavy-**I**on **M**ass and **E**nergy **R**esolving **A**rray) apparatus is a 4π multidetector installed at INFN-LNS [35]. Since the early 2000s, the aim of the detector has been the study of the physics behind heavy ion collisions and reaction mechanisms, mainly at Fermi energies (from 15 MeV/u to 100 MeV/u). Since then, a great multitude of experiments have been performed, investigating reaction dynamics and isospin degree of freedom in specific reactions such as neck fragmentation [48, 49], exotic clustering formation [20, 22], fusion and fission reactions [49, 50, 51], making it a lively and profitable tool.
The CHIMERA multidetector is made of 1192 telescopic units, arranged in a 4π geometry. Each unit consists of a silicon detector, about 300 μm thick (about 200 μm for the most forward part), followed by a CsI(Tl) scintillator crystal, with a thickness ranging from 3 cm at backward angles to 12 cm for the most forward angles, coupled to a photodiode. The whole detector is divided in two main parts:

- The forward part, made of 688 telescopes, covers the polar angles θ around the beam axis from 1° to 30°, with full 2π azimuthal symmetry. Detectors are grouped into 9 wheels, arranged in conical geometry, and each one of them is placed on horizontal supports that allow their independent movement. Each wheel is divided in 2 rings, *inner* and *outer*, with different granularity depending on the polar angle. Telescopes are placed at a large distance (350 to 100 cm) from the reaction target, in order to have a good time-of-flight measurement base.
- The backward part is made by 504 telescopes, arranged as a sphere of 40 cm radius, divided in 17 different rings, covering angles from 30° to 176°, with a full 2π azimuthal coverage. The reaction target is placed at the centre of the sphere.

2.4.1 Identification techniques with CHIMERA

The CHIMERA multidetector uses various techniques for the detection of ions and particles, to measure their energy and velocity and to identify them in charge and mass. Here, the various methods employed from its creation up to now are summarized:

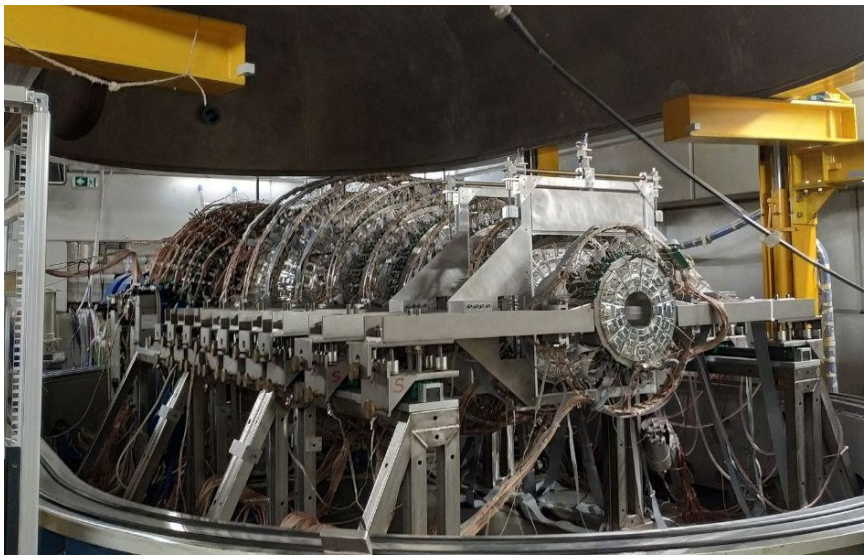

FIGURE 2.9: Photo of the CHIMERA multidetector installed at INFN-LNS. The 9 forward rings and the sphere are clearly visible [14].

- The ΔE-E technique. This uses the signals from the Si (energy loss, ΔE) and CsI(Tl) (residual energy) detectors, to build a matrix. This technique allows the charge and mass identification of the fragments punching through the silicon detector;
- The Pulse Shape Discrimination (PSD) in CsI(Tl) detectors. In the case of the CsI(Tl), by plotting the fast and slow components of the light produced in the scintillator, it is possible to identify in charge and mass the ions stopped inside the detector, with $Z \leq 4$, as well as γ-rays with an efficiency up to 60%.
- The PSD in Si detectors. In this case, the rise time of the signal can be used to gain information on the particles and ions stopped in the Si detector, to perform identification in charge and mass.
- The Time-of-Flight (ToF) technique. This technique, exploiting the time employed from the particle to travel from the target to the detector, provides the direct measurement of the velocity of all the reaction products and also the mass identification of ions stopped inside the Si stage.

Fig. 2.10 summarizes the different techniques, showing a ΔE-E plot, for Si-CsI telescopes (full matrix on top, in which it is evident the charge identification, and a zoom, on the bottom, on the part of the same plot where the light

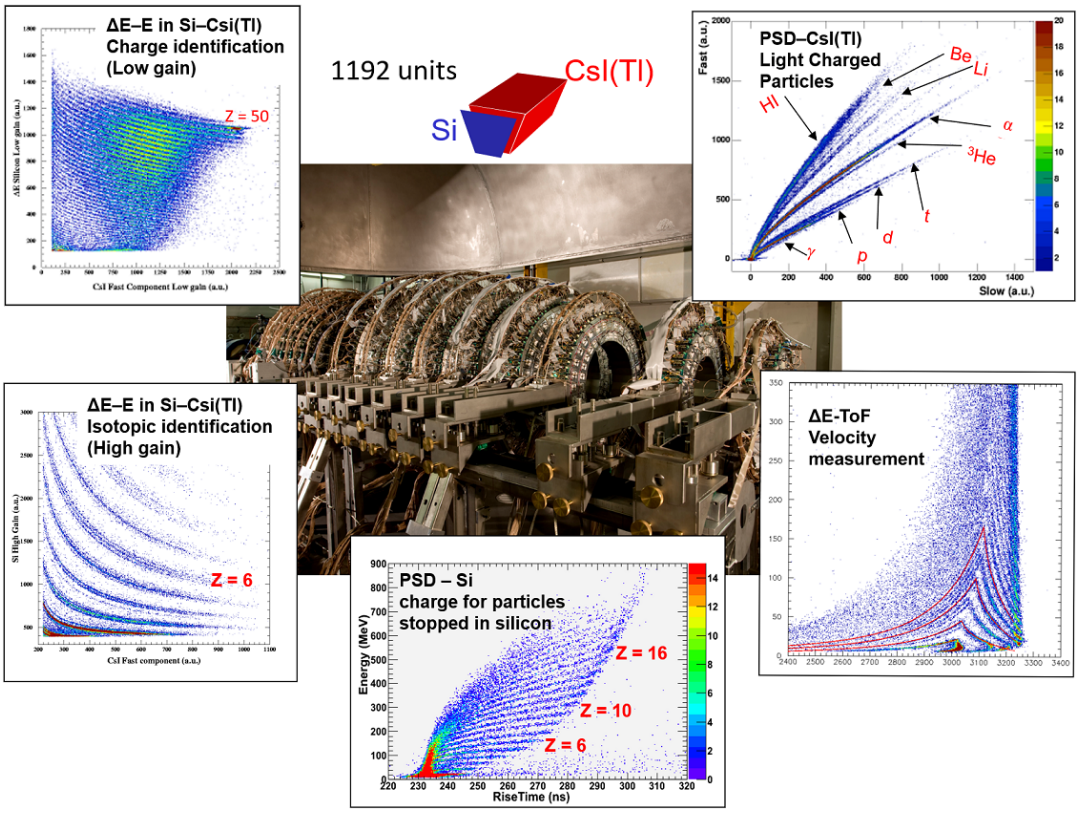

FIGURE 2.10: Various detection techniques for the CHIMERA 4π multidetector. On the left, two ΔE-E plots are shown respectively for Low and High-gain for the ^{124}Sn + ^{64}Ni (35 MeV/u) reaction. On the right, PSD identification in CsI(Tl) scintillators, allowing to identify Light Charged Particles (LCP) up to Be, and ΔE-ToF identification. On the bottom, PSD technique applied on CHIMERA Si detectors. Figure adapted from [14].

reaction products lie, in which it is possible to observe good mass discrimination), a PSD Fast-Slow plot for CsI(Tl) detectors, an E-Rise time plot for the PSD technique in Si detectors, and a ΔE-ToF plot.

The ΔE-E method

The ΔE-E technique is an identification technique that can be applied when a particle loses energy in the first stage of the telescope (the silicon detector) and the releases the residual energy in the scintillator (the fast component of the CsI(Tl) signal). In this way, since different ions have different stopping powers inside the same detector, the partition of the total energy $E_0 = \Delta E + E_{res}$ becomes different, producing a characteristic matrix like the one shown in Fig. 2.10 (top left), for the reaction ^{124}Sn + ^{64}Ni at 35 MeV/u.

From the example it is possible to see charge ridges clearly separated, for which a charge identification technique can be applied. The procedure is based on the Bethe-Block formula, used to fit correlations between the energy loss on Si (ΔE) with the remaining energy (E_{res}) as a function of Z and A. In the case of light ions, the specific energy loss dE/dx of a charged particle of mass A and charge Z depends on the characteristics of the absorbing material, such as density and atomic number. This can be written as:

$$\frac{dE}{dx} = \frac{Z^2}{f(E/A)} \tag{2.3}$$

From this equation, through analytic reductions and approximations, such as that $A = 2Z$, N. Le Neindre et al. [52] obtained a much exploitable formula to work with, parametrized by a 7 parameters functional, expressed in the form:

$$\Delta E = \left[(gE)^{\mu+\nu+1} + \left(\lambda Z^{\alpha} A^{\beta}\right)^{\mu+\nu+1} + \xi Z^2 A^{\mu} (gE)^{\nu} \right]^{1/(\mu+\nu+1)} - gE. \tag{2.4}$$

where μ, ν, λ, α, β and ξ are free parameters related to the characteristics and non-linear effects of the telescope detectors, while the g parameter accounts gain ratios of the ΔE and E signals. Moreover, two other parameters have to be included in the fit, to take into account the offset values upon the ΔE energy loss on the Si detector and the *fast* value on the CsI(Tl) one, for a total of 9 parameters. Some discrepancies can be expected at higher masses, for which the assumption $A = 2Z$ is no longer valid, and at low values of E_{res}, for which the non-linear response of the CsI(Tl) becomes more evident. Therefore, by performing a multiparameter fit simultaneously over different ridges for many isotopes of defined Z and A, a set of 9 parameters is obtained for the whole matrix, allowing to identify with good resolutions the masses of the ions. This procedure is performed on each used telescope, allowing us to perform event-by-event identification, to finally obtain the charge and mass of the impinging ion.

The ΔE-ToF method

The ΔE-ToF technique allows to determine the velocity of the fragments, while also serving as a method to identify in mass the ions stopped inside

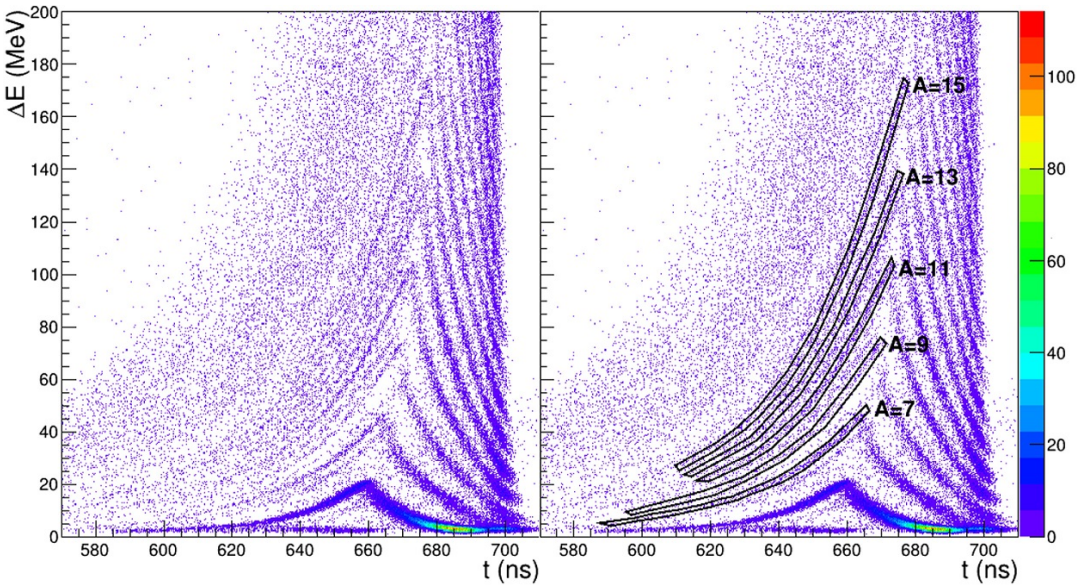

FIGURE 2.11: ΔE-ToF plot for a CHIMERA silicon detector, placed at about 210 cm from target and covering polar angles in the range $8.5° - 10°$, for the reaction $^{124}Xe + ^{64}Ni$. Ridges corresponding to different isobars can be distinguished. On the right panel, same as left one, graphical cuts are used to indicate particles of atomic mass number $A = 7, 9, 11, 13, 15$. Figure taken from [53].

silicon detectors [53]. Signals produced in CHIMERA's silicon detectors are treated by wide-dynamic-range fast Charge Sensitive preamplifiers (PACs) of 15-20 ns rise time. After passing through preamplifiers, the signal is sent to 16 channels NIM amplifiers, divided in two sections, the first one is dedicated to the energy output, while the second one is dedicated to the timing and multiplicity signals. The timing signal is differentiated with two different Constant Fraction Discriminator set at two different fractions, 30% and 80%: the first one, also delayed by 30 ns with a typical resolution of 250 ps/ch, is used as start signal in Time-to-Digital Converters (TDCs) to evaluate the Time-of-Flight with respect to the stop signal given by the Radio-Frequency of the CS, in reverse logic; the second one, delayed by 150 ns and with the same resolution of 250 ps/ch, is evaluated with respect to the same Radio-Frequency signal to evaluate the rise-time of the signal, which provides the time when the signal reaches the 80% of its maximum. The difference between the output signals from the two CFD is proportional to the rise time.
Fig. 2.11 shows a ΔE and ToF correlation plot for CHIMERA silicon detector for the reaction $^{124}Xe + ^{64}Ni$ at 35 MeV/u. From Fig. 2.11 two different cases

can be examined: particles stopped inside the detector, on the left region of the plot with $t \lesssim 660 - 680$ ns, and particles punching through the silicon detector and arriving on the following CsI(Tl) detector. In particular, for the first case, since the full energy is given by the silicon detector signal, by using non-relativistic kinematics, it can be said that:

$$E = \frac{1}{2}Mv^2 = \frac{1}{2}\frac{Ml^2}{(t_0 - t)^2}; \tag{2.5}$$

where M is the mass of the impinging ion, l is the distance travelled by the ion in cm, t is the time measured in ns, while t_0 is a value taking into account the time delay due to the length of the cables and front-end electronics processing the RF signal, and including the RF signal phase. From this equation, the mass identification of the particles can be obtained from the formula:

$$M = \frac{2(t_0 - t)^2 E}{l^2}; \tag{2.6}$$

and so proving that the different ridges in the left region of Fig. 2.11 correspond to different masses. The calculation of t_0, in particular for particles stopped in the silicon detector, requires the application of a special procedure, well described in Ref. [53].

Pulse Shape Discrimination

Pulse Shape Discrimination (PSD) is a technique usually applied to discriminate between signals of different nature, to recognize the source of the radiation. In the context of the CHIMERA multidetector, this technique is applied in CsI(Tl) detectors, using the so called fast-slow technique, and in Si detectors, for particles stopped on the detector, through the Energy vs. rise-time analysis of the signals.
In the first case of CsI(Tl) scintillators, the technique is used especially to identify light charged particles, with $Z \lesssim 3$ for particles punching through silicon detector and so with an energy loss relatively small of less of 20 MeV. CsI(Tl) scintillators produce light through different physical processes, depending on the energy, charge and mass of the incident particle. These can be generally categorized into two different components, called *fast* and *slow*. In this way, light can be parametrized by a simple combination of the two

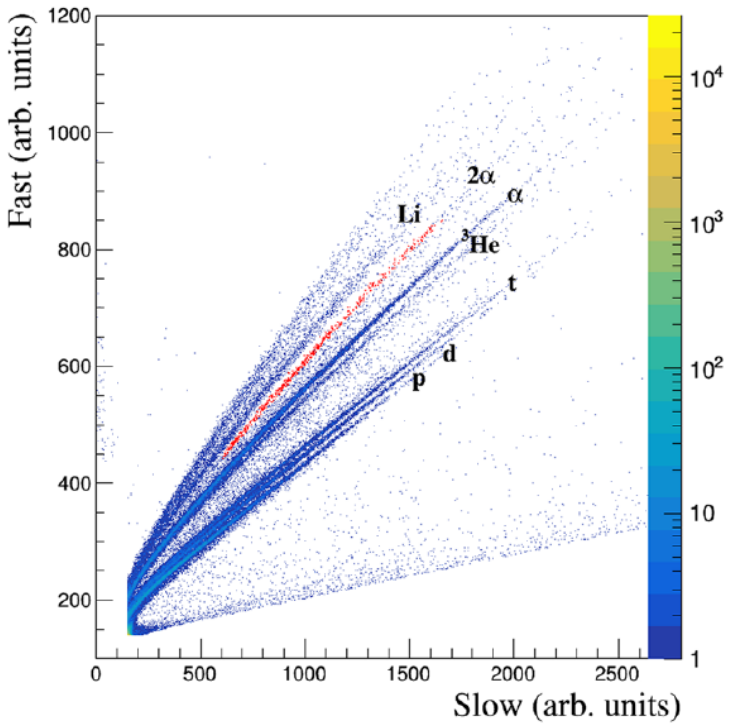

FIGURE 2.12: Fast–Slow identification plot obtained for a CsI(Tl) of the CHIMERA multidetector for the reaction ^{124}Xe + ^{64}Ni (35 MeV/u) at 34°. The red dots indicate the events labelled as ^{8}Be, or 2α. Figure taken from [54].

components, expressed as decreasing exponentials with different time constants, in the form of:

$$L(t) = A_1 e^{-t/\tau_1} + A_2 e^{-t/\tau_2} \tag{2.7}$$

with A_1 and A_2 the two amplitudes of the two fast and slow components, and τ_1 and τ_2 the decay time constants of the two different components. The combination of the two yields in these fast and slow components depends on the energy, charge, and mass of the incident particle, and is at the base of this technique. Typically, the two time constants have values of $\tau_1 \sim 0.4 - 0.7$ μs and $\tau_2 \sim 3.2$ μs, and the light output produced, collected by a photodiode and related electronic chain, keeps the information of them allowing to reconstruct the charge and mass of the detected particle. The light output is then sent to an amplifier, shaping the signal with a time constant of about 1-2 μs, thus maintaining the fast component unchanged while cutting off the slow component, influencing only the tail of the shape. In the case of CHIMERA

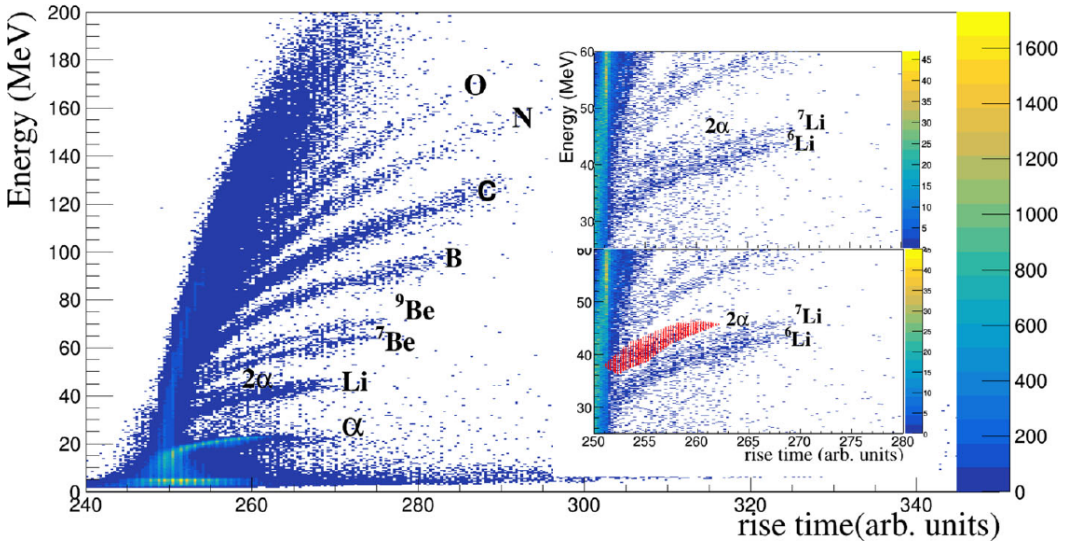

FIGURE 2.13: Energy and rise time scatter plot of particles detected in the reaction $^{78}Kr + ^{40}Ca$ (10 MeV/u). Different ridges can be associated with particles of different Z. In the insets: (bottom) zoom around the lithium region with red dots indicating the expected position of ^{8}Be ions (2α particles); (top) same as below without the red dots to better highlight the area. Figure taken from [54].

and FARCOS in the CLIR experiment, however, the signal produced is sent to two QDCs, and the single gate method is applied: while on one QDC the signal is stretched when it reaches the maximum value, on the other QDC it remains unchanged so by applying a cut on the tail of the signal it is possible to obtain the two components with a single gate.

Plotting one signal against the other allow to obtain an identification scatter plot, as shown in Fig. 2.12 in which several ridges can be observed, each one belonging to a different isotopic species. The same technique can also be employed for the detection of γ-rays, as they generate electrons in CsI(Tl) detectors that collide onto the ions of the scintillator lattice produce light, again with two different fast and slow components. Since these electrons have a very low relative stopping power compared to light ions, at the same energy of light ions they have a lower fast component and a bigger slow one, producing a ridge on a fast-slow plot just under the one of proton ridge.

PSD techniques can be applied also to Si detectors, to identify the ions that are not energetic enough to pass through the detector and are stopped. For these ions in particular it is known that their current pulses are dependent on

the mass A and charge Z of the stopped particle. In this case, the charge identification is obtained by correlating the energy of the detected particle with the rise-time of the produced signal. Similarly to the ToF case, the rise-time of the signal is calculated from the difference between the times obtained through two Constant Fraction Discriminator filters, respectively at 30% and 80%. Correlating the obtained rise-time with the energy of the ion, it is possible to obtain a scatter plot, like the one shown in Fig. 2.13, from which charge identification has been achieved for ions from helium to oxygen.

2.5 The FARCOS array

Over the years, the CHIMERA 4π multidetector allowed to obtain a long series of excellent results, especially in the field of multi-fragmentation and the study of the reaction dynamics at Fermi energies. This was achieved also thanks to a series of upgrades, aimed to satisfy primarily the experimental and physics needs that have constantly evolved over the past 20 years. One of these for example is the already mentioned upgrade for Pulse-Shape Discrimination for Silicon detectors, which has made it possible to lower the threshold for the simultaneous identification of mass and charge in light fragments, extending the use of the detector from multi-fragmentation to fusion reactions. In the context of the study of the reaction dynamics in heavy ion collisions, the characterization of events with 2 or more particles acquires particular importance, thus requiring both high angular and energetic resolutions.

For this purpose, the new FARCOS array was designed and created within the CHIMERA collaboration [14] and financed by INFN-CNS3, in a joint project among INFN-Section of Catania, LNS, INFN-Section of Milan, Universities of Catania, Milan, and with the participation of international researchers. The FARCOS (**F**emtoscope **AR**ray for **CO**rrelations and **S**pectroscopy) correlator [36, 37, 55, 56, 57] is a detector designed as a compact high-resolution array for the measurement of particle-particle correlations, spectroscopic and femtoscopic studies, and applications connected. In its final project, the FARCOS array consists of 20 units, or telescopes, arranged in a compact configuration. A detailed description of the performances of the FARCOS detector will be the object of an article in preparation. Each telescope is made of three different stages:

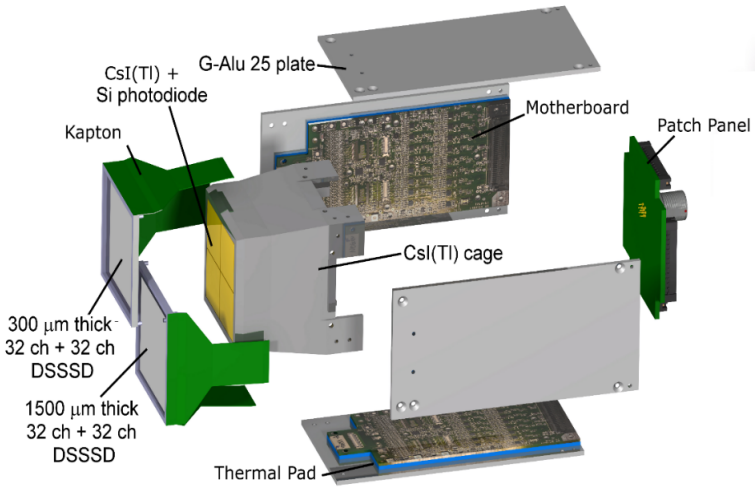

FIGURE 2.14: Expanded 3D model scheme of the FARCOS detector. Figure taken from [14].

- The first two are Double-Sided Silicon Strip Detector (DSSSD) respectively 300 μm and 1500 μm thick, constituted by 32 strips on the front side and 32 strips on the backward side, respectively in the horizontal and vertical directions, each one 2 mm wide, for a total detection area of 64×64 mm^2. The total geometrical dead area of the DSSSD, due to the inter-strip regions, where silicon oxide is deposited (25 μm on the junction front side and 40 μm on the ohmic back side), amounts to about 3% of the total area [58]. This, with a width per strip of 2 mm, is considered as a good compromise between granularity and efficiency loss.

- The third stage is made of four CsI(Tl) scintillators, of trapezoidal shape, 32×32 mm^2 front surface, 39.5×39.5 mm^2 back surface, 60 mm length. The CsI(Tl) crystals are wrapped with a 0.12 mm thick white reflector and a 50 μm aluminized Mylar, while the front face of the crystal is covered with only a 2 μm aluminized Mylar foil. The light produced by each crystal is readout by a photodiode (Hamamatsu model S-3204-08, 18×18 mm^2). This stage in particular serves the function of a calorimeter, needed to totally stop high-energy particles.

A single FARCOS telescope then requires 132 different readout channels. For this reason, a versatile multichannel CMOS frontend was developed, with a selectable full-scale energy range from 100 MeV up to 2.2 GeV. Moreover, in collaboration with Politecnico di Milano, compact pre-amplifiers have been

designed, with high channel density, based on ASIC technology. An energy resolution of about 20 keV FWHM can be achieved on both the DSSSD stages, as obtained in previous measurements [36], with an angular resolution at 1 m from the reaction target of about 0.1°. Due to the granularity of both front and back strips of the silicon stages, it is possible to measure with a good resolution the couples or triplets of particles emitted at small angles with small relative impulses. Thanks to the presence of the different stages, many techniques can be applied for the analysis of the fragments detected by the array, which will be described in the next sections. Moreover, thanks to its rather small size, a FARCOS telescope can be also used as a standalone detector or coupled with other detector systems, as in the present case of the CHIMERA multidetector.

The FARCOS telescopes show excellent characteristics, ideal for the study of particle-particle spectroscopy, in which high precision is required for an accurate reconstruction of the event of the reaction.

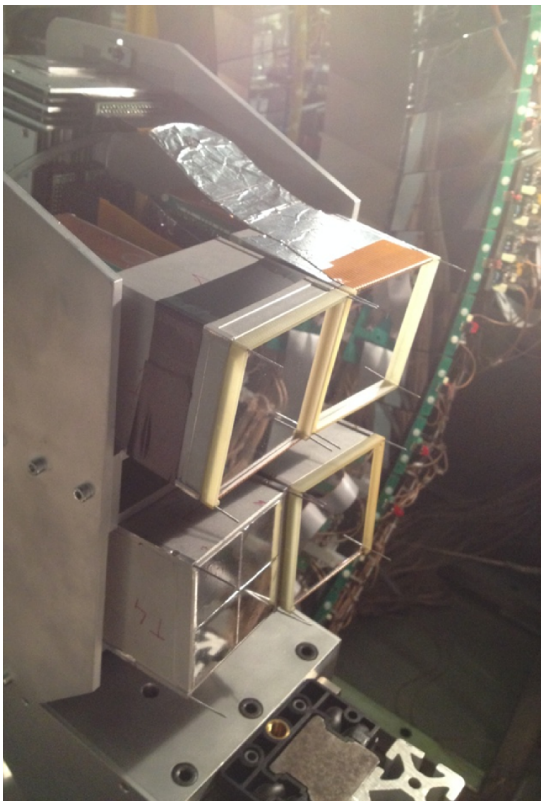

FIGURE 2.15: Photo of the four FARCOS telescopes during their assembly for the CLIR experiment. For the bottom left telescope, the four CsI(Tl) scintillators are still visible, covered by a mylar protection sheet.

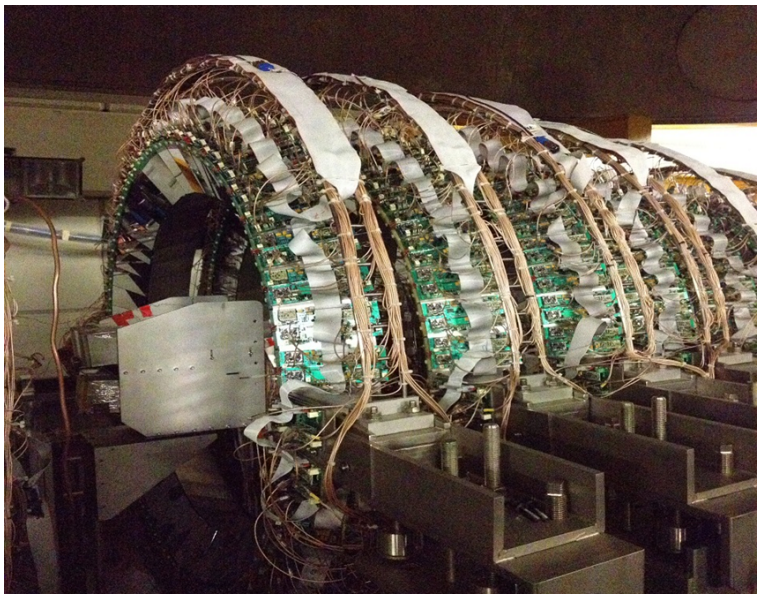

FIGURE 2.16: Photo of the final configuration for the four FARCOS telescopes, mounted on a support covering small azimuthal angles. The CHIMERA forward rings are also visible.

2.5.1 Characterization of FARCOS DSSSDs

During the experimental phase, both the 300 μm and 1500 μm stages have been used to gather data. However, while the 1500 μm DSSSDs were equipped with the full electronics, allowing to gather data for both the front and back side strips of the detector, the 300 μm stages were equipped only with the electronics for the front sides. In the case of the analysis developed for the CLIR experiment, the energy loss value of the ion inside the detector is assumed by the DSSSD front side. The back side of the second stage DSSSD had a double purpose:

- It is required for the tracking of the incident ion. Given a matrix of 32 $\times$ 32 strips front and back, a DSSSD can be thought as a grid of 1024 "virtual" pixels, for which both θ and ϕ angles are known, empirically calculated before the experiment. By firing both a front and a back strip, the correct polar coordinates with respect to the reaction target can be obtained, required for the calculation of the momentum of the incident ion.
- It can be used to reject background noise events. In principle, when a particle passes through the detector, the same energy loss signal is

gathered by both the front and back strips. In practice, this is not always true, since the difference E_{diff} between the energy loss E_f on the front strip and E_b on the back strip is not 0 and depends on many factors, mainly by the electronics. In this way, by comparing the energy loss values between a front and a back strip, it is possible to understand if the event is a real event or a noise one.

The back side of the detector also helps in the characterization of the event when multiple strips are fired in the same DSSSD. The assignment of the correct front strip to the back and vice-versa is in fact a common problem to DSSSDs. When multiple ions hit the same detector inside the same trigger window, multiple signals are produced on both the front and back side strips, thus preventing to understand in which "virtual pixels" the particles have passed through and therefore not being able to correctly identify the θ and ϕ polar angles. For this reason an algorithm has been developed to solve the assignment problem of *front* strip events to *back* strip events. From the E^2_{diff} difference between the energy values acquired by the front and back strips, the algorithm chooses the best possible configuration of association of strips that minimize that value, by comparing all the various possible front/back pairing.
Moreover, having two different sets of strips in the same DSSSD is also helpful to reconstruct interstrip events, i.e. events in which the electronic cloud of the incident ion fires two adjacent strips, partially depositing its energy on both of them. Through geometrical considerations, in the case of the FARCOS array DSSSDs, such events are at least $\approx 3\%$ for both front and back sides, which can be recognized and reconstructed through the other reciprocal strips.

2.6 The electronic chain

In this section the electronic chain used during the CLIR experiment will be described. It should be however worth underlying that the configuration used in this setting was especially preliminary for the FARCOS configuration, as it was changed during the years. More details on the current configuration of the electronics, especially for the FARCOS arrays will be given in 2.6.1. The electronic chain used for FARCOS during the CLIR experiment is essentially the same of the CHIMERA detector, with some small differences

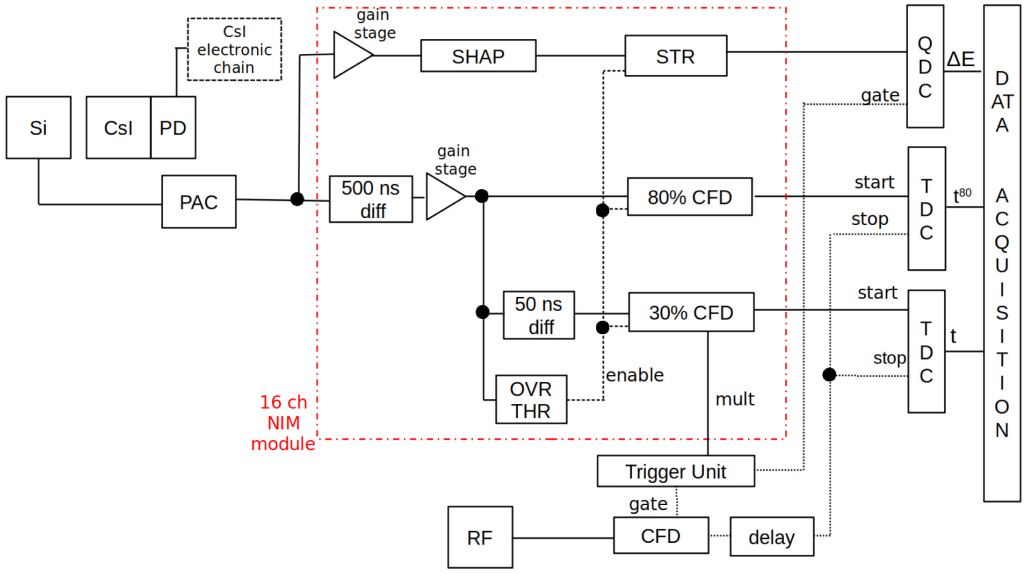

FIGURE 2.17: Scheme of the electronic chain used for the FARCOS array to process signals produced by the silicon detectors and CsI(Tl) scintillators. Figure taken from [53]

depending on the ring and on the type of detector, if a silicon one or a CsI(Tl). Since FARCOS was the main detector analyzed for this analysis, whose presence in the CLIR experiment also represented a first test in a real experiment, in this Section we will focus only on its electronics. A summary diagram of the electronic chain is shown in Fig. 2.17.

From each strip of the silicon detector of FARCOS a single signal is extracted, providing different information: the energy loss of the incident particle, the time signal of the arrival of the particle, used as the start of the ToF. This last information is just used for the best event selection. The electronic chain starts from the detector, whether it is a silicon one or a CsI(Tl), which signals are first processed by charge preamplifiers. These were made in collaboration with INFN-Section of Milan, specifically for this test. The FARCOS preamplifiers had 16 channels, and were positioned inside the CHIMERA chamber, under vacuum, at a short distance from the detector. The signal produced by the silicon detector is then integrated by the preamplifier and outputs a height signal independent on the capacitance, but proportional to the charge produced on the detector. While the rise time is of the order of 50 ns, the fall time is much slower, of the order of 200 μs. The output of these preamplifiers is sent outside the CHIMERA chamber through flanges, directly connected to the amplifiers. These consist of compact 16-channel NIM1568B modules

manufactured by CAEN. These modules have three sections: one amplifier and two Constant Fraction Discriminator set at two different fractions 30% and 80%. In the CLIR experiment the information relative to the 80% fraction signal is not present because of the missing of the TDC modules. The energy signal, after it is shaped by the amplifier, is sent to Charge-to-Digital Converters (QDCs), in order to be digitized and acquired. This is done however only if the trigger of the event responds positively to the opening of the signal acquisition gate. Moreover, two different output signals with different gain values can be produced: a low gain (LG) and a high gain (HG) signals, the latter one obtained by applying a factor $\times 8$. On the other side, in the same NIM1568B module, the same input signal is sent to the CFD. The 30% logical output is sent to a Time to Digital Converters (TDCs). Another output, the multiplicity signal, is sent to the trigger chain to a discriminator, which rejects or accepts the event depending on the conditions programmed for the "*OK EVENT*". To the same discriminator the radiofrequency of the CS is also sent, used to generate a gate for the QDCs of the silicon detectors, CsI(Tl) detectors for the fast and slow components, and the stop signal to the TDCs for the ToF. In the case of the TDCs, the start is given by the 30% CFD, while the 80% signal is also provided for the PSD. In fact, if both the TDCs for the 30% and 80% fractions are provided, one could calculate for the given event the rise time as $T_{rise} = T_{30\%} - T_{80\%}$.

The electronic chain for CsI(Tl) is essentially very similar to the one used for silicon detectors, although few changes need to be pointed out. Charge preamplifiers are designed by INFN-Section of Milan and produced by MICROTEL, while amplifiers are SILENA 16 channels NIM modules with 2 μs shaping time. These have a double output for the processing of the two components of the CsI(Tl) detectors, i.e. the *fast* and *slow*. Generally, the two components, integrated from the same CsI amplified signal, can be obtained by two gates, shifted to each other, integrating the peak and the tail of the signal to calculate respectively the fast and slow components. The technique used here however employs a common gate system for both components, reducing the costs of the modules to be used. The amplifier output signal is then split: one component remains unchanged, needed for the calculation of the slow component, while the other is stretched when it reaches the maximum amplitude. Outputs are then sent to two different QDCs that process the signal with a common gate enabled by the trigger chain, usually set for

the silicon detectors. Therefore, if an "*OK EVENT*" signal is produced, a single gate is produced for the integration of both components.

2.6.1 The new GET electronics

The electronics employed for the FARCOS array has undergone many changes over the years after the CLIR experiment. The electronics used for the array during the CLIR experiment were analog electronics, based on VME readout, with initial preamplifiers built specifically for the experiment. On the other side the electronic front-end of the CHIMERA CsI(Tl) detectors was becoming obsolete within the last 10 years of successful runs, and so it was decided to upgrade its electronics to a new system, capable of synchronizing with the old VME readout still in use for CHIMERA Silicon detectors. This is based on the new GET electronics. In this paragraph, the current FARCOS electronics will be briefly described, already in use for several years also for the CHIMERA CsI(Tl) signals.

The GET (Generic Electronic for TPC) electronic is a generic, reconfigurable electronics and compact data acquisition system, initially designed for gas-filled detector applications in nuclear physics and Time Projection Chambers (TPCs) [59]. It was initially developed to respond to the scientific community's need for high-density front-end electronics, capable of managing a large number of channels, even in the order of tens of thousands, capable of responding to external or internal triggers with low dead time and high acquisition rates. Although in general the GET system of FARCOS and CHIMERA responds to these canons, in our case the electronic chain has been slightly modified to respond to certain needs, first of all, the synchronization with the VME readout system, still in use for CHIMERA silicon detectors. The integration of this electronics required the creation of new preamplifiers, both for the DSSSD and for the CsI(Tl) of FARCOS, based on ASIC (Application Specific Integrated Circuit) technology. These are integrated into a single versatile board developed in collaboration with the Polytechnic of Milan, housing two ASICs with 16 channels plus a FPN channel (Fixed-Pattern Noise, useful to determine the intrinsic noise level and baseline shapes in order to improve the overall resolution), for a total of 32+2 read-out channels [60, 61]. Four of these motherboards are installed one for each side plate, cooled through thermal pads, and connected to the output with a patch

panel, carrying a total of 136 channels. In the case of CHIMERA, the signal is then also sent to a Dual Gain module, designed by INFN-Catania, a multi-channel digitally programmable gain amplifier. These modules produce two copies of the input signal, with different programmable gain, allowing the digitization of the input signal on two different scales. These are generally required in order to overcome the problem of the limited dynamic range of GET electronics, originating from the coupling between the VME read-out and GET. The Dual Gain Boards are directly connected to AsAd boards (ASIC plus ADC) hosting AGET chips, the very front-end of the GET system. In the case of FARCOS, the Dual Gain modules are not needed, as the custom preamplifiers can interface directly with the AsAd boards. Each AsAd consists of 4 AGET chips, the real core of the GET electronics, an FPGA and a 4-channel ADC. The AGET can process 64 independent channels plus 4 FPN, each of them consisting of a preamplifier (with four different programmable gain values), a filter, a discriminator, and can sample the frequency from 1 to 100 MHz. Each AsAd board can therefore process up to 256 different input channels. A block of four AsAd is then read-out by a CoBo (Concentration Board), thus processing data from up to 1024 channels. CoBos are housed into a μTCA (MicroTCA) chassis, which can store up to 11 CoBos, for a maximum of 11264 different channels. Up to 2 additional MicroTCA chassis can be combined to achieve the maximum system size of 33792 different channels. CoBos can both process the data coming from the AsAd boards and send the multiplicity values to the trigger module, the MuTanT (Multiplicity Trigger and Time), to generate a master trigger decision. Moreover, the data can be sent via Ethernet at 10 Gb/s through the MicroTCA backplane to computer farms for data analysis and storage. On the other side, the external PCs can communicate via Ethernet with them to configure CoBos and in turn configure AsAd boards communicating with them. The MuTanT module, installed as well in the MicroTCA crate, handles the Global Master Clock (GMC) and is able to synchronize all CoBos belonging to the same crate at 100 MHz, managing also communications with the VME acquisition for CHIMERA.

Chapter 3

Data analysis and experimental results

Data analysis from the CLIR experiment showed promising results for ^{10}Be spectroscopy. The data analyzed using the FARCOS array allowed us to obtain an excitation spectrum for the isotope examined, in which the energy levels are in agreement with the ones theoretically predicted, and with other case studies in literature. Furthermore, it is possible to compare this spectrum with the one obtained in a previous result achieved by the CHIMERA collaboration [14] at LNS, in order to show differences and improvements in the analysis, in particular especially with the results obtained for the spectroscopy of ^{10}Be during the UNSTABLE experiment, previously discussed in Sect. 1.5.1. In this Chapter, the techniques used for the calibration of the detectors, for the identification of the fragments on the FARCOS detector will be described and the main results of the analysis will be presented.

3.1 Calibration of FARCOS stages

As previously described in Sect. 2.1, CLIR was the first experiment involving the FARCOS detectors, and therefore this study is important not only for the physics case under study, but also for a full characterization of the FARCOS performances. Telescopes were placed inside the CHIMERA chamber at a small polar angle, covering $1.6^\circ \leq \theta \leq 8.2^\circ$ polar range. As it will be underlined later on, it can be observed that, using a polyethylene CH_2 target, at the energies of the incident cocktail beam, most of the fragments are emitted at a small angle. For example, as shown in Ref. [62], the ^{10}Be break-up cross section on hydrogen recoil target is focused forward, at small angles under 5.6°,

expecting most fragments in the range covered by the detectors. The analysis for the reconstruction of the excitation energies of ^{10}Be, however, is also only possible by accurately measuring the energy of the participants in the reaction, and more particularly of its decay products. The positioning of the FARCOS telescopes at small angles, where most of the reaction products are expected, was crucial, thanks above all to the *pixelation* of the DSSSD, which improves the angular resolution and, as a consequence, the energy resolution of the collected events. As it was described previously, both FARCOS DSSSDs and scintillators, with their electronic chains and QDCs, provide an energy loss value in arbitrary units (channels), so an accurate calibration of the stages is indispensable, and represents a crucial aspect for the success of the analysis of the data. Furthermore, this experiment was actually the first to use FARCOS detectors. Since then, during subsequent experiments, the detector has evolved both in its structure and in its electronic chain, as better explained in Sect. 2.6.1 with the GET electronics and the new preamplifiers mounted on the body of the detector itself. For this reason, for the CLIR analysis it was necessary to study and devise various techniques, especially starting from calibration techniques, identification of the ions in charge and mass, and most importantly data selection algorithms. However, the advantage of the developed techniques lies in the fact that these, not depending on the electronics used, can also be used in the future after being implemented with the new electronics. In this section the various methods of calibration of the three different stages of FARCOS will be described, starting from the 1500 μm stage DSSSD, and the following CsI(Tl).

Calibration of the FARCOS DSSSD stages

The energy lost by particles in the detector is provided by the QDCs, according to the electronic chain described in Sect. 2.6. The Time of Flight ToF is the time employed by the particle to travel from the target to the FARCOS detector. Calibrations for the DSSSDs stages of the FARCOS arrays was performed with different methods for the 300 and 1500 μm stages. In this regard, it is necessary to point out that the 300 μm stage was not provided with the electronics for the back side of the detector, so only data for the front side was gathered. However, due to the high incident energies of the cocktail beam ions, the 300 μm stages were actually only secondary for the complete information on the incident energy of the fragments. In this way, the pixelisation

of the event, i.e. the assignment of a specific front and back strip for the univocal calculation of the two angles θ and ϕ, is carried out starting from the second DSSSD stage.
The 1500 μm stages of FARCOS were calibrated on both the front and back sides, for which each strip was calibrated singularly. Through the simulation software LISE++ [63], the energy loss on the tagging detector allowed us to calculate the incident energy on the CHIMERA reaction target for each ion of the cocktail beam. Therefore, a calculation of the elastic scattering of the beam components was performed, obtaining the incident energy of each isotope for every "virtual" pixel of the 1024 total for the second stage, given from the intersection of the 32×32 front and back strips. The elastic scattering was calculated on the carbon ions of the polyethylene CH_2 target, assuming the scattering in the middle of it. In this way, it was possible to calculate the energy loss on the 1500 μm stage for each component of the cocktail beam and also considering the correct angle of the assigned pixel. Moreover, since in this phase of the calibration the 300 μm stage was not yet calibrated, a simulation of the energy loss on the first DSSSD was also taken into account. Calculations of the energy loss on the 300 μm stage and on the reaction target were performed thanks to the KaliVeda framework for heavy ion collisions, developed at IN2P3 and based on ROOT [64].
Thus the calibration of this second stage of the detector was performed by comparing the values calculated with the LISE++ software as previously explained. The experimental values of the energy loss of the elastically scattered beam were obtained by ΔE-E plots produced from the data gathered by the 1500 μm stage and by the following CsI(Tl) scintillator, as shown in Fig. 3.1. To produce these distribution plots, a selection was performed collecting events for every front and back strip in coincidence, therefore producing, for each telescope, a total of 1024 ΔE-E matrices.
As it can be observed in Fig. 3.1, at the end of each ridge, a pronounced distribution is present, accurately locating on the graph the position of the energy loss of each elastic beam. To recognize the ion ridges belonging to the cocktail beam component, several cuts on the tagging system plot were applied. In this way a further selection can be provided, producing ΔE-E matrices populated only by the ion selected and by its reaction products. An example can be seen from Fig. 3.2, obtained applying on the tagging matrix a cut for the ^{10}Be distribution. As one can see, the selection allows to identify each ridge of the complete ΔE-E matrix, ending with the distribution for the energy loss

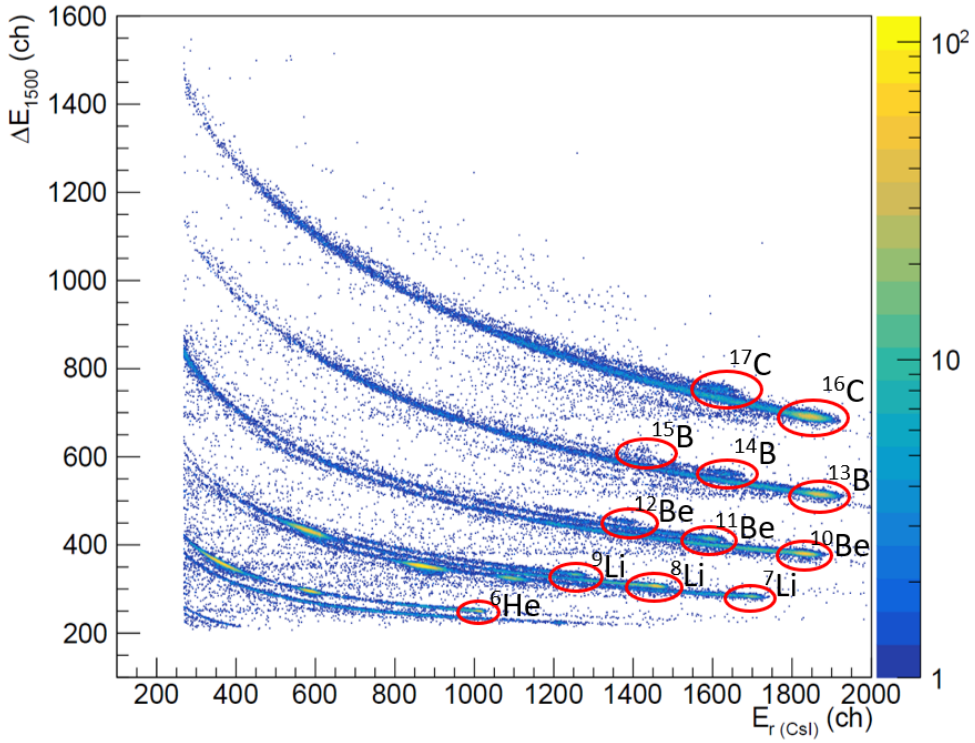

FIGURE 3.1: ΔE-E plot relative to a single strip of the 1500 μm stage of a FARCOS detector, with the following CsI(Tl) stage. In the plot, not calibrated yet, the positions of the energy loss distribution of the elastic scattering beams are shown.

of the elastic scattering beam. The selection of the cocktail beam ion on the tagging matrix by means of graphic cuts also made it possible to highlight, for example in the case of the ^{10}Be, the presence of other fragments, mainly coming from the cluster break-up, namely ^{4}He and ^{6}He.

The same process is therefore repeated until every cocktail beam ion has been recognized. Then, for each pixel of the same strip, the energy loss ΔE (in channels) of each ion is associated with the corresponding value calculated with the LISE++ software for that ion at the corresponding scattering angle, and plotted on the same calibration graph. Fig. 3.3 shows an example of calibration for a single strip of a telescope, done through a linear fit of type $\Delta E(\text{MeV}) = \text{Gain} * \Delta E(\text{Ch}) + \text{Offset (MeV)}$. Fig. 3.4 shows instead the relative error of each point plotted on Fig. 3.3 from the calibration line obtained, showing then a maximum discrepancy of less than $\approx$ 2%, underlining then the good likelihood of the fit.

This method of calibration allowed to calibrate about 50-60% of the total amount of front strips of the four FARCOS telescopes. This is due to the fact

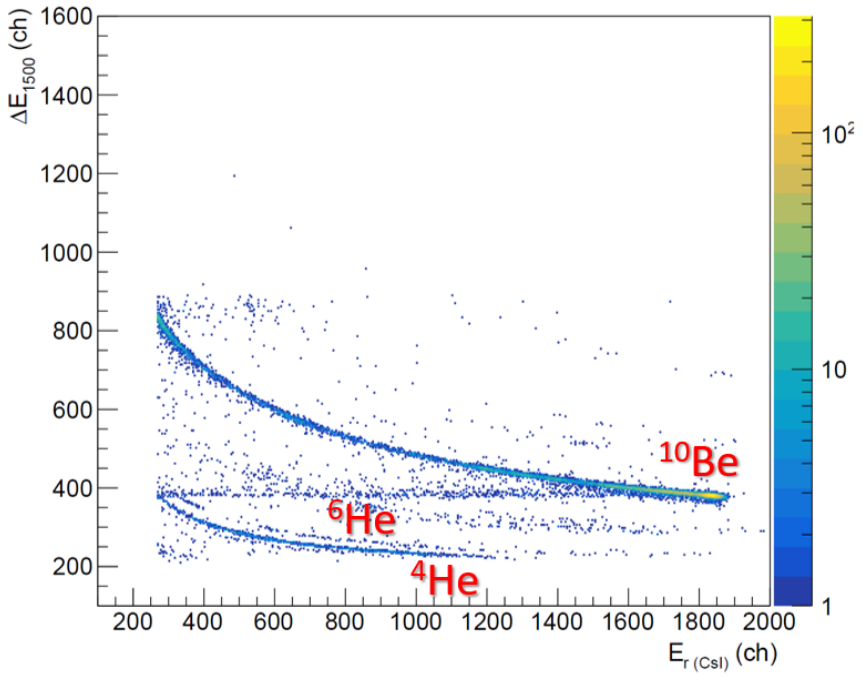

FIGURE 3.2: ΔE-E plot obtained from the previous plot of Fig. 3.1, applying a cut on the tagging matrix (Fig. 2.7) for the selection of the ^{10}Be beam. Moreover, traces of the clustering break-up products can be seen (^{6}He and ^{4}He).

that, by increasing the distance of the considered strip from the beam axis, the intensity of the elastic scattering distribution on the ΔE-E plot decreases, until it becomes so faint to be recognized with good accuracy, preventing to perform a good fit.

The back sides of the second DSSSD stage was also calibrated, however using a different method. This was performed by employing the calibration parameters obtained for the previous front side strips. The technique used in this case uses the main feature of double sided silicon strip detectors: when an ion passes through the DSSSD detector and the event does not affect different strips on the same side (i.e. no induction or interstrip events), the strips record a signal linearly proportional to the energy of the impinging ion, both on the front and on the back strips, which read the same energy value. Therefore, by selecting the events in which the particle passes from a front strip calibrated in energy for each single back strip, it is possible to obtain a linear graph that correlates the calibrations of the fronts for each back strip. As an example, Fig. 3.5 shows the calibration performed in this way for a back strip, highlighting the linear trend of the calibration between the front and back strips, that can therefore be calibrated.

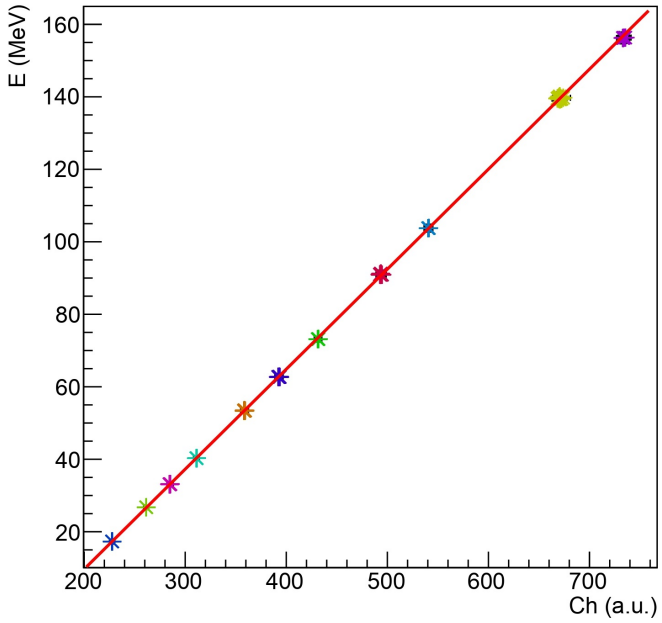

FIGURE 3.3: Calibration line of a single strip of a 1500 µm stage of a FARCOS detector.

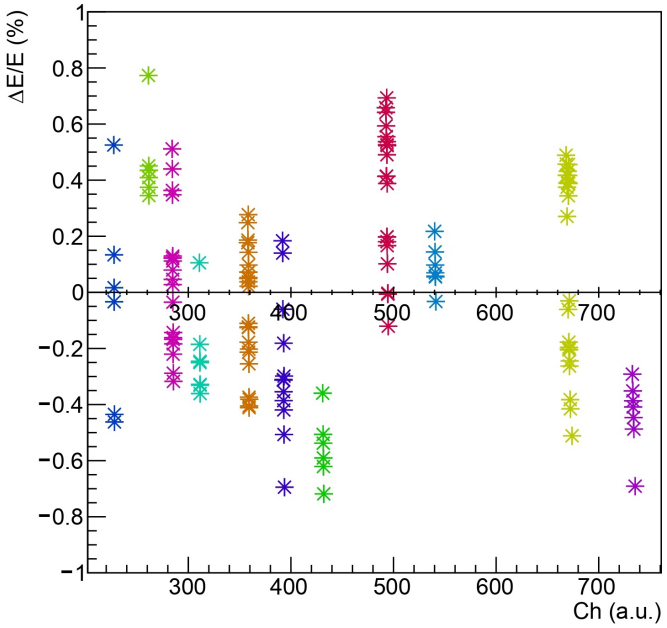

FIGURE 3.4: Relative error obtained for a calibration line of a strip of a 1500 µm stage of a FARCOS detector. Errors are referred to the points plotted on the calibration of Fig. 3.3, from the fitted calibration line.

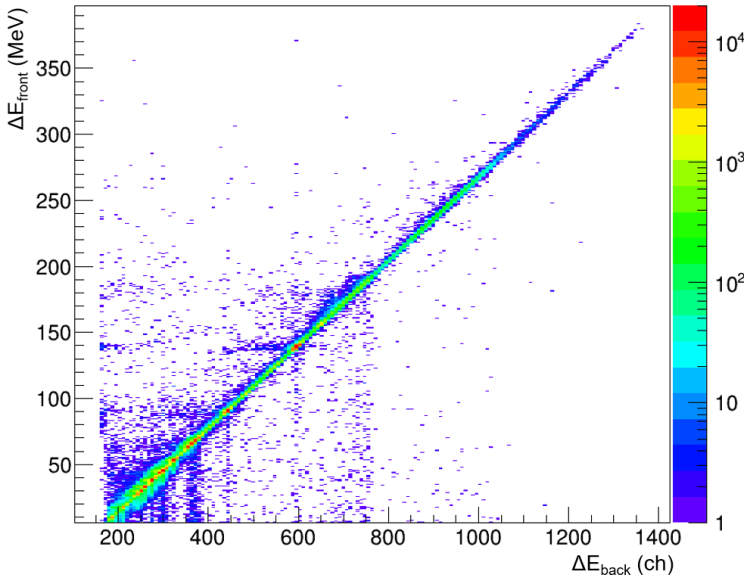

FIGURE 3.5: Calibration plot of a back strip of the 1500 µm stage of FARCOS, obtained plotting the value in channels vs the calibrated energy recorded by a one of the corresponding front strips.

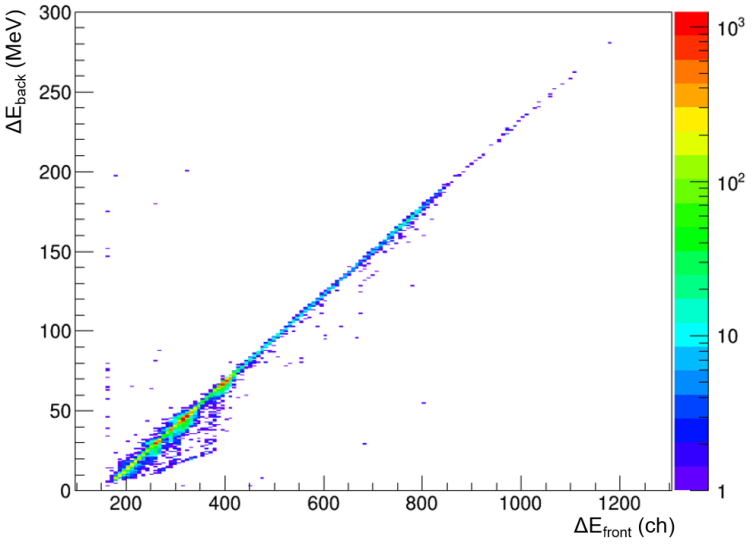

FIGURE 3.6: Calibration plot of a front strip of 1500 µm stage obtained correlating the signals gathered on the strip with the ones obtained for the calibrated back side strips of the detector.

This technique was also applied to the remaining front side strip not-yet calibrated, since, to obtain a linear trend capable of being easily fitted, many fewer calibration points are needed.
Fig. 3.6 shows an example in which one of the strips furthest from the beam

has been calibrated by the signal from the back strips. This method therefore allowed to calibrate the entirety of strips of all the FARCOS detectors, of course rejecting the ones that did not work during the data gathering, due to defects of the detector or electronics issues.

Calibration of the FARCOS CsI(Tl) detectors

CsI(Tl) scintillators have always been recognized to be a powerful material for the study of heavy ions, thanks to their relatively high performances and availability. This however is achieved at the cost of an evident difficulty in its unambiguous characterization, due to the non-linearity of the crystal response to highly ionizing charged particles. In literature in fact, since the early 90s, the non-linear behaviour of the response of CsI(Tl) scintillators to heavy ions has been known. One of the first pioneering studies about the dependence of the light output of a CsI(Tl) scintillator on the charge Z, mass A and energy E of an impinging ion comes from the work of Horn D. et al. [65]. It was in fact already known that the material suffers not only from "quenching" effects, in which the response of the detector has a reduction of the light yield with regard to the linear behaviour, but also that for a given energy, the light response depends on the type of particle. To obtain a first approximation of its behaviour, the Birks formula for the differential light output can be used, in the form of:

$$\frac{dL}{dx} = \frac{S(dE/dx)}{1 + [kB(dE/dx)]} \tag{3.1}$$

where S is the scintillation efficiency and kB the quenching factor. Using the approximation for which the energy of the incident ion is greater than a few MeV/u, so that it is possible to approximate $dE/dx \simeq cAZ^2/E$, the equation 3.1 can be analytically integrated to obtain the Horn formula for the value of the light output L [65]:

$$L = a_0 + a_1 \left\{ E - a_2 A Z^2 \ln \left| \frac{E + a_2 A Z^2}{a_2 A Z^2} \right| \right\} \tag{3.2}$$

with A, Z and E respectively the mass, charge and energy of the impinging ion, and constants relative to the considered material a_0, a baseline offset,

$a_1 = gS$, with g the gain factor of the electronics, and $a_2 = ckB$. This behaviour is non-linear and at the same incident energy, for different ions with different A and Z values, the scintillator produces different light outputs in channels, recorded by a photomultiplier and associated electronics.
Even though the Horn's model works as a first approximation to characterize the light output of incident ions in a CsI(Tl) scintillator, it fails to take into account the lattice effects of its crystal structure. In fact, the quenching effect is actually connected to electron-hole recombination effects, the impinged ion slows down and captures electrons, creating holes and leading to UV intrinsic transitions of the crystal. This effect also leads to the production of δ-rays, secondary electrons with enough energy to produce secondary ionization effects, varying the contribution of produced light. It has been in fact demonstrated by Parlog M. et al. [66, 67] that this effect is quite important in the production of the light output, especially for heavier ions. On the other side, electrons and γ rays behave linearly with their energy. In this case, the "Recombination and Nuclear Quenching Model" (RNQM) was developed and described by [66, 67], in the experimental case of the INDRA array [68].
For this model, to describe the light output of a CsI(Tl) one has to consider that:

- As in the case of the Horn formula described before, the electronic stopping power is given by the usual Bethe-Block approximation:

$$\frac{dE}{dx}_e(E) \approx \frac{cAZ^2}{E}; \tag{3.3}$$

- The passage of the particle produces defects inside the crystal, which contribute to the production of recombination effects, with light output different from the typical 550 nm yellow light. In a first approximation such concentration is given by $N_n(E) \propto AZ^2/E$;
- The nuclear stopping power can be approximated by

$$\frac{dE}{dx}_n(E) \approx \frac{a_2 AZ^2}{E} \tag{3.4}$$

  with a_2 a constant obtained by many contributions that can be regarded as constant in the used approximation.

- the fractional energy carried by the δ-rays, or knock-on electrons, in the

non-relativistic approximation outside a column of radius $r_c \approx 260$ nm. In the approximation used this value is considered as a step function with value 0 if $E/a \leq a_3$ and a_4 if $E/A > a_3$, with a_3 the energy per nucleon threshold for the δ-ray production and a_4 a fit parameter.

By using these approximations, the light output can be analytically found as [67]:

$$L = a_0 + a_1 \left\{ E - a_2 A Z^2 \ln \left| \frac{E + a_2 A Z^2}{a_2 A Z^2} \right| + a_4 a_2 A Z^2 \ln \left| \frac{E + a_2 A Z^2}{a_3 A + a_2 A Z^2} \right| \right\} \tag{3.5}$$

Formally, Eq. 3.5 contains 5 fit parameters, where the first three are consistent with the ones provided by Horn, in the previous Eq. 3.2. The new multiplicative term instead takes into account the effects of electron-hole recombination and the production of light due to δ-rays. In fact, the parameters a_3 and a_4 are related to δ-ray production, and respectively represent the average energy E_δ and the fractional energy loss transferred to a δ-ray, both fit parameters for a friendly analytical expression of L.

Calibrations for the CsI(Tl) detectors of the third stages of FARCOS were performed with both approaches described previously. The experimental values of the light output of the CsI(Tl) were obtained by the fast signal of the detector (in channels), while the energy (MeV) value of the stopped ion was obtained through the calibration of the 1500 μm stage. A ΔE-E plot for each CsI(Tl) scintillator was produced, using the calibrated ΔE data for the front strips previously obtained, and selecting events with only 1 hit on both the DSSSD and CsI detectors. Then, by identifying the ions, several points on the ΔE-E plot ridges were collected for each ion, and by using the energy loss on the 1500 μm stage, the residual energy was evaluated.

Fig. 3.7 shows a fit performed by using Eq. 3.2, while Fig. 3.8 shows one obtained with the RNQM model. The errors on the plotted points are obtained from $\pm 1\%$ relative error of the light output values obtained experimentally, while those on the residual energy E are obtained from the calculation of the energy loss from the uncertainty on the points on the graph ΔE-E. Between both methods, the one that shows a better likelihood with respect to the experimental data seems to be the RNQM, which was then used forward in the analysis.

Moreover, as one can see, the function 3.5 however is an expression of A,Z and incident energy E of the ion, allowing to retrieve the light output L.

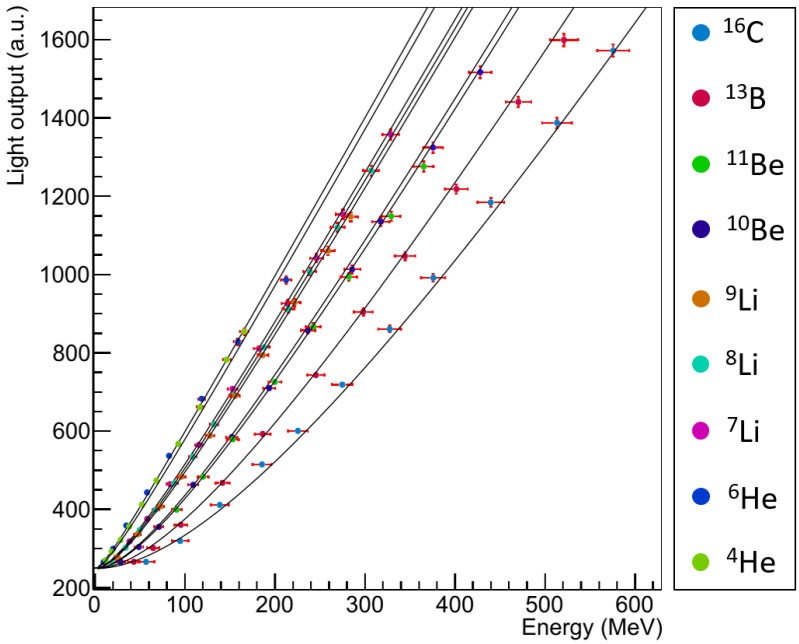

FIGURE 3.7: Calibration of a CsI(Tl) of the FARCOS detector, using the Horn model described by Eq. 3.2.

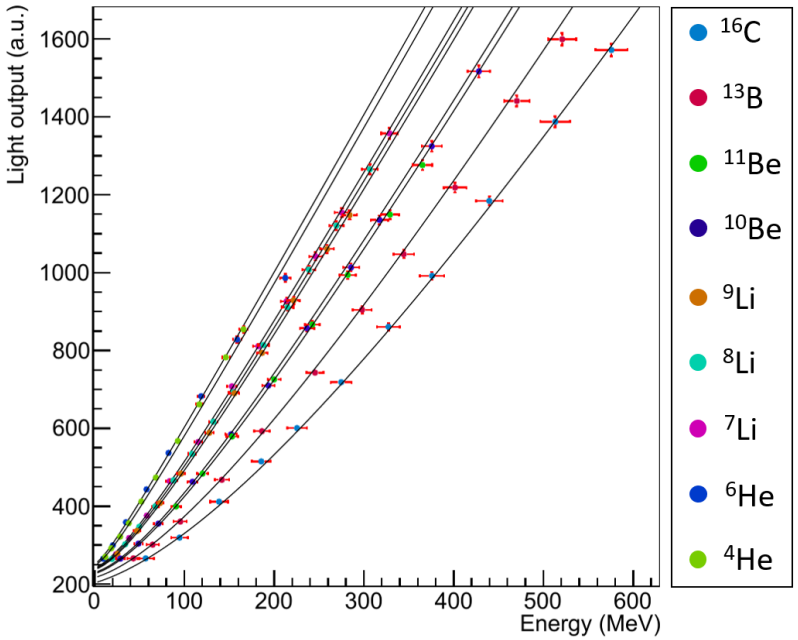

FIGURE 3.8: Calibration of a CsI(Tl) of the FARCOS detector, using the RNQM formula described in Eq. 3.5.

Therefore, to get the residual energy E_r from experimental value, this has to be inverted. To this aim an inversion algorithm, based on the bisection method, was implemented, allowing to convert the experimental data in

channels to MeV.

3.2 Identifications through ΔE-E method

The identifications in charge and mass of the ions detected by FARCOS are based on the technique previously described for CHIMERA in Sect. 2.4.1. This is based on the parametrization of Le Niendre et al. [52] of Eq. 2.4. Some modifications, however, with respect to the method developed for CHIMERA, have been made, to make it usable also for FARCOS and radioactive beams. In the case of FARCOS, the technique is applied on the ΔE-E plots between the second 1500 μm stage and the CsI(Tl), although theoretically it could be applied even for ΔE_{300}-ΔE_{1500}. It is important to underline that the method applied is absolutely empirical and it does not depend on the calibration of the two stages, thus the technique is also applicable using non-calibrated data. To do this, dispersion plots are produced for each front strip of the DSSSD, and for each coincident scintillator. Given that each front strip corresponds to two CsI(Tl), 64 different matrices are produced for each FARCOS telescope. The ion identification procedure starts first of all with the attribution of its charge. In fact, through graphical recognition, the first charge and mass values are assigned, allowing to fit various curves for Eq. 2.4 for each isotope. After fit parameters are returned, the charge of the ions can be initially verified from a charge distribution plot, as the one shown in Fig. 3.9. After the charge has been correctly attributed, the mass is therefore found by using the same fit parameters previously obtained, attributing to the particle a *float* value of the mass. This mass identification procedure starts with a first guess value based on different methods, depending on the specific case of the primary beam and the population of ΔE-E matrices, and following the same optimization algorithm. While for low charge ($Z \leq 4$) the mass is given by constant values, for $Z > 4$ the first guess is based on the formulas:

- mass is simply defined as $A = 2Z$;
- the Charity formula, given charge $Z > 4$, the mass is returned by the Charity formula [69]:

$$A = (2.072\ Z + 2.32\ Z^2 \times 10^{-3}) + 1; \tag{3.6}$$

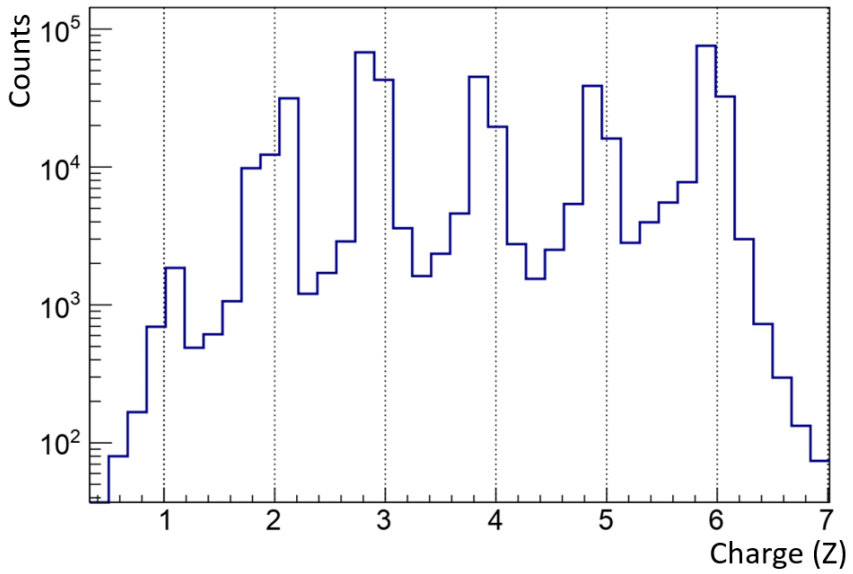

FIGURE 3.9: Typical charge distribution obtained from the identification algorithm of a ΔE-E matrix.

- Mass is calculated following the EPAX2 systematic. EPAX is an empirical parametrization based on the fragmentation cross section, so that given a projectile and a target the algorithm finds the possible quantities for the masses produced, based on cross section calculations [70].

Although these methods have been successfully used in the past for CHIMERA with the use of stable beams, with neutron-rich radioactive beams, because of the neutron enrichment, they are not able to reproduce the mass correctly, and therefore cannot be used. Many tests were therefore carried out so it was decided to use the simple empirical formula $A = 2.67\ Z$, because in the fitting procedure it almost precisely reproduces the expected mass of the elastic isotopes (16 for the carbon, 10 for beryllium). Using this simple yet effective formula, a *float* value of the mass is then fitted allowing to obtain for a given ΔE-E matrix a distribution plot as the one shown in Fig. 3.10.
The method thus applied therefore provides identification parameters based on the Eq. 2.4 formula. It is therefore possible to apply the same procedure event-by-event, allowing to obtain the correct charge and mass values independently of the detector and data calibration.

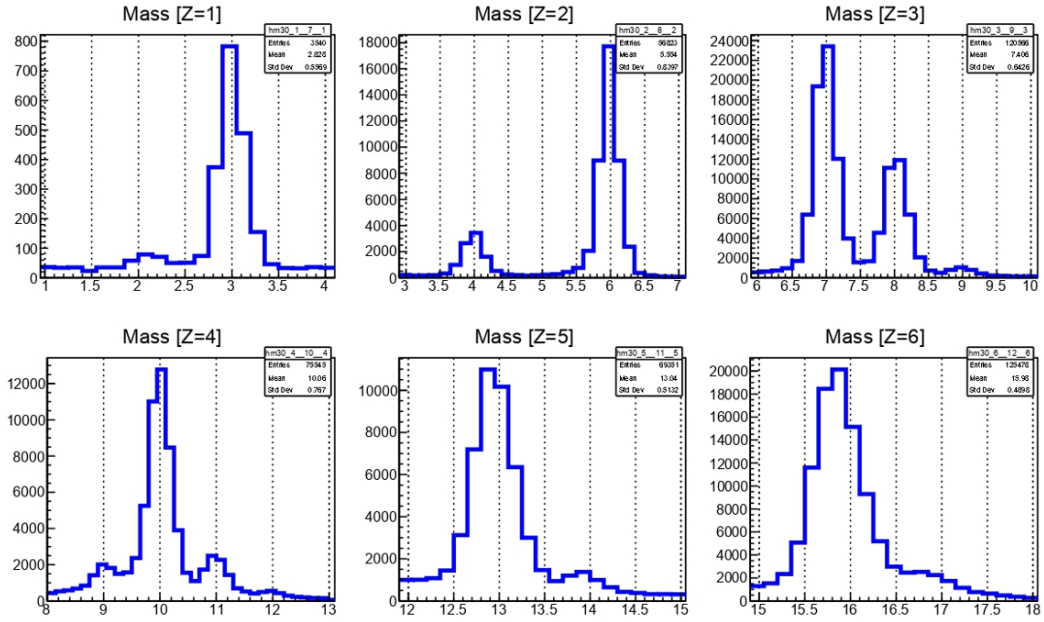

FIGURE 3.10: Mass identification plot obtained for the main charges of the ions detected by FARCOS in ΔE-E matrices. We note how the main fragments, for $Z = 2$, $Z = 3$ and $Z = 4$ are correctly identified.

3.2.1 Simulations and calibrations for the 300 μm stages of FARCOS

The calibration of the 300 μm stage of FARCOS proved to be a more complex task than expected. The first attempt was obtained by trying to calibrate its front strips (the only ones used for the CLIR experiment, since the electronics for the backs were not provided) using the method previously explained for the FARCOS 1500 μm: linearly fitting the values of energy loss of the elastically scattered beams with the experimental points obtained from plots ΔE_{300}-ΔE_{1500}. This, however, was not possible because, unlike the 1500 μm, at the energies of the different ions in the beam of around 40-50 MeV/u, the energy losses on the first stage are very similar to each other, preventing correct calibration through this method (Fig. 3.11)[1]. Another possible technique for strip calibration resulted in the application of the *punching-through* technique. Since the 300 and 1500 μm stages are still quite thin, it is normally likely that some particles may stop and remain trapped inside the second

[1]This behaviour can be observed for example from Fig. 3.11, which, for the sake of clarity, was calibrated in MeV, on the vertical axis through simulation, as it is going to be described.

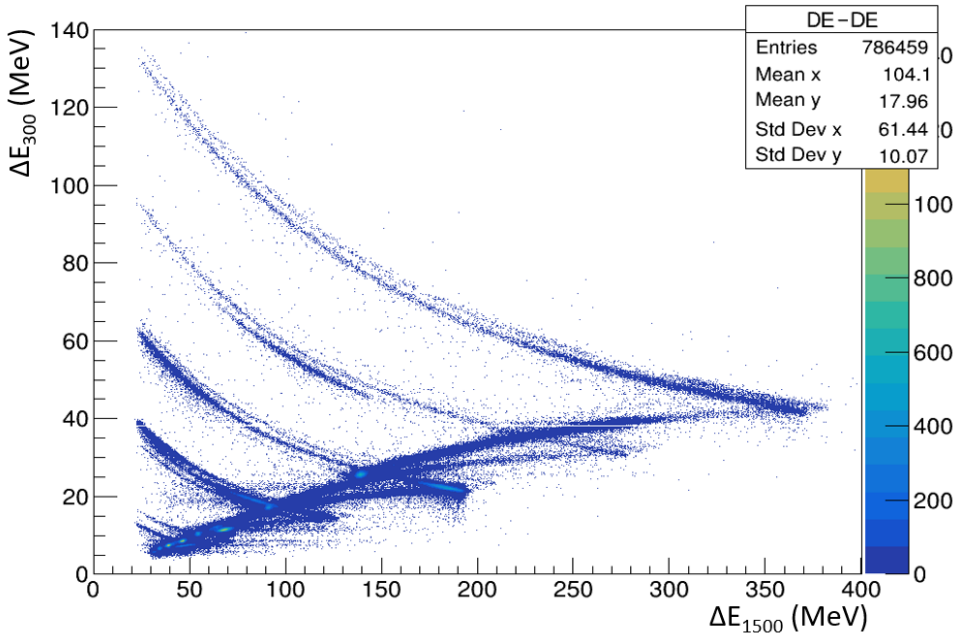

FIGURE 3.11: Calibrated ΔE_{300}-ΔE_{1500} matrix obtained by plotting calibrated data from front side strips of the 300 μm and 1500 μm stages. Several ridges for several isotopes can be observed. The reversal of concavity with the punching through position can be approximately observed.

stage, while others, more energetic, manage to pass through it, finally arriving on the CsI(Tl) scintillators.

It is possible to observe these two trends starting from a ΔE_{300}-ΔE_{1500} distribution plot as in Fig. 3.11: the particles stopped inside the second DSSSD produce higher energy loss signals, originating a positive concavity distribution; on the contrary, the more energetic ions release less energy in the 300 μm thick detector, producing a negative concavity distribution. For the same ion, two ridges are therefore formed, joining in a cusp singularity so-called "punching-through", whose energy can be easily calculated by considering a thickness of 300 μm of silicon and an ion with mass A and charge Z and applying the Bethe energy loss formula [71]. By obtaining these values for various ions it is theoretically possible to produce a linear fit and calibrate these strips for 300 μm. However, this method could not be efficaciously applied for this case, as most of the fragments produced were in transmission and due to a low quantity of ions stopped within the 1500 μm, making the retrieving of the position of the punching-through position uncertain.

For this reason, a new method was created, based on the simulation of energy

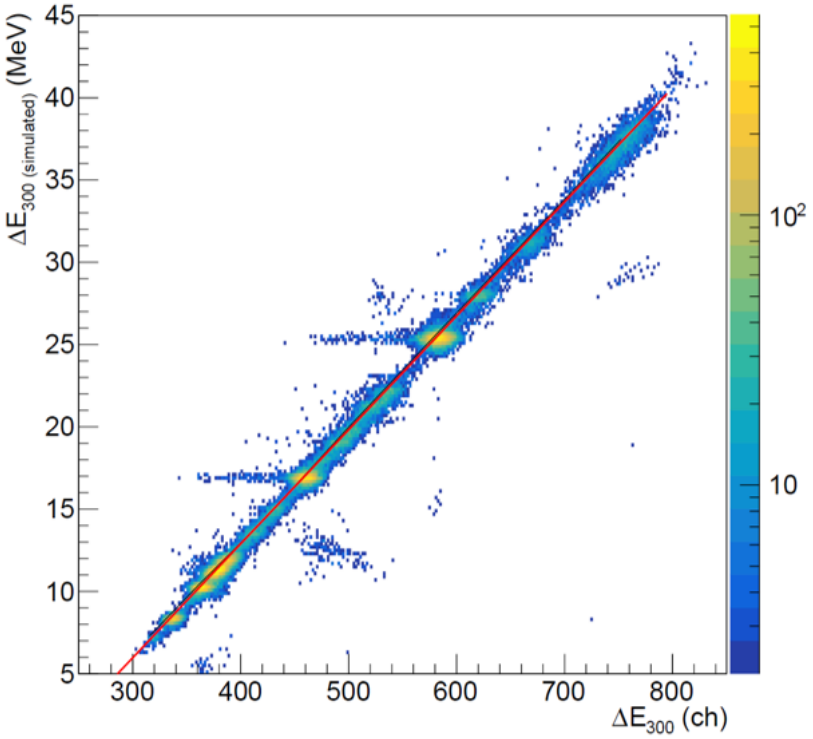

FIGURE 3.12: Calibration plot obtained for a 300 μm front strip, through calculation of the energy loss on the stage from the total outgoing energy of the identified ion.

loss in the material. The signal produced by silicon detectors, such as those of FARCOS as previously stated, behaves in a linear way with the energy of the incident ion. Since the CHIMERA chamber is under vacuum, an ion, after reacting with the target, loses negligible energy in it, while subsequently reaching the FARCOS stages. Here ideally an ion loses energy successively in the 300 μm, 1500 μm and CsI(Tl), where it stops.

The procedure begins by selecting events in which energy was released successfully in all three stages of FARCOS, and in which the energy of 1500 was calibrated and the ion was correctly identified via the ΔE-E matrix. Through the energy values obtained, it is possible to calculate the incident energy on the 1500 μm stage. This is actually the energy of the ion coming out of the 300 μm after losing energy in it. Through energy loss software, it is therefore possible to calculate the energy loss on the 300 μm stage. A dispersion plot is then created event-by-event, in which the energy loss (in channels) is correlated to the energy loss obtained through calculations. Fig. 3.12 shows an example of a single strip, from which it was possible to obtain the linear

parameters for the calibration.

3.3 Data clean-up and event selection

An important part of the FARCOS data analysis for the CLIR experiment involved the implementation of data selection algorithms. One of the main purposes of the FARCOS DSSSDs is in fact to associate, for each event, the correct front strip with the back one, giving the possibility of assigning a unique pair of polar and azimuthal angles θ and ϕ. However, the very presence of different strips may cause various issues that need to be overcome. Given a single FARCOS telescope, it is possible that the same DSSSD, on either its front or back sides, could record an event with multiplicity $M > 1$, characterized by the hitting of two or more different strips during the same time window. This case is not uncommon *per se*, since the telescopes are positioned in the forward direction, where the reaction is more kinematically focused, and it is possible that they record decay products from the same reaction, arriving at a small angle and on the same detector. This could prove to be a serious issue, as at this point the front-back assignment process of an event with multiplicity $M \geq 2$ for the single telescope is no longer a trivial task.

First of all, the data is filtered with a cut on the Time of Flight of the FARCOS strips. Although the ToF has not been calibrated, from its spectrum it is still possible to observe a population of a region indicating *coherent* events. Therefore a large window of about 500 channels (equivalent to about 120 ns, given a standard 250 ps value for channel) is selected, allowing to obtain a safe selection of all correct events and rejecting non-correlated events or events for which the start of the ToF has not been recorded. Only after this first selection, a procedure to assign the correct front to back strip is carried out, for each telescope taken individually. In this case, a complex assignment algorithm has been designed, based on the energy loss of the ion on the single strip. Before describing the algorithm it is necessary to underline that the value of the energy loss by the incident ion inside a DSSSD is the same in both the front and back strip it goes through, within a certain error which can vary depending on the strips and the their resolution.

For the sake of the explanation, let us consider a single FARCOS DSSSD, in which two strips are hit on both the front and back sides. It is also assumed

that the two strips fired for the same sides are not adjacent or consecutive, since this case will be later treated in detail. The calibrated energy of the fronts will then be written as ΔE_i^f, with i the index of the front strip, while for the backs it will be ΔE_j^b, with j the index of the back strip. A matrix is then created whose terms are calculated as the differences between the energy loss on front and backs squared to the power of two:

$$M_{ij} = (\Delta E_i^f - \Delta E_j^b)^2 \tag{3.7}$$

Therefore, in this precise case in which there are only two strips hit on the front and back sides, a 2×2 matrix is created. After that, all the sums of the terms of the matrix, considering only one repetition of the indices i and j, are calculated and stored. Since the energy loss on a front strip must be the same as the one on the back (or in a real case very close to each other, assuming a small difference, due to the finite energy resolution of the strips) the terms of the matrix M_{ij} would therefore be smaller only in the case of the correct front-back association. At this point, the choice is made unique by adding the different matrix elements M_{ij}, without pedix repetition, and choosing the combination of differences (i.e. front-back strip indices) that minimize the sum. The result of the algorithm is therefore a single combination of associations between front and back strips, for which, based on the energy loss on them, the ion should have passed, completing the pixellation process.
This however is as simple a case as possible, but the algorithm has also been extended to more complex cases. It is possible that the number of strips hit is not the same between the two sides of the detector, i.e. the multiplicity of one side is different from the one of the other. In these cases, the origin of the issue could be due to different factors. If a signal originated from a strip not adjacent to the others, it is possible that, during the opening of the QDCs gate, a random low energy noise event, but still energetic enough to exceed the set threshold level, was also recorded. Such events are typical for example of the most external strips, which, due to the non-uniformity of the field at the edge of the DSSSD detector, can be subject to electromagnetic noise.
If, however, the strips fired on one side of the detector are adjacent, it is possible that an *interstrip* event or an electromagnetic induction has happened. In the case of an interstrip, the incident ion impacted the detector close between

two adjacent strips, causing a signal on both strips, whose sum is theoretically equal to the total energy lost by the ion inside the detector. In this case, it is still possible to apply the method described previously, creating an event given by the sum of the energies of the two adjacent strips, and having a fictitious strip index. The case of inductions, however, is more complex and delicate, as it is originated by the electronic cloud of the ion, creating a delayed electronic signal in a side strip. These events can be reconstructed simply by applying the previous algorithm, but including also a cut on the time difference between the two adjacent events, which should not exceed 20-30 ns.

3.4 Preliminary results on ^{10}Be excitation spectrum

In this section some results of the analysis of ^{10}Be will be described. The work is still preliminary since, as will be underlined, optimization work will still be needed. In the case of ^{10}Be, the excitation energy spectrum for the ^{4}He + ^{6}He cluster break-up channel was reconstructed, using correlation techniques between the two resulting fragments detected by the FARCOS array. First, a selection of the ^{10}Be beam was carried out on the tagging matrix, through a graphic cut, selecting *a priori* only the events originating from this isotope. This can be convenient since it allows us to obtain usable data, attributable only to the fragmentation of the isotope considered, correctly selecting the reaction channel. Subsequently, the events of multiplicity $M = 2$ were selected, in which the identification recognized a ^{4}He and ^{6}He pair. Therefore, through the invariant mass method, the excitation energy of the ion was obtained, by adding to the relative energy of the two clusters emitted from the considered channel, the energy threshold for the decay channel under study $-Q_{gg} = 7.409$ MeV. Fig. 3.13 shows the spectrum obtained: although the statistics are low, it is possible to observe the presence of some structures in agreement with data found in literature [6, 17, 23]. The presence of some particularly interesting peaks is shown: the peaks at 9.5 MeV and 11.8 are fairly clear, while the 7.5 (2^+) MeV, 10.15 (4^+) MeV and 13.5 (6^+) MeV, belonging to the ^{10}Be molecular rotational band [21, 23], also seem to be present. In particular, the peak at 13.5 MeV could represent a further confirmation of the peak previously identified by Dell'Aquila et al. at LNS [21].
The next step will mainly concern the validation of the data obtained, in

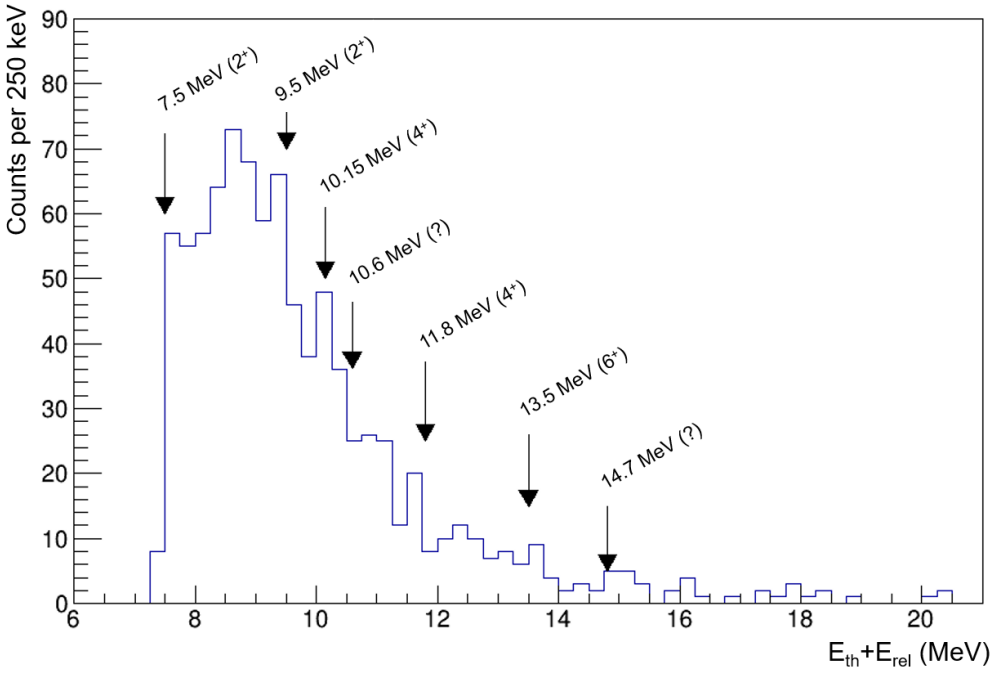

FIGURE 3.13: ^{10}Be excitation spectrum obtained through the invariant mass technique, reconstructed for the ^{4}He + ^{6}He decay channel. Positions of various peaks known in literature are marked. In the brackets the J^{π} spin parity is shown.

particular evaluating the background of the excitation spectrum and the detection efficiency of the FARCOS array. The background will be evaluated considering the contribution due to pairs of uncorrelated ^{4}He and ^{6}He fragments, through a procedure commonly referred to as *event-mixing*. This is obtained by selecting pairs of particles from different events induced by all the isotopes of the radioactive beam, and therefore not just ^{10}Be. It is also important to underline that, in general, the reaction mechanisms of ^{10}Be that lead to the decay channel studied, can be different if the projectile reacts with hydrogen or carbon atoms of the target. For this reason, it is interesting to study the detection efficiencies of the FARCOS array. These will be calculated through Monte Carlo simulations, depending on the target nucleus hit, of the detector with particular attention to its angular coverage. For the two cases, we expect two different efficiency curves, since the limiting angle for ^{10}Be at excitation energies $E_x = 10$ MeV is around 5.2°, while in the case of the carbon target, there is no limiting angle. Moreover, the angular distribution of the emitted ^{10}Be projectile can be calculated, as it can be also seen in

literature, using the formula:

$$\frac{d\sigma}{d\Omega_{cm}} \propto e^{-\frac{\theta_{cm}}{\lambda}}; \tag{3.8}$$

with λ the fall of factor of the order of 12-16 degrees [62], concluding that the emission of break-up fragments is forward focused. This therefore suggests that the angular coverage of the FARCOS telescopes analyzed leads to a better detection efficiency in the case of hydrogen targets, rather than carbon, right around the beam axis.

Conclusions

This thesis discusses the results obtained for the analysis carried out on the CLIR experiment conducted at the LNS of INFN in Catania, with the aim of studying cluster phenomena in light neutron-rich ions by means of the new FARCOS detector.
The CLIR experiment involved the production of a radioactive beam by the FRIBs@LNS facility, using the In-Flight technique. A primary ^{18}O beam, accelerated to 55 MeV/u by the Superconducting Cyclotron, was then fragmented onto a 1500 μm thick ^{9}Be target, producing a cocktail beam containing several ions of interest. Among the radioactive species produced in the cocktail beam there were ^{10}Be, ^{13}B and ^{16}C isotopic species, of significant interest due to the presence of possible cluster states. In particular, among these, promising results were obtained on ^{10}Be spectroscopy, also in agreement with what had already been found in previous experiments at the LNS. The radioactive beam was identified by means of the ΔE-ToF technique, using two detectors placed on the beam line, before arriving at the experimental hall: an MCP detector, recording the start of the ToF and a DSSSD 156 μm thick, gathering the stop of the ToF and the energy loss ΔE. The experiment was conducted using four detectors of the FARCOS array coupled to the CHIMERA 4π multidetector. Particular importance was covered by the FARCOS detectors: in order to increase the angular resolution in the region of interest, the telescopes were positioned between the rings and the CHIMERA sphere, at a small angle around the beam axis, between 1.6° and 8.2° polar angles, where the majority of reaction fragments was emitted. Since it was during this experiment that FARCOS was used for the first time for a real work, coupled to the CHIMERA detector, it was necessary to develop different techniques for processing the experimental data, also due to the presence of a preliminary and subsequently improved electronics. The analysis carried out on FARCOS involved the calibration of its three different stages, for each of which it was carried out using different methods. In particular, the

DSSSDs of the second stage of 1500 μm were calibrated by correlating the energy loss of the fragments of the cocktail beam undergoing elastic scattering with the reaction target, with the value obtained through simulation. Furthermore, for the CsI(Tl) scintillators a multi-fit calibration was carried out to obtain the residual energy of the ions, following Horn's empirical formula and the RNQM method, discussed in Chapter 3. Ion identification was performed via the ΔE-E method, using data collected from the 1500 μm and the corresponding CsI(Tl) scintillator. The identification obtained is excellent, especially for light fragments clearly recognized by ΔE-E matrices, which are the ions of major interest for the study of fragmentation reactions of cluster states.

The excitation spectrum of ^{10}Be was therefore studied for the decay channel ^{4}He + ^{6}He, reconstructed using the invariant mass method. After having selected, through graphic cuts on ΔE-ToF matrices, exclusively the ^{10}Be beam from the cocktail beam, the ^{4}He + ^{6}He event pairs incidents on FARCOS detectors were selected. Starting from the energy loss on the different stages of FARCOS and from the position of the particle on the telescope, the incident energy and the emission angle of the two ions were then reconstructed. Therefore, through the method previously mentioned in Sect. 1.4, the relative energy of the two fragments in the center of mass reference was then calculated. In this way, by adding the threshold energy for the formation of the cluster state, ($-Q_{value} = 7.408$ MeV) an excitation spectrum was obtained for this decay channel. There, it was possible to observe the presence of various peaks, compatible with the energies of ^{10}Be excitation levels obtainable in literature and predicted theoretically. Some of these, compared to previous LNS measurements, show a direct improvement, especially in angular resolution. Also some peaks are shown for states belonging to the molecular rotational band exhibiting a α-2n-α configuration, at 7.5 (2^+) MeV, 10.15 (4^+) MeV and 13.5 (6^+) MeV. The last one in particular would be a further confirmation of a state observed for the first time at the LNS by the CHIMERA Group, for which a value of $J^\pi = 6^+$ was also obtained. The analysis, still in progress, will continue mainly to improve and optimize the results obtained. First of all, it will be necessary to increase the statistics of the analysis, mainly through the inclusion of the CHIMERA multidetector, which in this experiment worked mainly in the detection of the scattered target and of light fragments emitted at a larger angle. Following further cleaning of the experimental data, it will also be necessary to evaluate the background for

the obtained ^{10}Be excitation spectrum, which can be derived through event-mixing procedures. Furthermore, to guarantee the validity of the analysis, a simulation of the detection efficiency of the four FARCOS telescopes will be produced, for both the possible reaction target ions, hydrogen and carbon. The same selection procedure could therefore also be applied to other case studies, such as the break-up channels of ^{16}C (for example ^{4}He + ^{12}Be or ^{6}He + ^{10}Be) or ^{13}B, of which some states with exotic cluster cores are expected (^{4}He + ^{9}Li or the much more discussed ^{6}He + ^{7}Li). Furthermore, the techniques developed for the analysis of the CLIR experimental data will be exploited in the future for new experiments with the FARCOS detector, now employing a new digitized electronic chain as illustrated in Sect. 2.6.1.
In particular, regarding new possible works on cluster phenomena in light neutron-rich ions, in the forthcoming years, it will be possible to conduct a great variety of experiments thanks to the completion of the new FRAISE facility. The POTLNS project is about to be completed, mainly consisting of an upgrade of the Superconducting Cyclotron, which will be able to produce stable beams up to 100 times more intense, and the construction of the new FRAISE fragment separator. In this way, as described in the Appendix A, it will not only be possible to produce radioactive beams of specific, high-purity ions, but also, thanks to the higher intensity of the primary beams, to produce more unstable and shorter-lived ions, towards the neutron- and proton-drip line, which may present many exotic and poorly studied clustering phenomena. Furthermore, within the CHIMERA group, in the next months the construction of the new NARCOS neutron detector will be completed, which, used together with the FARCOS and CHIMERA detectors, will be able to provide valuable information on decay channels involving the emission of neutrons.

Appendix A

The new fragment separator FRAISE

In the last years, the Scientific Community of Laboratori Nazionali del Sud has been involved in the POTLNS, an important upgrade project for the accelerating systems of LNS and for the other infrastructures of the laboratories. The project aims in the first place at the upgrade of the facility for the production of radioactive beams with higher intensity and purity, thanks to an upgrade of the Superconducting Cyclotron and to the construction of the new fragment separator *FRAISE* (**FRA**gment **I**n-flight **SE**parator). As for the CS, the upgrade will provide a new extraction system based on the *stripping* method which, through a change of the charge (and hence rigidity) of the accelerated ions, will allow us to obtain RIBs with higher intensity. The new stripping method will be especially efficient for ions up to mass $A \approx 40$, within the Fermi energy range, for which it will be possible to increase the power from the previous 100 W to 10 kW, and for an intensity of the output beam up to 10^{10}-10^{13} pps. The high intensity beams provided by the upgraded CS will be exploited by the new fragment separator FRAISE, foreseen by the POTLNS project. The need for a new fragment separator comes first from the impossibility of installing a shielding infrastructure in the location of the FRIBs apparatus, required due to high neutron and gamma emissions, especially in the proximity of the fragmentation target and of the first dipole. For this reason, the best solution to improve the production of radioactive beams was to decide on the construction of a new spectrometer with a dedicated area hosting it. FRAISE will in fact be hosted by the new area corresponding to the old LS-20 and LS-40 halls, appropriately shielded on floor, walls, roof, and other critical points. From simulations of neutron

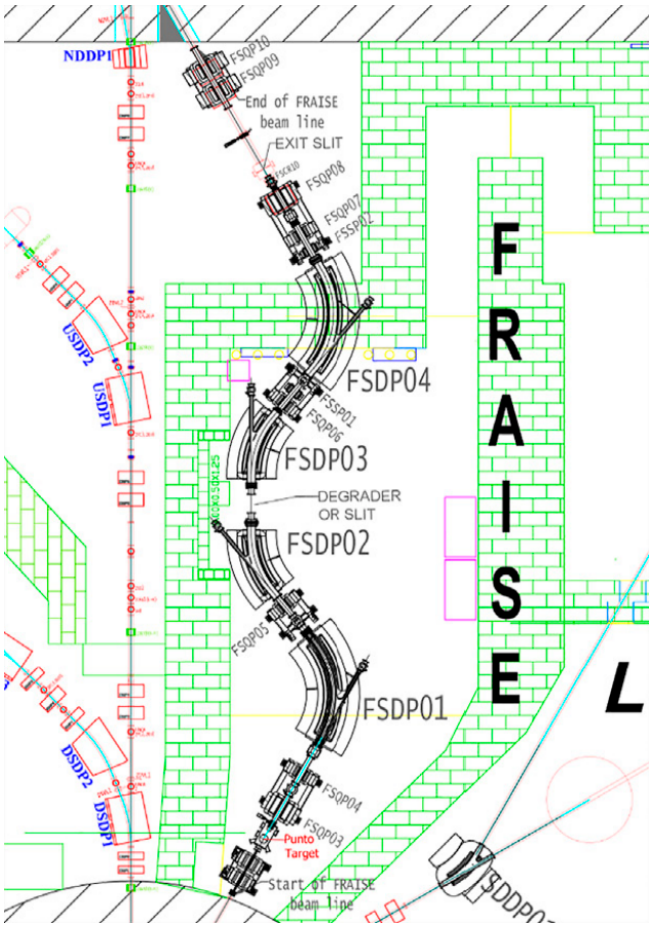

FIGURE A.1: Schematic view of the new FRAISE fragment separator. The different components can be observed, i.e. fragmentation target, dipoles, quadrupoles and sextupoles, as well as the position of slits and degraders. Figure adapted from [43, 33].

and gamma ray production on the LNS infrastructures it was found that the location will be able to sustain spurious radiation from primary beams of maximum power of 2-3 kW. With this available power, FRAISE will be able to produce RIBs with high intensity of the order of 10^3-10^7 pps, respectively for nuclei far from the stability valley and closer ones, resulting in an increase of 20 times with respect to the ones produced by the FRIBs facility. Such improvement in intensity will allow to extend the research possibilities at the LNS, allowing the study of reactions between heavy ions also for extreme radioactive ionic species, which will briefly be discussed in Appendix A.0.1.

The new FRAISE spectrometer is schematized in Fig. A.1. It will be made of two symmetrical branches to ensure achromaticity conditions as discussed

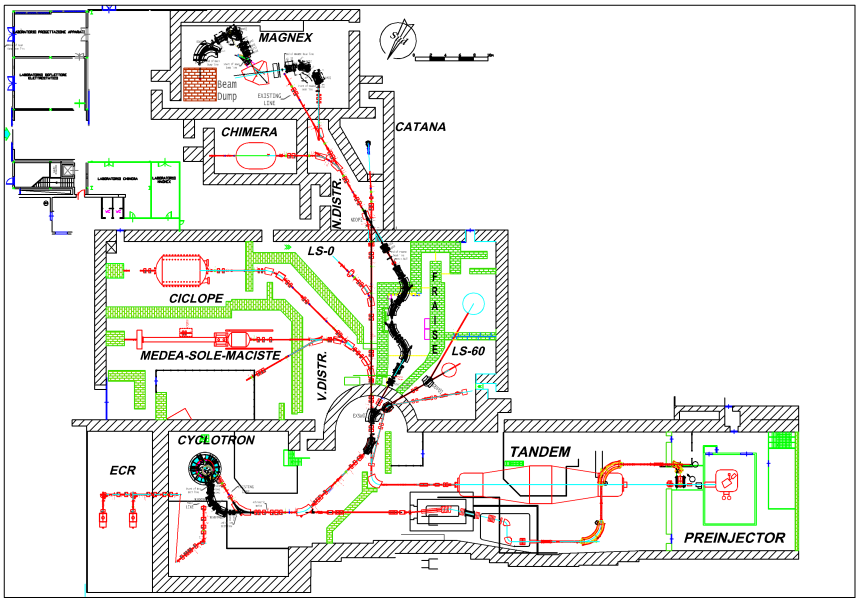

FIGURE A.2: Schematic view of the INFN-LNS infrastructures after the upgrading project, including the new beam line hosting the new FRAISE fragment separator. Figure taken from [43, 33].

in Sect. 2.2.1, for a total of 4 dipoles (two couple of 70° and 40° deflection angles), designed to reach a maximum $B\rho$ of $\approx 3.2Tm$ and $\Delta p/p \approx 1.2\%$ momentum acceptance, 6 quadrupoles and 2 sextupoles. The fragmentation target will be a CLIM target, produced in collaboration with the GANIL laboratory in France [72], housed in a dedicated chamber at the entrance of the spectrometer. It will consist of discs of beryllium or carbon, rotating and water-cooled, to spread the region heated by the beam spot and reduce the effects of degradation or overheating, due to the high intensity of the primary beam. Moreover, many thicknesses will be available for the target, and, since it will be rather activated due to the fragmentation of ions, it will not be possible to remove it manually, thus a remotely maneuverable robotic system will be able to change targets and store them in the appropriate container.
Moreover, two chambers will be installed on the beamline, respectively at the centre and exit of the fragment separator. These will host slits and detectors for the diagnosis of the beam features. The first chamber will be mounted on the symmetry plane, between the two branches of the spectrometer, that is the point with higher horizontal dispersion of the beam. Here a horizontal slit will be mounted to reduce the $\Delta p/p$ momentum acceptance of the

fragment separator and thus reduce the energy spread of the outgoing beam. Moreover, an aluminum wedge can be inserted inside the beamline to perform a better cleaning of the cocktail beam and remove spurious contaminants, to increase the composition quality of the final beam, at the cost, however, of worsening its energy resolution. Moreover, the horizontal slit will grant also the possibility to produce RIBs and even stable beams with very high energy resolution, essential for the NUMEN experiment [73].
A critical aspect that the Laboratories will have to face will be the diagnosis and tagging of the beam. Due to the high rate of the RIBs and intensity of spurious radiation, it will not be possible to employ the same detectors for the tagging system developed for the FRIBs facility, discussed in Sec. 2.3, since they would be damaged within a very short time. For this reason, a new diagnostics and tagging system is under development at LNS, which should be capable of working in high radioactively activated environments and sustaining high direct irradiation, all while running for several experiments per year. The choice for the material falls onto the Silicon Carbide (SiC), which due to its high displacement and lattice binding energies make it a radiation-hard material, suitable for the making of robust detectors, confirmed also by simulations and preliminary tests conducted on thin samples [74]. Moreover, the diagnostic system is required to be versatile, to be used both for beam monitoring and tagging of the RIBs cocktail beam components, while also serving the purpose of active degrader, providing information such as intensity, energy loss, and isotope identification by means of the $\Delta E - ToF$ technique. The new detection system will be made of detectors, placed inside the two chambers in the middle and at the end of the fragment separator. Each detector will consist of two arrays, each side made of a matrix of single pads with an active area of 5×5 mm^2 and 100 μm, assembled in groups of 2×2. The final scheme of the detector, stylized in Fig. A.3, will consist of a multitude of pads, in columns and rows, for a total area of 60×30 mm^2, in order to cover enough horizontal surface, to be able to detect RIBs even with large horizontal dispersion. Each detector could be able to sustain very high intensity up to 10^7 pps over the whole array. Moreover, each detection system will consist of a sandwich configuration of two arrays, a few cm away from each other, and with a half pitch both horizontally and vertically, to improve the position resolution and dead region around each pad, allowing to reach efficiencies up to 90%. Tests are currently ongoing on the new SiC 5×5 mm^2 prototype pads, which have shown a detector capacitance of 21 pF at

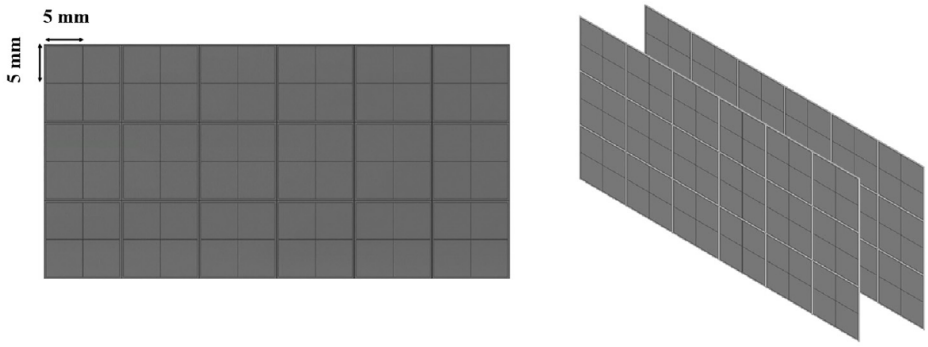

FIGURE A.3: Scheme of the SiC diagnostics and tagging detectors for the new FRAISE facility. On the left a frontal view, covering 60 × 30 mm^2, while on the right a side view of the two multipad-array separated and shifted by a few cm. Figure taken from [43]

400 V depletion voltage.

The future possibilities of the new FRAISE facility have been also tested by a series of simulations produced on the LISE++ software. Simulations used the standard configuration for FRAISE discussed previously, assuming 2 kW power for the primary beam, and included also a 100 μm thick SiC detector at the symmetry point of the fragment separator. Simulations included primary beams of $^{12}C^{6+}$, $^{18}O^{8+}$,$^{20}Ne^{10+}$, $^{40}Ar^{18+}$, and used a fragmentation target of ^{9}Be, which thickness has been optimized for the secondary beam to be produced, according to the experimentally available thicknesses. Table. A.1 reports some of the expected intensities and energies in MeV/u using the dedicated primary beams, expecting values up to 10^8 pps for RIBs near the stability valley and 10^3 for ones far from it. Tagging $\Delta E - ToF$ plots have been produced, for which the ΔE was simulated by the energy deposited onto the SiC detector at the exit of the spectrometer, while the ToF was given by the time difference between the start, provided by a radiofrequency signal, and the stop, given by the same SiC detector. Fig. A.4 on top shows an example of a $\Delta E - ToF$ tagging plot, while maximizing for the production of ^{13}B, accounting for a total of 65% of the whole cocktail beam, while on the bottom the spatial distribution plot for all the ions produced is shown.

Further studies will be needed however for the feasibility of extraction through stripping of other primary beams, which will further improve the production of many RIBs that could be produced. Such studies will be mainly concerning the trajectories of ions inside the CS and the possible output power

TABLE A.1: List of primary beams studied for extraction by stripping, with relative energy and emission power [43].

Ion	Energy (MeV/u)	Power (kW)
$^{12}C^{6+}$	60	2
$^{18}O^{8+}$	70	2
$^{20}Ne^{10+}$	70	2
$^{40}Ar^{18+}$	60	2

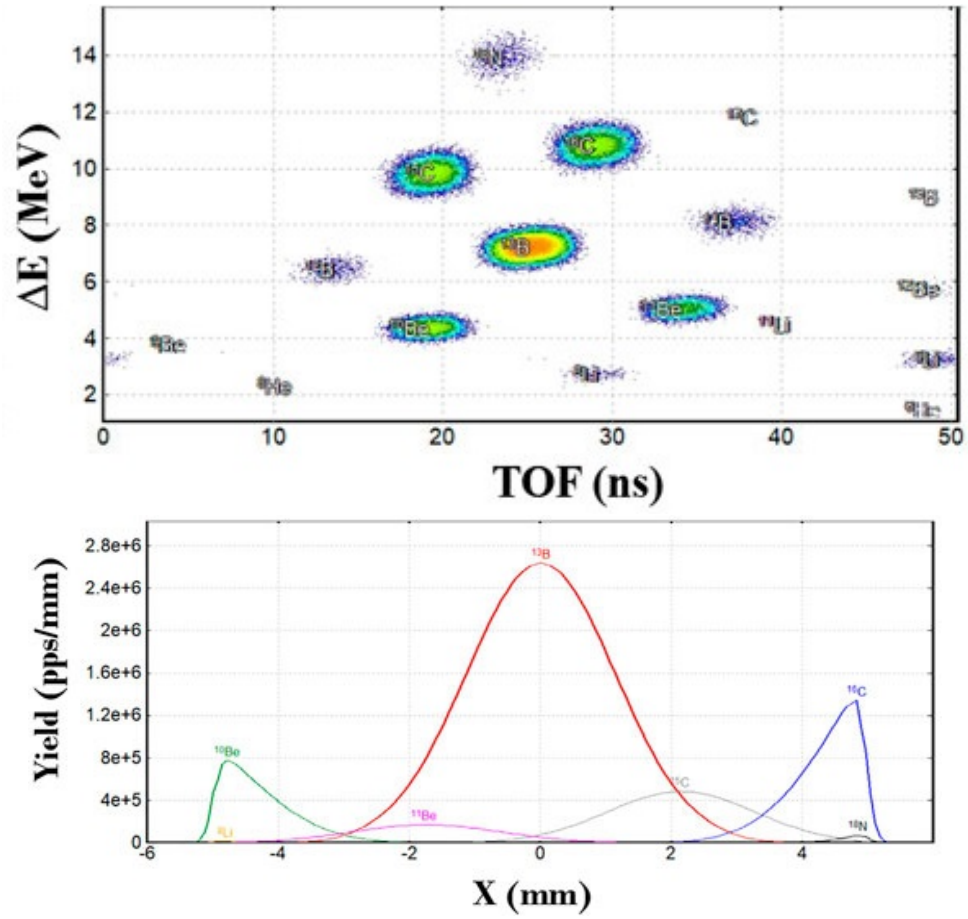

FIGURE A.4: LISE++ simulation of production of a ^{13}B radioactive beam through the new FRAISE fragment separator: on top a ΔE-ToF simulation obtained using the radiofrequency time reference; on the bottom the horizontal distribution of the simulated components of the cocktail beam, with ^{13}B the most produced ion, accounting for 66% of the total yield. Figure taken from [43].

achievable. Some examples are ^{13}C or ^{16}O, which could improve the yield production of neutron-rich isotopes of Li, Be and B, even more than the ones already studied, or ^{22}N and ^{36}Ar, which could improve the production of neutron-rich isotopes of N, O and F and the production of neutron-poor isotopes respectively. Other primary beams like ^{24}Mg, ^{27}Al, ^{32}S will be especially relevant for the production of RIBs with mass between 20 and 31, while ^{48}Ca, ^{54}Ni and ^{70}Zn will be studied for the production of isotopes with mass above 40. Among the aforementioned, the case of ^{70}Zn will be particularly interesting for the production of ^{68}Ni, already produced at LNS by the FRIBs facility for the study of its Pygmy Dipole Resonance phenomena [42]. It must be noted however that, for heavy primary beams as ^{70}Zn, the CS will have some issues of production which will have to be taken into account. Due to the new stripping extraction method, in the case of ions with mass greater than 40, the passage through the carbon film inside the CS will produce different charge states. This effect could result in some issues because while the selected charges are sent to the right extraction channel, the other charges produced (about 10% of the whole yield produced) are dissipated inside the CS, causing overheating in the internal structure. For this reason, it will be necessary to decrease the output power for the production of the primary beam, which in the case of ^{70}Zn was calculated to be 1 kW at most. Although the reduced output power however the production rate of ^{70}Zn will still be increased compared to that obtainable before the upgrade, resulting in a higher ^{68}Ni production, up to 8.5×10^5 pps and 70% beam purity.

A.0.1 Future possibilities with the new FRAISE fragment separator

The new facility of radioactive beams FRAISE at LNS will be competitive in the worldwide scenario of production of unstable nuclei at the Fermi energies. Thanks above all to the experience obtained through the past FRIBs facility, it will be possible to carry out plenty of new studies, both by expanding research topics already started at the LNS, and by developing new ones. Thanks to the new facility, it will first be possible to expand the research areas on cluster physics among neutron-rich isotopes of Be, B, C, and O. In fact, it could be possible to enrich the studies already performed in the past with FRIBs on ^{16}C or ^{10}Be isotopes, increasing the production yield and therefore the collected statistics, one of the main problems encountered in

past analysis. For all of these cases, it will be possible to produce radioactive beams with high yield, of the order of $10^6 - 10^7$ pps, with high purity above 90%. Moreover, with the aid of the new FARCOS cluster, consisting of 20 telescopes equipped with the GET electronics, it will be possible to study cluster states with a higher precision.

Another important case will be the ^{13}B cluster structure, for which a highly deformed configuration has been hypothesized, leading to the formation of rotational bands. As already addressed in Sect. 1.6.2, ^{13}B has already been studied theoretically through the AMD model, showing some interesting cluster states at excited levels with $^{12}\text{Be} + p$, $^{9}\text{Li} + \alpha$ and $^{10}\text{Be} + t$ configurations, presenting very high deformations. Some other exotic configurations, not predicted theoretically, are possible with very low probability, as the $^{7}\text{Li} + ^{6}\text{He}$ cluster state, already observed at LNS in previous experiments. At LNS in particular, an experiment with such radioactive beam was already planned and approved, the CLUB (Clusters in Boron), in 2021 with the FRIBs facility, but subsequently postponed. The new CLUB experiment will probably involve the use of FRAISE as a beam production facility, using the 4π CHIMERA multidetector alongside the powerful FARCOS array.

Another interesting topic that could be improved with FRAISE will be the study case of neutron skin or neutron halo structures. Thanks to FRAISE, many interesting isotopes, both light and medium mass, will be produced to study for example the case of the presence of the Pygmy Dipole Resonance, such as among ^{20}O, ^{34}Si, ^{38}S, ^{48}Ar or the previously mentioned ^{68}Ni. In particular, for the ^{68}Ni beam it could be possible to use the ^{70}Zn at 1 kW intensity as primary beam. In this case, in fact, it will be necessary to reduce the intensity of the primary beam due to possible problems that could arise in its production, due to the new *stripping* output channel. For what concerns this case study, with CHIMERA and FARCOS, it would be possible to measure the neutron shell occupancy dependence of the PDR below and above the particle emission threshold, also given the experience recently gained with other studies of the same type [42].

Moreover, the halo structure of light ions like ^{11}Be and ^{8}B could be investigated. For the study of the nuclear structure in nuclei far from the stability valley it is usually required both high efficiency detector array and high cross sections reactions. Moreover, the difficulty in the study is also accentuated by the fact that such inverse kinematic reactions introduce further problems both in the identification of the fragments and in the angular

resolution, worsening the quality of the study. Through the FRAISE facility, increasing the production yield up to 20 times, and using the new detectors of the upgraded LNS, it will be possible to obtain new and fruitful results. By studying the scattering on proton of ^{11}Be it would in fact be possible to study the neutron halo structure around ^{10}Be, showing resonance effects just above the particle emission threshold, at about 320 keV of excitation energy. On the other side, the proton-halo structure of ^{8}B could be investigated, performing both elastic and inelastic scattering on proton, which has shown in literature contradictory results on its existence.
Another topic of interest will be the study of isospin effects in heavy ion reactions, already explored with the CHIMERA multidetector in the past years. In this case, by producing neutron-poor and neutron-rich ions of the same charge, like ^{34}Ar and ^{46}Ar, it would be possible to improve the constraints of the symmetry energy of the Equation of State of nuclear matter, amplifying its effects.
Moreover, nuclear astrophysics topics could be expanded thanks to FRAISE with the production of radioactive isotopes interesting in this context, such as ^{13}N or ^{14}O, which could play an important role in the break-out of HCNO cycles to RP processes, to comprehend the presence and abundance of ^{13}C leading to the formation of heavier elements by neutron capture.
Lastly, FRAISE will give the possibility to produce radioactive beams interesting for medical purposes. Among the others, the case of ^{11}C is one of the most interesting, for which the β^+ decay would allow both to perform treatment and diagnosis exams at the same time, with respect to more traditional methods with H, He or C ions.

Bibliography

[1] Martin Freer. "The clustered nucleus—cluster structures in stable and unstable nuclei". In: *Reports on Progress in Physics* 70.12 (2007), p. 2149. DOI: 10.1088/0034-4885/70/12/R03. URL: https://dx.doi.org/10.1088/0034-4885/70/12/R03.

[2] M. Freer. "Clusters in nuclei". In: *Scholarpedia* 5 (6 2010).

[3] Hoyle F. "On Nuclear Reactions Occuring in Very Hot STARS.I. the Synthesis of Elements from Carbon to Nickel." In: *apjs* 1 (1954), p. 121. DOI: 10.1086/190005. URL: https://ui.adsabs.harvard.edu/abs/1954ApJS....1..121H.

[4] Kiyomi Ikeda, Noboru Takigawa, and Hisashi Horiuchi. "The Systematic Structure-Change into the Molecule-like Structures in the Self-Conjugate 4n Nuclei". In: *Progress of Theoretical Physics Supplement* E68 (1968), pp. 464–475. ISSN: 0375-9687. DOI: 10.1143/PTPS.E68.464. eprint: https://academic.oup.com/ptps/article-pdf/doi/10.1143/PTPS.E68.464/5216547/E68-464.pdf. URL: https://doi.org/10.1143/PTPS.E68.464.

[5] W. von Oertzen, Martin Freer, and Yoshiko Kanada-En'yo. "Nuclear clusters and nuclear molecules". In: *Physics Reports* 432.2 (2006), pp. 43–113. ISSN: 0370-1573. DOI: https://doi.org/10.1016/j.physrep.2006.07.001. URL: https://www.sciencedirect.com/science/article/pii/S0370157306002626.

[6] W. von Oertzen. "Two-center molecular states in ^{9}B,^{9}Be,^{10}Be, and ^{10}B ". In: *Zeitschrift für Physik A Hadrons and Nuclei* 354 (1996). ISSN: 0939-7922. DOI: 10.1007/s002180050010. URL: https://doi.org/10.1007/s002180050010.

[7] Yoshiko Kanada-En'yo and Hisashi Horiuchi. "Structure of Light Unstable Nuclei Studied with Antisymmetrized Molecular Dynamics". In: *Progress of Theoretical Physics Supplement* 142 (2001), pp. 205–263. ISSN: 0375-9687. DOI: 10.1143/PTPS.142.205. eprint: https://academic.

oup.com/ptps/article-pdf/doi/10.1143/PTPS.142.205/5440607/142-205.pdf. URL: https://doi.org/10.1143/PTPS.142.205.

[8] T. K. Eriksen et al. "Improved precision on the experimental $E0$ decay branching ratio of the Hoyle state". In: *Phys. Rev. C* 102 (2 2020), p. 024320. DOI: 10.1103/PhysRevC.102.024320. URL: https://link.aps.org/doi/10.1103/PhysRevC.102.024320.

[9] Lombardo I. and Dell'Aquila D. "Clusters in light nuclei: history and recent developments". In: *La Rivista del Nuovo Cimento* (2023). DOI: https://doi.org/10.1007/s40766-023-00047-4.

[10] Pascal Naidon and Shimpei Endo. "Efimov physics: a review". In: *Reports on Progress in Physics* 80.5 (2017), p. 056001. DOI: 10.1088/1361-6633/aa50e8. URL: https://dx.doi.org/10.1088/1361-6633/aa50e8.

[11] H Zheng and A Bonasera. "The Thomas theorem and the Efimov States within a generalized Bohr model". In: *Journal of Physics Communications* 4.8 (2020), p. 085011. DOI: 10.1088/2399-6528/abaca4. URL: https://dx.doi.org/10.1088/2399-6528/abaca4.

[12] G. Cardella et al. "Search for rare 3-α decays in the region of the Hoyle state of ^{12}C ". In: *Nuclear Physics A* 1020 (2022), p. 122395. ISSN: 0375-9474. DOI: https://doi.org/10.1016/j.nuclphysa.2022.122395. URL: https://www.sciencedirect.com/science/article/pii/S037594742200015X.

[13] Alessandro Chieffi and Marco Limongi. "The Explosive Yields Produced by the First Generation of Core Collapse Supernovae and the Chemical Composition of Extremely Metal Poor Stars". In: *The Astrophysical Journal* 577.1 (2002), p. 281. DOI: 10.1086/342170. URL: https://dx.doi.org/10.1086/342170.

[14] URL: https://web.infn.it/CHIMERA/index.php/it/.

[15] G. Cardella et al. "Investigating γ-ray decay of excited ^{12}C levels with a multifold coincidence analysis". In: *Phys. Rev. C* 104 (6 2021), p. 064315. DOI: 10.1103/PhysRevC.104.064315. URL: https://link.aps.org/doi/10.1103/PhysRevC.104.064315.

[16] A. Di Pietro et al. "Experimental investigation of exotic clustering in ^{13}B and ^{14}C using the resonance scattering method". In: *Journal of Physics: Conference Series* 966.1 (2018), p. 012040. DOI: 10.1088/1742-6596/966/1/012040. URL: https://dx.doi.org/10.1088/1742-6596/966/1/012040.

[17] W. von Oertzen. "Dimers based on the $\alpha + \alpha$ potential and chain states of carbon isotopes". In: *Zeitschrift für Physik A Hadrons and Nuclei* 357 (1997), 355–365. URL: https://doi.org/10.1007/s002180050255.

[18] M. Milin and W. von Oertzen. "Search for molecular bands in ^{13}C ". In: *The European Physical Journal A - Hadrons and Nuclei* 14 (2002), pp. 295–307. URL: https://doi.org/10.1140/epja/i2001-10199-6.

[19] G. Raciti et al. "Experimental Evidence of ^{2}He Decay from ^{18}Ne Excited States". In: *Phys. Rev. Lett.* 100 (19 2008), p. 192503. DOI: 10.1103/PhysRevLett.100.192503. URL: https://link.aps.org/doi/10.1103/PhysRevLett.100.192503.

[20] A. Pagano et al. "Characteristic time scale of cluster production at the Fermi energy". In: *Frontiers in Physics* 10 (2022). DOI: 10.3389/fphy.2022.1050450. URL: https://www.frontiersin.org/articles/10.3389/fphy.2022.1050450.

[21] D. Dell'Aquila et al. "New experimental investigation of the structure of ^{10}Be and ^{16}C by means of intermediate-energy sequential breakup". In: *Phys. Rev. C* 93 (2 2016), p. 024611. DOI: 10.1103/PhysRevC.93.024611. URL: https://link.aps.org/doi/10.1103/PhysRevC.93.024611.

[22] B. Gnoffo et al. "Clustering and molecular states in neutron rich nuclei". In: *Frontiers in Physics* 10 (2022). DOI: 10.3389/fphy.2022.1061633. URL: https://www.frontiersin.org/articles/10.3389/fphy.2022.1061633.

[23] M. Freer et al. "$\alpha : 2n : \alpha$ Molecular Band in ^{10}Be". In: *Phys. Rev. Lett.* 96 (4 2006), p. 042501. DOI: 10.1103/PhysRevLett.96.042501. URL: https://link.aps.org/doi/10.1103/PhysRevLett.96.042501.

[24] Q. Zhao et al. "α clustering and neutron-skin thickness of carbon isotopes". In: *The European Physical Journal A* 57.5 (2021), p. 157. ISSN: 1434-6001. DOI: 10.1140/epja/s10050-021-00465-0. URL: https://link.springer.com/10.1140/epja/s10050-021-00465-0.

[25] A.V. Dobrovolsky et al. "Nuclear matter distributions in the neutron-rich carbon isotopes $^{14-17}$C from intermediate-energy proton elastic scattering in inverse kinematics". In: *Nuclear Physics A* 1008 (2021), p. 122154. ISSN: 0375-9474. DOI: https://doi.org/10.1016/j.nuclphysa.2021.122154. URL: https://www.sciencedirect.com/science/article/pii/S0375947421000191.

[26] Fortune, H. T. "Structure of exotic light nuclei: Z = 2, 3, 4". In: *Eur. Phys. J. A* 54.3 (2018), p. 51. DOI: 10.1140/epja/i2018-12489-2. URL: https://doi.org/10.1140/epja/i2018-12489-2.

[27] T. Baba and M. Kimura. "Characteristic α and ^{6}He decays of linear-chain structures in ^{16}C". In: *Phys. Rev. C* 97 (5 2018), p. 054315. DOI: 10.1103/PhysRevC.97.054315. URL: https://link.aps.org/doi/10.1103/PhysRevC.97.054315.

[28] Y. Liu et al. "Positive-Parity Linear-Chain Molecular Band in ^{16}C". In: *Phys. Rev. Lett.* 124 (19 2020), p. 192501. DOI: 10.1103/PhysRevLett.124.192501. URL: https://link.aps.org/doi/10.1103/PhysRevLett.124.192501.

[29] J. X. Han et al. "Observation of the $\pi^2\sigma^2$-bond linear-chain molecular structure in ^{16}C". In: *Phys. Rev. C* 105 (4 2022), p. 044302. DOI: 10.1103/PhysRevC.105.044302. URL: https://link.aps.org/doi/10.1103/PhysRevC.105.044302.

[30] Yoshiko Kanada-En'yo et al. "Cluster States in ^{13}B". In: *Progress of Theoretical Physics* 120.5 (2008), pp. 917–935. ISSN: 0033-068X. DOI: 10.1143/PTP.120.917. eprint: https://academic.oup.com/ptp/article-pdf/120/5/917/5207226/120-5-917.pdf. URL: https://doi.org/10.1143/PTP.120.917.

[31] F. Risitano et al. "Status of the CLIR experiment at LNS". In: *IL NUOVO CIMENTO* 45 C (2022), p. 60. DOI: 10.1393/ncc/i2022-22060-5. URL: https://dx.doi.org/10.1393/ncc/i2022-22060-5.

[32] P. Russotto et al. "Status and Perspectives of the INFN-LNS In-Flight Fragment Separator". In: *Journal of Physics: Conference Series* 1014.1 (2018), p. 012016. DOI: 10.1088/1742-6596/1014/1/012016. URL: https://dx.doi.org/10.1088/1742-6596/1014/1/012016.

[33] A.D. Russo et al. "Preliminary design of the new FRAgment In-flight SEparator (FRAISE)". In: *Nuclear Instruments and Methods in Physics Research Section B: Beam Interactions with Materials and Atoms* 463 (2020), pp. 418–420. ISSN: 0168-583X. DOI: https://doi.org/10.1016/j.nimb.2019.04.037. URL: https://www.sciencedirect.com/science/article/pii/S0168583X19302216.

[34] I. Lombardo et al. "Use of Large Surface MicroChannel Plates for the Tagging of Intermediate Energy Exotic Beams". In: *Nuclear Physics B - Proceedings Supplements* 215.1 (2011), pp. 272 –274. ISSN: 0920-5632. DOI: https://doi.org/10.1016/j.nuclphysbps.2011.04.028. URL:

http://www.sciencedirect.com/science/article/pii/S0920563211002672.

[35] A. Pagano et al. "Fragmentation studies with the CHIMERA detector at LNS in Catania: recent progress". In: *Nuclear Physics A* 734 (2004), pp. 504 –511. ISSN: 0375-9474. DOI: https://doi.org/10.1016/j.nuclphysa.2004.01.093. URL: http://www.sciencedirect.com/science/article/pii/S0375947404001137.

[36] Pagano, E.V. et al. "Status and perspective of FARCOS: A new correlator array for nuclear reaction studies". In: *EPJ Web of Conferences* 117 (2016), p. 10008. DOI: 10.1051/epjconf/201611710008. URL: https://doi.org/10.1051/epjconf/201611710008.

[37] L. Acosta et al. "Campaign of measurements to probe the good performance of the new array FARCOS for spectroscopy and correlations." In: *Journal of Physics: Conference Series* 730.1 (2016), p. 012001. DOI: 10.1088/1742-6596/730/1/012001. URL: https://dx.doi.org/10.1088/1742-6596/730/1/012001.

[38] G. Cuttone et al. "EXCYT: The RIB project at INFN-LNS". In: *Nuclear Instruments and Methods in Physics Research Section B: Beam Interactions with Materials and Atoms* 261.1 (2007), pp. 1040–1043. ISSN: 0168-583X. DOI: https://doi.org/10.1016/j.nimb.2007.04.142. URL: https://www.sciencedirect.com/science/article/pii/S0168583X07009445.

[39] A Kjelberg and G Rudstam. "THE ISOLDE ISOTOPE SEPARATOR ON-LINE FACILITY AT CERN". In: (1970). URL: https://www.osti.gov/biblio/4176834.

[40] T. Nilsson et al. "REX-ISOLDE-post-accelerated radioactive beams at cern-ISOLDE". In: *AIP Conference Proceedings* 576.1 (2001), pp. 265–268. ISSN: 0094-243X. DOI: 10.1063/1.1395300. eprint: https://pubs.aip.org/aip/acp/article-pdf/576/1/265/11608685/265_1_online.pdf. URL: https://doi.org/10.1063/1.1395300.

[41] G. Raciti et al. "Intermediate energies tagged RIBs". In: *Nuclear Instruments and Methods in Physics Research, Section B: Beam Interactions with Materials and Atoms* 266.19-20 (2008), 4632 – 4636. DOI: 10.1016/j.nimb.2008.05.153. URL: https://www.sciencedirect.com/science/article/pii/S0168583X0800791X.

[42] N.S. Martorana et al. "First measurement of the isoscalar excitation above the neutron emission threshold of the Pygmy Dipole Resonance in 68Ni". In: *Physics Letters B* 782 (2018), pp. 112–116. ISSN: 0370-2693.

DOI: https://doi.org/10.1016/j.physletb.2018.05.019. URL: https://www.sciencedirect.com/science/article/pii/S0370269318303836.

[43] N. S. Martorana et al. "Radioactive ion beam opportunities at the new FRAISE facility of INFN-LNS". In: *Frontiers in Physics* 10 (2022). ISSN: 2296-424X. DOI: 10.3389/fphy.2022.1058419. URL: https://www.frontiersin.org/articles/10.3389/fphy.2022.1058419.

[44] E. Rapisarda. *FRIBs: tagged intermediate energy radioactive ion beams at Laboratori Nazionali del Sud*. PhD thesis, Università Di Catania, 2006.

[45] Thomas Baumann. *Minicourse on Experimental techniques at the NSCL Fragment Separators*. 2001.

[46] David J. Morrissey and Brad M. Sherrill. "In-Flight Separation of Projectile Fragments". In: *The Euroschool Lectures on Physics with Exotic Beams, Vol. I*. Ed. by Jim Al-Khalili and Ernst Roeckl. Berlin, Heidelberg: Springer Berlin Heidelberg, 2004, pp. 113–135. ISBN: 978-3-540-44490-9. DOI: 10.1007/978-3-540-44490-9_4. URL: https://doi.org/10.1007/978-3-540-44490-9_4.

[47] O.B. Tarasov and D. Bazin. "LISE++: Exotic beam production with fragment separators and their design". In: *Nuclear Instruments and Methods in Physics Research Section B: Beam Interactions with Materials and Atoms* 376 (2016), pp. 185–187. ISSN: 0168-583X. DOI: https://doi.org/10.1016/j.nimb.2016.03.021. URL: https://www.sciencedirect.com/science/article/pii/S0168583X1600224X.

[48] Russotto, P. et al. "Dynamical versus statistical production of Intermediate Mass Fragments at Fermi Energies". In: *Eur. Phys. J. A* 56.1 (2020), p. 12. DOI: 10.1140/epja/s10050-019-00011-z. URL: https://doi.org/10.1140/epja/s10050-019-00011-z.

[49] G. Politi et al. "Isospin effects on reaction dynamics at Fermi energies". In: *EPJ Web Conf.* 194 (2018), p. 07003. DOI: 10.1051/epjconf/201819407003. URL: https://doi.org/10.1051/epjconf/201819407003.

[50] Gnoffo Brunilde. "Isospin influence on the IMFs production in the ^{78,86}Kr + ^{40,48}Ca reactions at 10 AMeV". In: *Il Nuovo Cimento C* 39 (2016). DOI: 10.1393/ncc/i2016-16275-0.

[51] S. Pirrone et al. "Isospin influence on fragments production in ^{78}Kr +^{40}Ca and ^{86}Kr +^{48}Ca collisions at 10 MeV/nucleon". In: *The European Physical Journal A* 55 (2 2019). DOI: 10.1140/epja/i2019-12695-4. URL: https://doi.org/10.1140/epja/i2019-12695-4.

[52] N. Le Neindre et al. "Mass and charge identification of fragments detected with the Chimera Silicon–CsI(Tl) telescopes". In: *Nuclear Instruments and Methods in Physics Research Section A: Accelerators, Spectrometers, Detectors and Associated Equipment* 490.1 (2002), pp. 251–262. ISSN: 0168-9002. DOI: https://doi.org/10.1016/S0168-9002(02)01008-2. URL: https://www.sciencedirect.com/science/article/pii/S0168900202010082.

[53] P. Russotto et al. "Mass identification by means of Energy-Time-of-Flight technique using large area silicon detector in a 4π array: The CHIMERA case". In: *Nuclear Instruments and Methods in Physics Research Section A: Accelerators, Spectrometers, Detectors and Associated Equipment* 1056 (2023), p. 168593. ISSN: 0168-9002. DOI: https://doi.org/10.1016/j.nima.2023.168593. URL: https://www.sciencedirect.com/science/article/pii/S0168900223005831.

[54] G. Cardella et al. "Different methods for the identification of short-life nuclei: the ^{8}Be case". In: *The European Physical Journal Plus* 138 (1 2023). ISSN: 2190-5444. DOI: 10.1140/epjp/s13360-023-03681-3. URL: https://doi.org/10.1140/epjp/s13360-023-03681-3.

[55] Quattrocchi, L. et al. "The FARCOS project. First characterization of CsI(Tl) crystals of the FARCOS array using charged particle beams at LNS". In: *EPJ Web of Conferences* 66 (2014), p. 11001. DOI: 10.1051/epjconf/20146611001. URL: https://doi.org/10.1051/epjconf/20146611001.

[56] G. Verde et al. "The Farcos project: Femtoscope Array for Correlations and Femtoscopy". In: *Journal of Physics: Conference Series* 420.1 (2013), p. 012158. DOI: 10.1088/1742-6596/420/1/012158. URL: https://dx.doi.org/10.1088/1742-6596/420/1/012158.

[57] Acosta, L. et al. "FARCOS, a new array for femtoscopy and correlation spectroscopy". In: *EPJ Web of Conferences* 31 (2012), p. 00035. DOI: 10.1051/epjconf/20123100035. URL: https://doi.org/10.1051/epjconf/20123100035.

[58] A. Castoldi et al. "Laser mapping of the inter-strip response in double sided silicon strip detectors for particle identification". In: *Journal of Instrumentation* 10.01 (2015), p. C01017. DOI: 10.1088/1748-0221/10/01/C01017. URL: https://dx.doi.org/10.1088/1748-0221/10/01/C01017.

[59] E.C. Pollacco et al. "GET: A generic electronics system for TPCs and nuclear physics instrumentation". In: *Nuclear Instruments and Methods in Physics Research Section A: Accelerators, Spectrometers, Detectors and Associated Equipment* 887 (2018), pp. 81–93. ISSN: 0168-9002. DOI: https://doi.org/10.1016/j.nima.2018.01.020. URL: https://www.sciencedirect.com/science/article/pii/S0168900218300342.

[60] A. Castoldi, C. Guazzoni, and T. Parsani. "Versatile multi-channel CMOS frontend with selectable full-scale dynamics from 100 MeV up to 2.2 GeV for the readout of detector's signals in nuclear physics experiments". In: *Il Nuovo Cimento* 41 C (2018), p. 168. DOI: 10.1393/ncc/i2018-18168-6.

[61] A. Castoldi, C. Guazzoni, and T. Parsani. "A CMOS Frontend for Scintillators Readout by Photodiodes for Nuclear Physics Experiments". In: *IEEE Transactions on Nuclear Science* 64.10 (2017), pp. 2678–2682. DOI: 10.1109/TNS.2017.2741962.

[62] M. Freer et al. "Helium breakup states in ^{10}Be and ^{12}Be". In: *Phys. Rev. C* 63 (3 2001), p. 034301. DOI: 10.1103/PhysRevC.63.034301. URL: https://link.aps.org/doi/10.1103/PhysRevC.63.034301.

[63] O.B. Tarasov and D. Bazin. "LISE++: Radioactive beam production with in-flight separators". In: *Nucl. Instr. Meth. Phys. Res., Sect. B* 266.19 (2008), pp. 4657 –4664. ISSN: 0168-583X. DOI: https://doi.org/10.1016/j.nimb.2008.05.110. URL: http://www.sciencedirect.com/science/article/pii/S0168583X08007969.

[64] URL: https://kaliveda.in2p3.fr/index.html.

[65] D. Horn et al. "The Mass dependence of CsI(Tl) scintillation response to heavy ions". In: *Nucl. Instrum. Meth. A* 320 (1992), pp. 273–276. DOI: 10.1016/0168-9002(92)90785-3.

[66] M. Pârlog et al. "Response of CsI(Tl) scintillators over a large range in energy and atomic number of ions. Part I: recombination and δ-electrons". In: *Nuclear Instruments and Methods in Physics Research Section A: Accelerators, Spectrometers, Detectors and Associated Equipment* 482.3 (2002), pp. 674–692. ISSN: 0168-9002. DOI: https://doi.org/10.1016/S0168-9002(01)01710-7. URL: https://www.sciencedirect.com/science/article/pii/S0168900201017107.

[67] M. Pârlog et al. "Response of CsI(Tl) scintillators over a large range in energy and atomic number of ions. Part II: calibration and identification in the INDRA array". In: *Nuclear Instruments and Methods in*

Physics Research Section A: Accelerators, Spectrometers, Detectors and Associated Equipment 482.3 (2002), pp. 693–706. ISSN: 0168-9002. DOI: https://doi.org/10.1016/S0168-9002(01)01712-0. URL: https://www.sciencedirect.com/science/article/pii/S0168900201017120.

[68] J. Pouthas et al. "INDRA, a 4π charged product detection array at GANIL". In: *Nuclear Instruments and Methods in Physics Research Section A: Accelerators, Spectrometers, Detectors and Associated Equipment* 357.2 (1995), pp. 418–442. ISSN: 0168-9002. DOI: https://doi.org/10.1016/0168-9002(94)01543-0. URL: https://www.sciencedirect.com/science/article/pii/0168900294015430.

[69] R. J. Charity. "*N*-*Z* distributions of secondary fragments and the evaporation attractor line". In: *Phys. Rev. C* 58 (2 1998), pp. 1073–1077. DOI: 10.1103/PhysRevC.58.1073. URL: https://link.aps.org/doi/10.1103/PhysRevC.58.1073.

[70] K. Sümmerer and B. Blank. "Modified empirical parametrization of fragmentation cross sections". In: *Phys. Rev. C* 61 (3 2000), p. 034607. DOI: 10.1103/PhysRevC.61.034607. URL: https://link.aps.org/doi/10.1103/PhysRevC.61.034607.

[71] Glenn F. Knoll. *Radiation Detection and Measurement*. 4th. Wiley, 2010. ISBN: 9780470131480.

[72] S. Grévy and R. Hue. "CLIM : the new rotating target for exotic nuclei production at LISE spectrometer". In: *24th World Conference of the International Nuclear Target Development Society - INTDS2008*. Caen, France, 2008. URL: https://hal.in2p3.fr/in2p3-00326196.

[73] F. Cappuzzello et al. "The MAGNEX spectrometer: Results and perspectives". In: *European Physical Journal A* 52.6 (2016). DOI: 10.1140/epja/i2016-16167-1. URL: https://link.springer.com/article/10.1140/epja/i2016-16167-1.

[74] Martorana N.S. et al. "Latest results on the FraISe facility and possible physics cases at INFN-LNS". In: *Il Nuovo Cimento* (2023). In press.